

Theoretical and Experimental Investigations of  
the Elastic Properties of Carbon Nanotube-  
Reinforced Polymer Thin Films

Behnam Ashrafi

May, 2008

Department of Mechanical Engineering  
McGill University, Montreal, QC, Canada, H3A 2K6

A thesis submitted to  
McGill University  
in partial fulfillment of the requirements for the degree of  
Doctor of Philosophy

©Copyright  
2008, B. Ashrafi

## Abstract

Nanocomposites are a promising new class of materials for the mechanical components of microstructures such as microactuators and microresonators. This work presents a combination of theoretical and experimental investigations of the utility of carbon nanotube-reinforced composites for designing microstructures. In the theoretical part of this research, the effects of nanotube aspect ratio, dispersion, alignment, and volume fraction on the elastic modulus and longitudinal wave velocity are analyzed by recourse to the Mori-Tanaka theory. The calculated bounds on Young's modulus and wave velocity capture the trend of the experimental results reported in the literature. Polymer-matrix nanocomposites reinforced with aligned, dispersed single-walled carbon nanotubes are identified as excellent candidates for small structures with properties rivaling those of metallic- and ceramic-structures used in the current generation of microelectromechanical systems (MEMS). The experimental part of this research focuses on the manufacture and characterization of carbon nanotube-reinforced polymer thin films. A novel nanoindenter-based bending test is developed for characterizing the elastic properties of nanocomposite thin films. This technique is first numerically verified using finite element methods. Polymer thin films with known mechanical properties are then utilized to validate the technique experimentally. Next, epoxy-matrix and vinyl ester epoxy-matrix nanocomposite films (ranging from 50 to 70  $\mu\text{m}$  in thickness) reinforced with low concentrations ( $<1\%$  by weight) of single-walled carbon nanotubes are successfully manufactured and characterized. Finally, using carbon nanotube sheets (buckypaper), polymer-matrix nanocomposite films with high volume fractions of carbon nanotubes (30-40%) are manufactured by using two different techniques: vacuum infiltration and hot press. This relatively high content of carbon nanotubes results in a three- to four-fold increase in the elasticity of nanocomposites with respect to that of the pure polymer. A qualitative comparison between the state-of-the-art nanocomposite manufacturing technology and the predicted upper bound theoretical results highlights the enormous improvements needed in materials processing and micromachining to harness the

full potential of carbon nanotube-reinforced composites for microstructure applications.

## Résumé

Les nano-composites sont une nouvelle classe de matériaux prometteurs pour les composants mécaniques de microstructures telles que les micro-actuateurs et micro-résonateurs. Ce travail présente une combinaison d'études théoriques et expérimentales sur l'utilité de composites renforcés par des nanotubes de carbone pour la conception de microstructures. Dans la partie théorique de cette recherche, les effets du rapport de forme, de la dispersion, de l'alignement et de la fraction volumique des nanotubes sur le module élastique et la vitesse d'onde longitudinale ont été analysés en utilisant la théorie de Mori-Tanaka. Les limites calculées du module d'Young et de la vitesse d'onde capturent la tendance des résultats expérimentaux rapportés dans la littérature. Les nano-composites à matrice polymère renforcée avec des SWNT alignés et dispersés ont été identifiés comme d'excellents candidats pour de petites structures dont les propriétés rivalisent avec les structures métalliques ou céramiques utilisées dans la présente génération de systèmes micro-électro-mécaniques (MEMS). La partie expérimentale de cette recherche focalise sur la fabrication et la caractérisation de films polymères minces renforcés avec des nanotubes de carbone. Du aux difficultés rencontrées avec les techniques traditionnelles pour la caractérisation du module élastique de films polymère minces, une nouvelle technique, un test en flexion par nano-indentation, a été développée avec succès. La technique a été d'abord vérifiée numériquement par la méthode d'éléments finis. Puis des films polymère minces avec des propriétés connues ont été utilisés pour vérifier cette technique expérimentalement. Par la suite, des films minces (épaisseur variant de 50 à 70  $\mu\text{m}$ ) de nano-composite à matrice époxy et vinyle-ester renforcées avec de faibles concentrations de SWNT (1% par masse) ont été fabriqués et caractérisés avec succès. Finalement, des films de nano-composite à matrice polymère avec une haute fraction volumique de nanotubes de carbone (30-40%) ont été fabriqués par deux techniques en utilisant des feuilles de nanotube (buckypaper) : infiltration par pression et presse chauffante. Ces films à haut taux de nanotubes de carbone présentent des propriétés élastiques 3 à 4 fois

supérieures à celle du polymère pur. Une comparaison qualitative entre l'état de l'art sur les technologies de la fabrication des nano-composites et les limites supérieures des résultats théoriques souligne le besoin d'importantes améliorations au niveau de la transformation des matériaux et du micro-usinage afin d'exploiter tout le potentiel des composites renforcés par des nanotubes de carbone pour les applications microstructurales.

## **Acknowledgements**

The author wishes to express his sincere gratitude to his Ph.D. supervisors, Professors Pascal Hubert and Srikar Vengallatore for their extensive guidance, encouragement and support during this research. They provided me with the opportunity to do this research and they were always willing to provide knowledge, expertise, and assistance. Their professional and personal attitudes have made my stay at McGill University a very rewarding and memorable experience.

I am grateful to Mr. Vahid Mirjalili and Mr. Cyrill Cattin for their assistance and discussion, and also for their amiable friendship. Among other things, Cyrill helped me with film preparations and Vahid with SEM imaging as well as with buckypaper impregnation.

I am grateful to Dr. Benoit Simard, Dr. Yakienda Martinez-rubi and Dr. Jingwen Guan at the Steacie Institute for Molecular Studies of the National Research Council of Canada (NRC-SIMS) in Ottawa for providing the materials for this research as well as writing the section on carbon nanotube-sheet manufacturing. Sincere thanks and appreciation go to Mr. Rene Pronovost for his contribution to the finite element modelling part of this research. Special thanks go to Mr. Jonathan Laliberté for his guidance and advice during the practical work in composite laboratories.

Many thanks to Ms Loleï Khoun for her help for the abstract translation. Special thanks to Dr. Brian Roy, a great friend, for proof-reading this dissertation.

I am very grateful to all the members of the Composite Materials and Structures Group and Micro/Nano System Group who provided scientific support throughout my studies.

Finally, financial support from the Natural Sciences and Engineering Research Council (NSERC) of Canada through the Discovery Grants Program and a PGSD scholarship are gratefully acknowledged.

## Table of Content

Abstract.....	ii
Résumé.....	iv
Acknowledgements.....	vi
Table of Content .....	viii
List of Figures.....	xii
List of Tables .....	xvii
List of Symbols.....	xviii
Chapter 1.....	1
Introduction and Objectives.....	1
1.1    Introduction.....	1
1.2    Applications for CNT Composites.....	2
1.2.1    Applications as Secondary Reinforcement.....	2
1.2.1.1    Interlaminar Shear.....	3
1.2.1.2    Hybrid Fibres .....	4
1.2.2    Sensing Applications .....	5
1.2.2.1    Strain Sensing.....	5
1.2.2.2    Heath Monitoring.....	5
1.2.3    Application for Small-Volume Structures .....	7
1.3    Objectives and Approach.....	8
Chapter 2.....	11
Theoretical Investigation of Mechanical Properties of Carbon Nanotube-Reinforced Microactuators.....	11
2.1    Introduction.....	11
2.2    Modelling of an Electrostatic Microactuator .....	12
2.2.1    Mechanical Force.....	12
2.2.2    Electrostatic Force .....	12
2.3    Requirements of an Electrostatic Microactuator.....	13
2.3.1    High Speed of Actuation.....	13
2.3.2    Low Actuation Voltage.....	14

2.4	Materials for Electrostatic Microactuators.....	14
2.5	Structure of Nanocomposite Actuators.....	17
2.6	Theoretical Mechanics of Nanocomposite Actuators.....	20
2.6.1	Theory of Mori-Tanaka.....	21
2.6.1.1	Eshelby Approach.....	23
2.6.1.2	Mori-Tanaka Approach.....	27
2.6.2	Young's Modulus of Composite Microactuator.....	28
2.6.3	Longitudinal Wave Velocity of Composite Microactuator.....	29
2.7	Numerical Results.....	31
2.7.1	Comparison with Previously Reported Experiments.....	35
2.8	Summary.....	39
Chapter 3.....		43
Elastic Characterization of Soft Thin Films through Nanoindenter-Based Bending Tests.....		43
3.1	Introduction.....	43
3.2	Theory.....	45
3.2.1	Bending Deformation of a Clamped Circular Plate.....	47
3.2.2	Contact Indentation due to a Spherical Tip.....	48
3.2.3	Bending-Indentation of a Plate under a Spherical Tip.....	48
3.3	Finite Element Modelling.....	49
3.4	Experimental Protocols.....	55
3.4.1	Nanoindenter-Based Bending Tests in the Plate Regime.....	55
3.4.2	Design of Test Jigs.....	59
3.4.3	Specimen Preparation.....	61
3.4.4	Protocol for Nanoindenter-Based Tests.....	64
3.5	Results.....	67
3.6	Summary and Discussion.....	71
Chapter 4.....		75
Elastic Characterization of Dilute SWNT-Reinforced Polymer Thin Films.....		75
4.1	Introduction.....	75
4.2	Synthesis of Polymer Nanocomposite Thin Films.....	75

4.2.1	SWNT-Reinforced Epoxy Thin Films .....	76
4.2.2	SWNT-Reinforced Epoxy Vinyl Ester Thin Films.....	77
4.3	Experimental Procedure for Elastic Characterization.....	77
4.3.1	Nanoindenter-Based Bending Tests.....	77
4.3.2	Tensile Dynamic Mechanical Analysis Tests.....	77
4.4	Elastic Characterization of SWNT-Reinforced Polymer Thin Films ...	79
4.4.1	SWNT-Reinforced Epoxy Thin Films .....	79
4.4.2	SWNT-Reinforced Epoxy Vinyl Ester Thin Films.....	80
4.5	Conclusions.....	83
Chapter 5	.....	85
Elastic Characterization of Polymer-Impregnated Buckypaper Thin Films.....		85
5.1	Introduction.....	85
5.2	Buckypaper Manufacturing .....	89
5.2.1	Purification of Raw SWNT Manufactured with Double Laser Ablation System.....	89
5.2.2	Preparation of Suspension of SWNTs .....	89
5.2.3	Preparation of Buckypaper .....	89
5.2.4	Post-Treatment of Buckypaper .....	89
5.3	Characterization of Pristine Buckypaper .....	90
5.3.1	Characterization Using Scanning Electron Microscope .....	90
5.3.2	Characterization of Impurities .....	91
5.3.3	Density Characterization.....	92
5.3.4	Elastic Characterization of Pristine Buckypaper .....	93
5.4	Bending Deformation of Isotropic Bi-Layer Films .....	94
5.5	Impregnation Techniques.....	95
5.5.1	Vacuum Infiltration Technique.....	96
5.5.2	Hot-Press Technique.....	99
5.6	Results of Resin-Impregnated Buckypaper Sheets.....	99
5.6.1	Characterization through Scanning Electron Microscope .....	99
5.6.2	Characterization of Elastic Properties.....	102
5.7	Summary .....	105

Chapter 6.....	107
Summary and Future Work.....	107
Appendix 1: Blueprint of the Fixture for Bending Test of Soft Thin Films.....	112
Appendix 2: Processing of CNT/Polymer Composite Films.....	113
A 2.1: Solution Processing Technique.....	113
A 2.2: Melt Processing Technique.....	114
A 2.3: In Situ Polymerization Technique .....	114
A 2.4: Carbon Nanotube Sheet .....	115
Appendix 3: Raw Data.....	116
References.....	120

## List of Figures

Figure 1.1: a) Deposition of carbon nanotubes on a carbon fibre mat using electrophoresis b) Scanning electron microscope (SEM) image of the deposited CNT on carbon fibres [3].....	3
Figure 1.2: SEM image of a carbon fibre a) before and b) after CNT growth [6]..	4
Figure 1.3: a) Buckypaper sheet as a strain sensor attached to a brass tensile specimen. b) Variations in voltage due to changes in the specimen strain [10].....	5
Figure 1.4: Application of CNT for composite health monitoring a) a schematic of CNT penetration between fibres b) detection of delamination due the change in CNT/polymer resistance [13].....	6
Figure 1.5: a) A composite thermomechanical microactuator made of CNTs and Ni b) an increase in mechanical properties due to increase in the concentration of CNT inside the solution [14]. ....	7
Figure 1.6: CNT-reinforced polymer micro-gripper. Red arrow shows the direction for CNT alignment [16]. ....	8
Figure 2.1: Schematic illustration of an electrostatically actuated microbeam. ..	11
Figure 2.2: One-dimensional model of electrostatic micro-actuators.....	13
Figure 2.3: Materials selection chart for microactuators. ....	16
Figure 2.4: Schematic illustration of a nanocomposite actuator beam with perfectly-aligned nanotubes embedded in an isotropic matrix .....	18
Figure 2.5: Definition of the equivalent homogeneous inclusion. First the homogeneous inclusion is subjected to a stress-free shape change. An appropriate surface traction is applied to the inclusion to put it back inside the matrix. After equilibrium, the constrained strain inside the inclusion can be obtained by the Eshelby tensor [47].....	24
Figure 2.6: Effect of SWNT aspect ratio and alignment on Young's modulus....	31
Figure 2.7: Effect of volume fraction and alignment of SWNT, MWNT, and SWNT arrays on Young's modulus of PMMA-matrix nanocomposites. The Young's modulus of monolithic silicon is also shown for comparison.....	33

Figure 2.8: Effect of volume fraction and alignment of SWNT, MWNT, and SWNT arrays on the longitudinal wave velocity of PMMA-matrix nanocomposite. The wave velocity of monolithic silicon is also shown for comparison.....	34
Figure 2.9: Effect of SWNT volume fraction on longitudinal wave velocity for representative metal-, ceramic- and polymer-matrix nanocomposites. ....	35
Figure 2.10: Comparison of measured longitudinal wave velocities of Ni-MWNT nanocomposite microresonators with calculated values for perfectly-aligned and perfectly-random composites. ....	36
Figure 2.11: Comparison of measured Young's modulus of PVA-MWNT nanocomposites with the calculated values for perfectly-aligned and perfectly-random composites.....	38
Figure 2.12: Materials selection chart for nanocomposite microactuators. The curve represents the calculated upper bound for PMMA-matrix reinforced with aligned SWNT. ....	39
Figure 3.1: a) Contact indentation ( $\delta_C$ ) and plate deflection ( $\delta_P$ ) as a result of load $P$ . b) A series of springs representing Figure 2-a. $S_C$ and $S_P$ are, respectively, the contact stiffness and the plate stiffness of the film. c) Experimental valuation of contact indentation ( $\delta_C$ ) through a thin film attached to a substrate. ....	46
Figure 3.2: Mesh, geometry and boundary conditions of the FE model of Hertzian contact mechanics. Indenter is modeled as an arc to reduce numbers of elements. ....	52
Figure 3.3: Comparison between FEA and Hertzian contact theory for contact stiffness. The Young's modulus of the film for each case is indicated on the figure. ....	53
Figure 3.4: a) Mesh, geometry and boundary conditions of the FE model of a clamped circular plate under a point load. ....	53
Figure 3.5: Comparison between the plate theory, the Hertzian theory and the FE model for $h=100 \mu\text{m}$ and $E=1 \text{ GPa}$ . Associated errors between theories and the FE model are represented. Vertical dashed line shows $P_{\text{max}}$ . ....	55

Figure 3.6: a) A schematic design of the fixture and its components. b) Top view of the fixture.....	56
Figure 3.7: Effect of the maximum load on the behaviour of 1, 10, and 100 $\mu\text{m}$ films for a typical range of polymers. The vertical dashed line shows the minimum limit of typical Hysitron indenters.....	57
Figure 3.8: The maximum possible force that can be applied in the plate deformation regime as a function of film thickness. The Young's modulus corresponding to each curve, and the force range of the Hysitron TriboIndenter, are indicated.....	58
Figure 3.9: Contact-to-plate displacement ratio as a function of film thickness for representative polymers. The solid curve shows the ratio for all polymers when the maximum force ( $P_{\text{max}}$ ) is applied. Thin curves show the ratio for $P=15\text{ mN}$ (the maximum force of a typical Hysitron indenter).....	59
Figure 3.10: Schematic view and dimensions of the jig and the nanoindenter transducer.....	60
Figure 3.11: Manufacture of thin films using a steel shim and two glass substrates. ....	63
Figure 3.12: Cure cycle for MY0510 epoxy system (ramp rates: $3^{\circ}\text{C}/\text{min}$ ).....	63
Figure 3.13: a) Using optical microscope to define the sample (points A, B, C, and D). b) A snapshot of the Triboindenter software when the optic was focused at point B.....	65
Figure 3.14: Load versus displacement for an epoxy film characterized with a load and load rate of 1 mN and 300 $\mu\text{N}/\text{sec}$ . Pink curve shows the combined plate-indentation behaviour, blue curve shows the nanoindentation behaviour and the black curve is the subtraction of the former curve from the latter one, representing pure plate behaviour.....	68
Figure 3.15: Young's modulus as a function of the thickness of epoxy films measured through two techniques, the "Hertzian corrected plate tests" and the "Combined plate-indentation tests". Contact-to-plate displacement ratios are shown for each thickness. ....	70

Figure 3.16: Load-displacement curve of the epoxy film attached to a steel substrate (load rate of 300 $\mu\text{N}/\text{sec}$ ). Hertz equation was fitted to the curve to extract the epoxy's Young's modulus.....	71
Figure 3.17: Young's modulus of LDPE as a function of load rates. The results are compared with those obtained through nanoindentation. ....	72
Figure 4.1: Edges of DMA films a) Epoxy vinyl ester nanocomposite films. b) Epoxy nanocomposite film (Plasma 1) with non-uniform edge. c) Micro-cracks of a few hundreds micrometers on epoxy nanocomposite films. ....	78
Figure 4.2: Micrographs of the plasma 1 specimen. The dark regions are identified as CNT-rich agglomerates a) resin-rich region with small SNWT agglomeration; b) Agglomerated SWNT region with a size of $\sim 300 \mu\text{m}$ ....	80
Figure 4.3: Storage modulus of epoxy vinyl ester nanocomposite films obtained through tensile DMA tests. ....	82
Figure 4.4: a) Young's modulus of SWNT-vinyl ester thin films as a function of SWNT volume fraction predicted through two techniques: DMA and nanoindenter based bending tests. b) Experimental results were compared with theoretical results obtained through Mori-Tanaka approach. ....	82
Figure 4.5: Micrographs of epoxy vinyl ester specimens. a) Pure polymer film ( $\times 100$ ). Lines of scratches can be seen the entire surface transferred from the glass substrates. b) Nanocomposite films with 0.6 wt % SWNT: small agglomerates of a few micrometers are seen. c) Higher magnification ( $\times 500$ ) of nanocomposite films with 0.6 wt % SWNT. The average size of agglomeration is between 5 to 10 $\mu\text{m}$ spread the entire sample. d) Resin-rich region with a size of a few tens of micrometers. ....	83
Figure 5.1: SEM images of pure buckypaper with 10K, 25K, 100K and 200 K magnifications.....	90
Figure 5.2: Weight change of two buckypaper sheets under nitrogen purge gas as a function of temperature. ....	91
Figure 5.3: Definition of geometric constants for an isotropic bi-layer plate.....	95
Figure 5.4: Schematic illustration of the vacuum infiltration technique used for impregnation of the buckypaper. ....	97

Figure 5.5: Viscosity of MY0510 epoxy system as a function of time for 4 different temperatures (adapted from [131]).....	98
Figure 5.6: Modified cure cycle used during impregnation of buckypaper. For comparison, original cure cycle of MY0510 epoxy is also shown. ....	98
Figure 5.7: Schematic illustration of the hot-press technique for impregnation of buckypaper.....	99
Figure 5.8: Cross-sectional view of vacuum-infiltrated samples. a) A comparison between pristine buckypaper and impregnated buckypaper. b) A broken surface with magnifications of 50K and 200K showing the bridging effect of CNT c) An 8 $\mu\text{m}$ -thick layer of resin film at one edge of the sample. ....	101
Figure 5.9: Cross-sectional view of hot-press samples. a) Two distinct regions can be differentiated: a resin-rich region and a non-impregnated region. b) Good resin wetting can be observed at the boundary of these two regions. c) There is no sign of resin infiltration in the middle of the CNT-rich region.....	102
Figure 5.10: Load-deflection curves for buckypaper, resin, and resin-infiltrated buckypaper composite manufactured by vacuum infiltration.....	104
Figure 5.11: A comparison between different films (pure epoxy, pristine buckypaper and impregnated buckypaper) and theoretical prediction using Mori-Tanaka technique.....	105

## List of Tables

Table 2.1: Nominal properties of bulk materials [22, 25].....	18
Table 2.2: Properties of nanotubes and nanotube-arrays [34-36] .....	20
Table 2.3: Components of Eshelby tensor, $S$ , for ellipsoidal and circular cylinder inclusions [47].....	26
Table 3.1: Advantages and disadvantages of traditional techniques for the elastic characterization of soft thin films .....	44
Table 3.2: Difference between Hertzian theory, plate theory and FE results .....	54
Table 3.3: Typical properties of Araldite MY0510 epoxy systems.....	61
Table 3.4: Young's modulus of epoxy films obtained through different methods for three different load rates.....	68
Table 4.1: Specifications of SWNT-reinforced epoxy films .....	76
Table 4.2: Elastic properties of epoxy polymer and its composites .....	79
Table 5.1: Elastic properties of pristine buckypaper and resin-impregnated buckypaper.....	87
Table 5.2: Elastic properties of resin-impregnated buckypaper sheets.....	88
Table 5.3: Density, volume fraction and Young's modulus of buckypaper .....	93
Table 5.4: Properties of buckypaper .....	94
Table 5.5: Young's modulus of polymer-impregnated buckypaper (GPa).....	103

## List of Symbols

$A$	Concentration factor; Buckypaper area
$A^N$	Dilute mechanical strain concentration tensor
$A^{dil}$	Concentration tensor of dilute composites
$A^{non-dil}$	Concentration tensor of non-dilute composites
$a$	Plate radius
$C^C$	Composite stiffness tensor
$C^M$	Matrix stiffness tensor
$C^N$	Nanofibre stiffness tensor
$c^{AC}$	Longitudinal wave velocity of aligned composite
$c^M$	Matrix longitudinal wave velocity
$c^{RC}$	Longitudinal wave velocity of random composite
$D$	Reinforcement diameter; Bending stiffness
$D_{ij}$	Bending stiffness tensor
$E$	Young's modulus
$E_I$	Indenter Young's modulus
$E_{L1}, E_{L2}$	Young's moduli of layers
$E_r$	Reduced modulus or combined modulus
$E_{11}$	Longitudinal Young's modulus
$E_{11}^N$	Nanofibre longitudinal Young's modulus
$E_{22}^N$	Nanofibre transverse Young's modulus
$E_{xx}^{AC}$	Longitudinal Young's modulus of aligned composite
$E_{yy}^{AC}$	Transverse Young's modulus of aligned composite
$E_{xx}^{RC}$	Young's modulus of random composite
$E_{11}^C$	Composite longitudinal Young's modulus
$E_{22}^C$	Composite transverse Young's modulus
$E^M$	Matrix Young's modulus
$E_{11}^R$	Reinforcement longitudinal Young's modulus
$F_e$	Microactuator electrostatic force

$F_m$	Microactuator mechanical force
$G_{12}$	Longitudinal shearing modulus
$G_{23}$	In-plane shearing modulus
$G_{12}^N$	Nanofibre longitudinal shear modulus
$G_{23}^N$	Nanofibre in-plane shear modulus
$G_{xy}^{AC}$	Longitudinal shear modulus of aligned composite
$G_{yz}^{AC}$	In-plane shear modulus of aligned composite
$g$	Distance between capacitor plates
$g_0$	Equilibrium distance between capacitor plates
$h$	Film thickness
$h_{L1}, h_{L2}$	Film thicknesses of layers
$I$	Identity tensor; Second moment of inertia
$I_1, I_3$	Esheby Constants
$K_t$	Film permeability
$k$	Spring stiffness constant
$L$	Reinforcement length; Beam length
$M_w$	Carbon atomic weight
$N$	Number of carbon atom per unit lengths
$N_a$	Avogadro's number
$n$	Number of carbon atoms per unit length of nanofibre
$Q$	Esheby Constant
$P$	Force
$P_{max}$	Maximum plate-regime force
$R$	Esheby Constant; Nanofibre radius
$R_{SW}$	Radius of single-walled carbon nanotube
$S$	Eshelby tensor
$s$	Nanofibre aspect ratio
$T$	Esheby Constant
$t$	Infiltration time
$V$	Voltage

$V_a$	SWNT rope packing fraction
$V_f$	Reinforcement volume fraction
$W_i$	Impurity weight
$W_t$	Buckypaper weight
$w$	Beam width
$\alpha$	Normalized difference of elastic constants
$\Delta P$	Vacuum pressure
$\delta_C$	Contact indentation
$\delta_P$	Plate deformation
$\delta_T$	Total displacement of plate
$\delta_{ij}$	Kronecker delta
$\bar{\varepsilon}$	Composite average strain
$\varepsilon^A$	Uniform external strain
$\varepsilon^C$	Constrained strain
$\varepsilon^I$	Inclusion average strain
$\varepsilon^T$	Transformation strain
$\varepsilon_0$	Vacuum permittivity
$\varepsilon_r$	Relative static permittivity
$\eta$	Resin viscosity
$\lambda$	Plate dimensionless constant
$\lambda', \lambda'', \lambda'''$	Boundary condition constants
$\rho$	Density
$\rho^{BP}$	Buckypaper density
$\rho^C$	Composite density
$\rho^M$	Matrix density
$\rho^N$	Nanofibre density
$\rho^{rope}$	Carbon nanotube rope density
$\bar{\sigma}$	Composite average stress
$\sigma^A$	external stress
$\sigma^I$	Inclusion stress

$\nu$	Poisson's ratio
$\nu_{12}$	Major Poisson's ratio
$\nu_I$	Poisson's ratio of indenter
$\nu_{L1}, \nu_{L2}$	Poisson's ratios of layers
$\nu_{xy}^{AC}$	Major Poisson's ratio of aligned composite
$\nu^{RC}$	Poisson's ratio of random composite
$\nu^M$	Matrix Poisson's ratio
$\nu_{12}^N$	Nanofibre major Poisson's ratio
$\nu_{23}$	In-plane Poisson's ratio

# Chapter 1

## Introduction and Objectives

### **1.1 Introduction**

Carbon nanotubes (CNT) are structures with diameters ranging from 1 to 100 nm and lengths of up to millimeters. These structures innately possess great potential as reinforcement for multifunctional, advanced composites. Carbon nanotubes have been reported to exhibit an elastic modulus that is five times that of steel, tensile strength that is sixty times that of high-carbon steel, thermal conductivity that is twenty times that of copper, electrical conductivity that is thousand times that of silver, and a mass density that is only one-sixth that of traditional steels [1].

During the past ten years, there has been a significant amount of research on the modelling, processing and characterization of CNT nanocomposites. Recent studies exhibit encouraging trends, which has led to continued interest in the development and application of CNT composites. However, a significant gap still exists between results obtained from experiments and expectations based on theoretical predictions [2]. In addition, the scaling and manufacture of CNT nanocomposites are difficult because of the following factors.

- 1) The small size of CNTs leads to strong forces (such as van der Waals forces) at the molecular scale. As a result, it is difficult to disperse carbon nanotubes within metallic, ceramic, or polymeric matrices.
- 2) Due to the very high aspect ratios of CNT<sup>1</sup>, the addition of a small amount of CNTs to the matrix significantly increases viscosity. This fact considerably reduces manufacturability.

---

<sup>1</sup> Aspect ratio is defined as the length over the diameter of a carbon nanotube

- 3) For advanced composites, a strict control of the alignment of the reinforcing agents within the matrix is crucial. Considering the size of carbon nanotubes, however, their manipulation is extremely difficult.
- 4) CNTs are very inert because of their atomic structure. As a result, interactions between carbon nanotubes and polymer molecules, which is an important factor in producing an effective composite, are not sufficiently strong.
- 5) Current manufacturing techniques of CNTs can produce only small quantities. Moreover, various purification techniques are necessary to remove impurities, resulting in longer manufacturing cycles. Mass production of carbon nanotubes is necessary for applications in bulk structures used in aerospace, sports, and automotive industries.

## **1.2 Applications for CNT Composites**

Due to the factors mentioned in Section 1.1, CNT composites are only now emerging as replacements for traditional composites. However, there are three potential applications in the near-future for carbon nanotube composites [2]:

- 1) Applications as secondary reinforcements of traditional composites to improve their functionality.
- 2) Sensing applications, such as monitoring crack growth in composites.
- 3) Reinforcement of miniaturized small-volume structures (hereafter referred to as microstructures), which are used in microelectromechanical systems (MEMS).

These applications are reviewed below in more detail.

### **1.2.1 Applications as Secondary Reinforcement**

Carbon nanotubes have high potential for applications as secondary reinforcements to improve the functionality of traditional composites by improving their inter-laminar shear strength, and by enhancing interaction between traditional fibres and polymers.

### 1.2.1.1 Interlaminar Shear

Traditional woven composites exhibit very good properties along the directions of reinforcing fibres (in-plane directions). However, the out-of-plane properties are still weak as they are dominated by the properties of the matrix. A few researchers have tried to incorporate CNTs in an effort to improve out-of-plane properties. Bekyarova *et al.* [3] introduced a technique called electrophoresis to deposit carbon nanotubes on carbon fibre (CF) fabric. In this technique, the application of a DC voltage on the carbon fibre mat results in the deposition of suspended CNT over the surfaces of carbon fibres (Figure 1.1). Then, traditional vacuum-assisted resin transfer molding (VARTM) is used to infiltrate the carbon fibre mat with an epoxy resin. This results in an overall increase of 30% in the interlaminar shear strength (ILSS) of the CF/CNT/epoxy composite as compared to that of CF/epoxy composite, without any degradation of the tensile properties. In another work by Gojny *et al.* [4, 5], CNTs are first added to the resin system using shear mixing techniques. The CNT-modified resin was then injected into the mold filled by glass fibre preform using resin transfer molding (RTM). Using these techniques the interlaminar shear strength of glass fibre/polymer composites was improved by up to 16% through the addition of a small quantity (0.3 wt %) of carbon nanotubes.

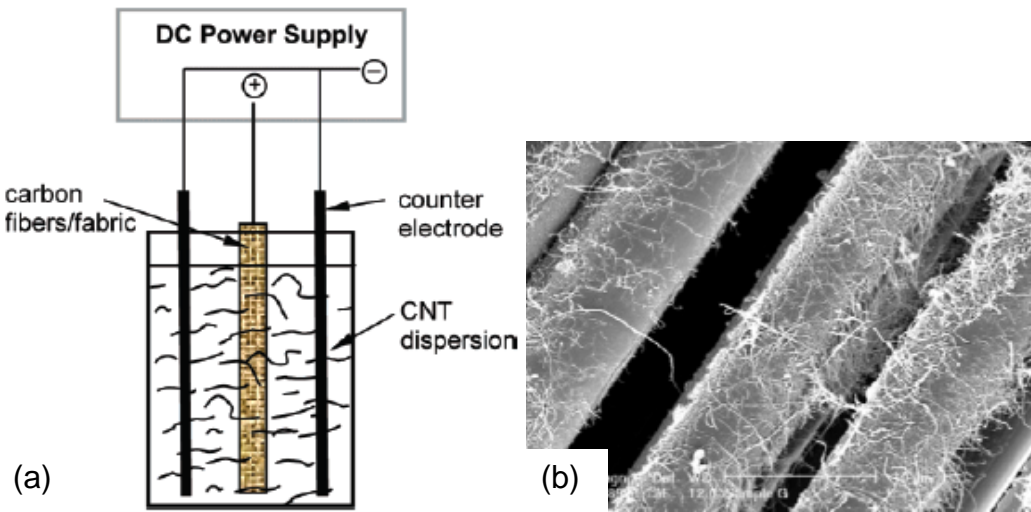


Figure 1.1: a) Deposition of carbon nanotubes on a carbon fibre mat using electrophoresis b) Scanning electron microscope (SEM) image of the deposited CNT on carbon fibres [3].

### 1.2.1.2 Hybrid Fibres

Thostenson *et al.* [6] grew carbon nanotubes on the surface of carbon fibres to improve interactions between fibres and the matrix. In this technique, a thin layer of catalyst was deposited on the surface of carbon fibres. Then CNTs were grown on carbon fibres using chemical vapor deposition (CVD). Figure 1.2 shows the SEM image of carbon fibres before and after CNT growth. An individual SWNT/CF was embedded inside the resin and the single-fibre fragmentation test was performed to evaluate the interfacial shear strength (For more details on the single-fibre fragmentation test please refer to the work done by Thostenson *et al.* [6]). A 15% improvement in interfacial shear strength was reported due to the addition of CNTs. An increase in the interfacial area of the fibre as well as an improvement in the shear modulus and yield strength of the CNT-modified resin near the interface might be responsible for this improvement.

In comparison to the electrophoresis technique (Section 4.1.1), this technique, however, has a main drawback that it cannot be easily applied to the whole fibre mats. A similar approach was used by other researchers to improve the interfacial shear strength of CF/carbon matrix composites [7, 8]. Here, while the improvement was verified qualitatively using SEM observations, no quantitative improvement was reported.

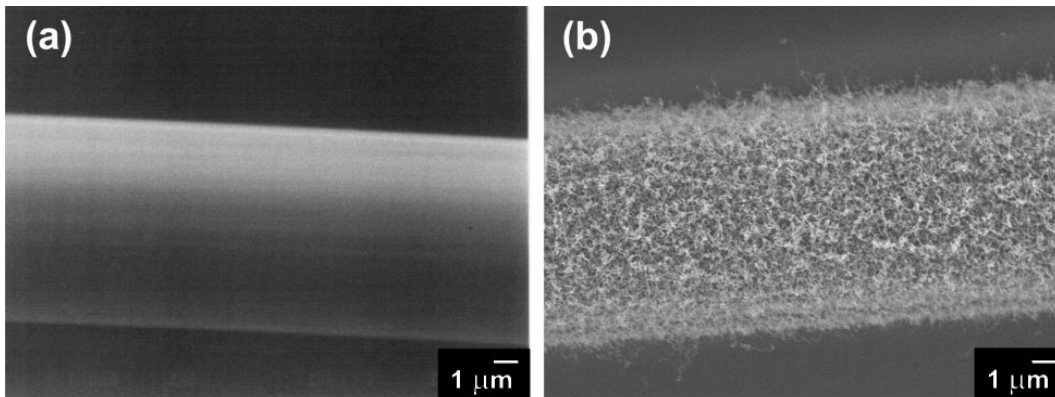


Figure 1.2: SEM image of a carbon fibre a) before and b) after CNT growth [6].

## 1.2.2 Sensing Applications

Carbon nanotubes have potential applications as sensors both in the form of an individual system and as inclusions inside composite materials. The motivation for sensing applications of carbon nanotubes in composites comes from the fact that carbon nanotubes are highly conductive. A review of this subject is contained in a recent paper by Li *et al.* [9].

### 1.2.2.1 Strain Sensing

Dharap *et al.* [10] were the first to use randomly oriented carbon nanotube (buckypaper) films as strain sensors. Figure 1.3-a shows a brass tensile sample with buckypaper attached as a strain sensor. An almost linear change in voltage was measured as a result of a linear change in the strain of the sample (Figure 1.3-b). In another work, a carbon nanotube/polymer thin film was used as a strain sensor, resulting in a measurement sensitivity 3.5 times higher than that of a traditional strain gauge [11].

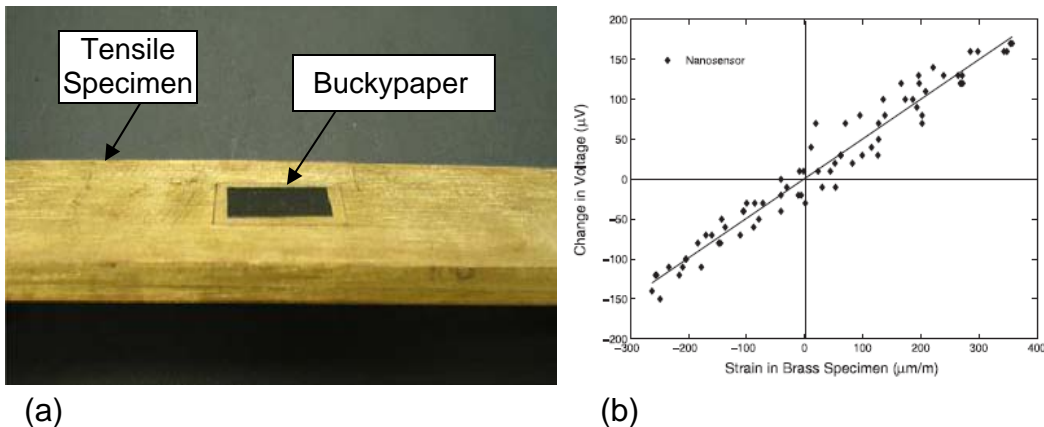
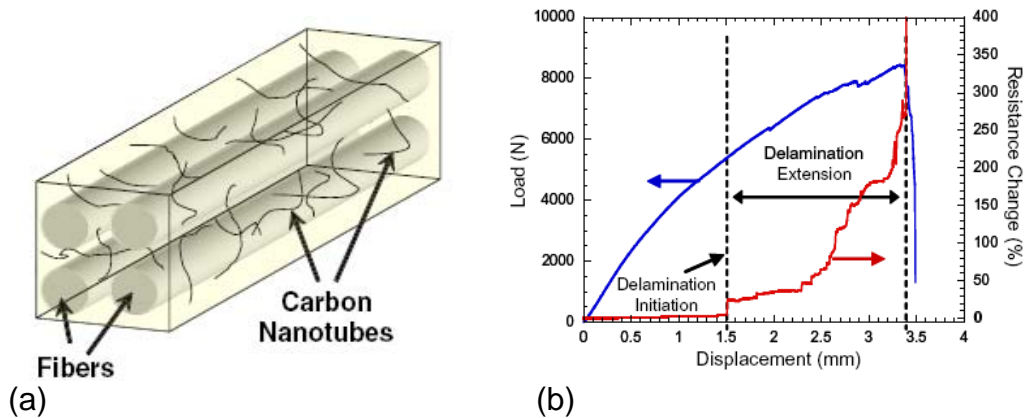


Figure 1.3: a) Buckypaper sheet as a strain sensor attached to a brass tensile specimen. b) Variations in voltage due to changes in the specimen strain [10].

### 1.2.2.2 Health Monitoring

Electrical conductivity measurements have been used for a long time to detect fibre damage in schemes for health monitoring of traditional composites [12]. As

an example, carbon fibres are conductive and any fibre fracture results in a change of resistance. However, as most polymers are not conductive, this method was not applicable to detect matrix-dominated fractures. Thostenson and Chou [13] suggested the application of CNT to detect these types of fractures. In other words, due to their small size, CNTs can easily penetrate the matrix-rich regions between fibres, and detect any damage caused by matrix failure (Figure 1.4-a). In this experiment, the CNT-modified resin was injected into a preform of traditional fibres. The specimen was then intentionally damaged to initiate a matrix-dominated failure. Figure 1.4-b shows the results of the delamination of a five-ply unidirectional composite in which the center ply was cut in a way which caused a ply delamination. The sample was then subjected to a tensile load while the resistance was simultaneously measured (Figure 1.4-b). For low strains, a linear change of load and deflection resulted in a linear increase in resistance (similar to strain sensing discussed in Section 1.5.2.1). By increasing the load, however, the delamination was finally initiated resulting in a significant increase of resistance (Figure 1.4-b). As a result, this technique can be effectively used to monitor the initiation of delamination.



**Figure 1.4: Application of CNT for composite health monitoring a) a schematic of CNT penetration between fibres b) detection of delamination due the change in CNT/polymer resistance [13].**

### 1.2.3 Application for Small-Volume Structures

Tsai *et al.* [14] manufactured a thermomechanical microactuator from CNT-reinforced nickel composites (Figure 1.5-a). Here, an appropriate amount of CNT was dispersed inside Ni to make a solution and electroplating was used to deposit the mixture on a chip. Microfabrication techniques were then utilized to manufacture the microactuators. An approximately linear increase in  $E/\rho$  was reported through an increase in the concentration of CNTs inside the Ni solution (Figure 1.5-b). A similar approach was utilized to manufacture Nickel-Phosphorus-CNT microactuators [15].

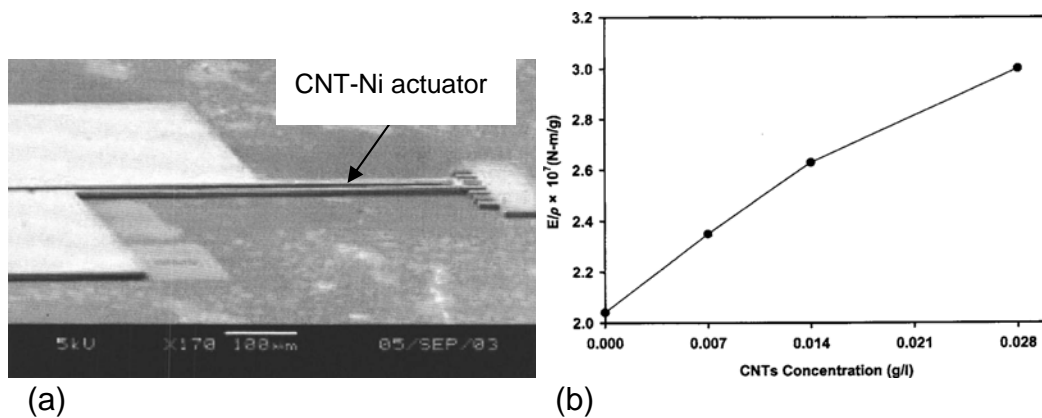
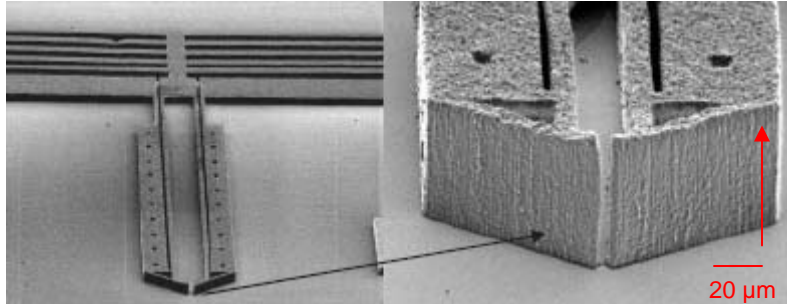


Figure 1.5: a) A composite thermomechanical microactuator made of CNTs and Ni b) an increase in mechanical properties due to increase in the concentration of CNT inside the solution [14].

Fang *et al.* [16] used carbon nanotube-reinforced polymer films to manufacture microgrippers (Figure 1.6). First, aligned carbon nanotubes were grown on the surface of a silicon substrate. The gaps between aligned carbon nanotubes were filled with parylene polymer using vapor-phase deposition. However, no information was given about the quality of impregnation. The nanocomposite was reported to exhibit an increase of nine times in the Young's modulus with respect to the pure polymer. In these measurements, the Young's modulus was determined from the flexural resonance frequency of the structures.



**Figure 1.6: CNT-reinforced polymer micro-gripper. Red arrow shows the direction for CNT alignment [16].**

### ***1.3 Objectives and Approach***

This research focuses on the potential applications of carbon nanotubes in reinforcing microstructures used in microelectromechanical systems (MEMS). The use of CNTs for this application is motivated by following factors.

- 1) Traditional fibres are not of an appropriate size for these applications.
- 2) Despite the fact that manufacturing techniques produce small quantities of CNTs, their output is still sufficient for the reinforcement of small structures.
- 3) There are opportunities to integrate the methods of manufacturing carbon nanotubes with conventional microfabrication methods to create CNT-reinforced microstructures.

In this work, a combination of theoretical and experimental frameworks has been chosen to investigate the applicability of CNT composites for small devices. This research thus has been divided into two different phases.

Phase one is a theoretical inquiry focused on the mechanical properties of microstructures. A combined framework of micromechanics and structural mechanics of composite materials is used to address different characteristics of carbon nanotube-based nanocomposites. This includes the choice of matrix as well as the type, volume fraction, aspect ratio and alignment of carbon nanotubes.

Special attention is paid to the potential application of CNT nanocomposites for microactuators, which are common elements of microelectromechanical systems. To increase the functionality of these structures, it is necessary to increase their speed of actuation and reduce the force necessary for actuation. As a result, materials with high elastic modulus and low density are the best candidates for the microactuators. Considering their low density and high Young's modulus, carbon nanotubes are inherently applicable to the reinforcement of microactuators. In phase one, the main parameters important for the design and manufacture of nanocomposite microactuators are specified.

The second phase of this research focuses on the synthesis and experimental characterization of carbon nanotube-reinforced polymeric thin films to establish a strong foundation for the eventual use of these materials in microstructures. Traditionally, there are different techniques for elastic characterizations of thin films such as tensile tests, flexural tests, bulge tests and nanoindentations. For polymer-based materials, however, each of these techniques demonstrates different disadvantages. As a result, a more robust technique is developed for the elastic characterization of polymer-based materials. This technique is a combination of bending and nanoindentation tests and is called the "nanoindenter-based bending test". This method is successfully used for elastic characterization of two classes of carbon nanotube-reinforced polymer thin films: dilute nanocomposites with low volume fraction (less than 1%) of carbon nanotubes, and buckypaper-reinforced nanocomposites with high volume fraction (30-40%) of carbon nanotubes. Finally, the results from these measurements are compared with predictions from theoretical models to develop guidelines for the use of nanocomposites as structural materials for microstructures.

The details of the two phases of research are organized into the following four chapters in this thesis.

Chapter 2 presents a detailed theoretical investigation on the utility of carbon nanotube-reinforced microactuators, with an emphasis on the identification of important parameters for the design of high-performance CNT-reinforced microactuators.

Chapter 3 presents the development of a new experimental technique for the elastic characterization of polymer-based thin films.

Chapters 4 and 5 present the results from the synthesis and experimental characterization of different classes of carbon nanotube-reinforced polymer thin films.

## Chapter 2

# Theoretical Investigation of Mechanical Properties of Carbon Nanotube-Reinforced Microactuators

### 2.1 Introduction

This chapter presents a detailed theoretical investigation of the utility of carbon nanotube-reinforced thin films for microactuators. The design of high-performance and reliable microactuators is essential for the development of microelectromechanical systems (MEMS) used in sensing, displays, communications, micromechanical testing instrumentation, and biochemical analysis [17, 18]. The actuators are typically simple beam and plate structures, with cross-sectional dimensions on the order of micrometers, and actuation is achieved either by applying an external force or by differential expansion and contraction.

A common example is a flexural-mode electrostatic actuator in which the structure deforms in response to an electrical potential difference applied between the actuator and a fixed proximal electrode [18]. A representative geometry for an electrostatic actuator is a microbeam of constant rectangular cross section, as shown in Figure 2.1. This structure is actuated by applying an electrostatic potential difference between the beam and the substrate.

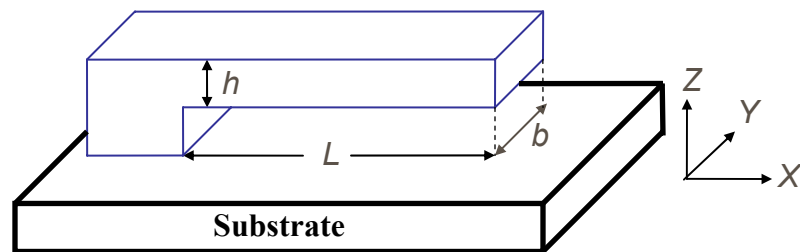


Figure 2.1: Schematic illustration of an electrostatically actuated microbeam.

## 2.2 Modelling of an Electrostatic Microactuator

This structure is typically modeled as an equivalent spring representing the beam and a capacitor standing for the electrostatic force between two plates (Figure 2.2). Two parallel forces are simultaneously applied to the central plate as described below.

### 2.2.1 Mechanical Force

This force ( $F_m$ ), a restoring mechanical force due to the beam stiffness, is [18]:

$$F_m = k(g_0 - g) \quad (2.1)$$

In Equation (2.1),  $g$  is the instantaneous distance between two capacitor plates, and  $g_0$  is this distance at equilibrium. The stiffness,  $k$ , of the spring is given by:

$$k = \lambda' \frac{EI}{L^3} \quad (2.2)$$

Here,  $\lambda'$  is a constant depending on the type of boundary conditions applied to the beam.  $I$  and  $E$  are the second moment of inertia and Young's modulus of the beam, respectively. In addition,  $L$  is the unsupported length of the beam.

### 2.2.2 Electrostatic Force

Electrical force ( $F_e$ ) is the result of an electrostatic attractive force between moving and fixed electrodes (red and blue plates in Figure 2.2) due to the application of a voltage ( $V$ ). Hence, this force is given by [18]:

$$F_e = -\frac{\varepsilon_r \varepsilon_0 L w V^2}{2g^2} \quad (2.3)$$

In this equation,  $\varepsilon_0$  and  $\varepsilon_r$  are the vacuum permittivity and relative static permittivity, respectively, and  $w$  is the width of the beam.

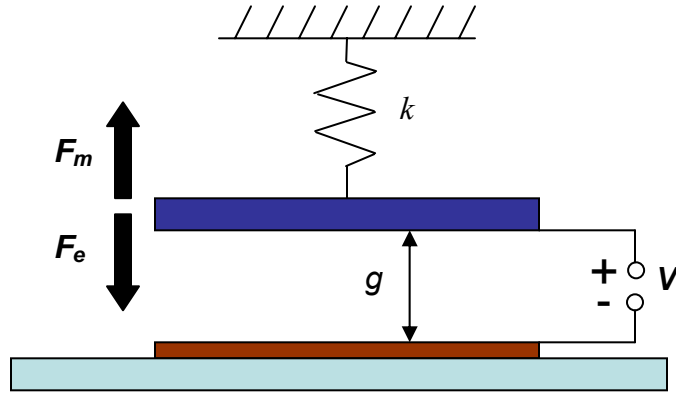


Figure 2.2: One-dimensional model of electrostatic micro-actuators.

## 2.3 Requirements of an Electrostatic Microactuator

Depending on their applications, electrostatic microactuators should satisfy different requirements. Two typical requirements of these structures, the high speed of actuation and the low activation voltage, are discussed below.

### 2.3.1 High Speed of Actuation

Since these structures are used as switches and oscillators for radio frequency (RF) applications (RF-MEMS), it is important to maximize their speed of reaction, to make them compatible with the speed required for other RF components. This speed ( $s$ ) is proportional to the frequency of the vibration of the beam ( $f$ ), which is given by:

$$f = \lambda'' \left( \frac{h}{L^2} \right) \sqrt{\frac{E}{\rho}} \quad (2.4)$$

In this equation, the first term ( $\lambda''$ ) is a constant, dependent on the boundary conditions of the beam. The second term is the geometry index ( $h$  is the beam thickness) and the third term is the material index ( $\rho$  is the density of the beam). For an isotropic material, the last term is equal to the longitudinal wave velocity

of materials ( $c$ ). Hence, a material with a higher  $c$  is required for high-speed electrostatic microactuators.

### 2.3.2 Low Actuation Voltage

The second important requirement of an electrostatic microactuator is low actuation voltage [18]. By equating electrical and mechanical forces (Equations (2.1) and (2.3)) this voltage is given by [18]:

$$V = \sqrt{\frac{2kg^2(g_0 - g)}{\epsilon_r \epsilon_0 Lw}} \quad (2.5)$$

Now, by replacing  $k$  from Equation (2.2), we obtain:

$$V = \lambda''' \sqrt{\frac{g^2(g_0 - g)h^3}{L^4}} \sqrt{E} \quad (2.6)$$

In this equation, the first term ( $\lambda'''$ ) is another constant, dependent on the boundary conditions and permittivity properties of the medium between the two plates. The second term is the geometry index and the third term ( $\sqrt{E}$ ) is the material index. In terms of material optimization, we have to decrease the beam's Young's modulus to decrease the actuation voltage.

## 2.4 Materials for Electrostatic Microactuators

Based on the previous discussion, the stiffness of the actuating structure dictates the force required for a specified deformation, and the natural frequency of vibration is a measure of the response time. Thus, many applications require the design of actuators with low stiffness and high natural frequencies of vibration [18]. One approach to achieve these objectives is to use advanced structural materials for manufacturing microactuators [19-21].

Microactuators in the current generation of MEMS are either monolithic structures or layered composites of laminated thin films. The selection of optimal materials for such actuators from the set of metals, ceramics and polymers has been discussed previously using the framework of the Ashby approach [19-21]. For a bending-mode actuator of given geometry and size, the stiffness and frequency are proportional to the Young's modulus,  $E$ , and longitudinal wave velocity,  $c = \sqrt{E/\rho}$ , respectively, where  $\rho$  is the density [22]. Thus, the material of choice for low-stiffness, high-frequency actuators should exhibit a combination of low modulus and high wave-velocity. A convenient method of identifying such materials is to use a materials selection chart with the longitudinal wave velocity plotted against the Young's modulus (Figure 2.3). The ideal candidate will occupy the top left-hand corner of this graph. Since this region is unpopulated, a trade-off is necessary to obtain either high-speed at the cost of high force (using ceramics and metals such as silicon, silicon carbide, aluminum and nickel), or to actuate at a low force by sacrificing the speed of operation (using polymers and elastomers) [20].

Consider now the location of yet another class of materials, namely, *fibre-reinforced, polymer-matrix, bulk composites* on Figure 2.3. Fibre-reinforced composites are not currently used in MEMS, but the graph suggests that these materials exhibit an attractive combination of high wave speed and relatively low modulus. Furthermore, due to the flexibility in choosing the polymer matrix [23], many other properties (e.g., optical, chemical, electrical) can be engineered into the structure, suggesting the possibility of developing *multifunctional* high-speed microactuators. The key questions now are whether these composites are compatible in size and processing requirements for integration with microsystems.

In order for a fibre to be used as reinforcement, the fibre diameter must necessarily be smaller than the cross-sectional dimensions of the composite structure [24]. Thus, conventional glass- and carbon-fibres cannot be used to reinforce micromachined structures since the fibre diameters range typically from

3 to 20  $\mu\text{m}$  [25]. On the other hand, there is an emerging class of one-dimensional *nanofibres* (nanotubes, nanorods, and nanowires) with diameters ranging from 1 to 100 nm [26], which are ideally suited in size to reinforce structures in MEMS. Carbon nanotubes are particularly attractive because they combine small size with exceptional mechanical properties [1, 27]. Thus, carbon-nanotube-reinforced composites are a natural starting point in the development of nanocomposites for microactuators.

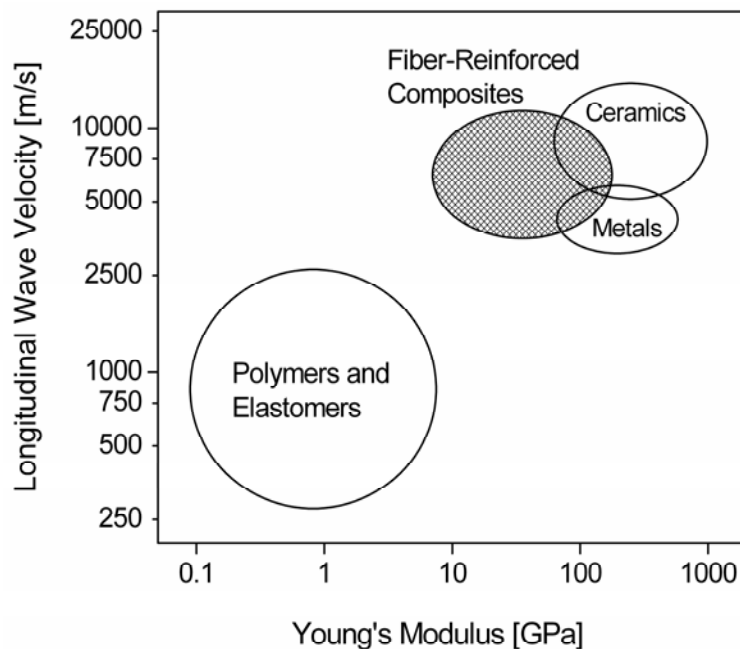


**Figure 2.3: Materials selection chart for microactuators.**

The synthesis and characterization of carbon nanotube-composites are topics of intense research activity (for recent reviews, please see Refs. [28-30]). However, the development of such nanocomposites for microactuators is still in its infancy [14-16]. Recent experimental studies report that reinforcing nickel microbeams with nanotubes leads to a modest increase of the longitudinal wave velocity [14], and that the force required for actuating polymer-matrix nanocomposites is significantly less than that for metallic- and ceramic actuators of comparable dimensions [16]. These results indicate the potential utility of these advanced materials for MEMS, but also highlight the critical need for developing *robust*

*structure-property relationships to guide the rational design of high-performance nanocomposite microactuators.* As a first step toward that objective, this chapter presents a detailed theoretical analysis of the elastic properties of carbon nanotube-reinforced microactuators.

## **2.5 Structure of Nanocomposite Actuators**

The structure considered for analysis is a long, slender, nanocomposite beam consisting of an isotropic matrix reinforced with carbon nanotubes, as shown in Figure 2.4. The cross-sectional dimensions of the beam are taken to be on the order of micrometers, which is representative of structures used in MEMS. The two independent elastic constants of the isotropic matrix are chosen to be the Young's modulus,  $E^M$ , and Poisson's ratio,  $\nu^M$ . Table 2.1 catalogs the nominal values of these properties, along with the density,  $\rho^M$ , and longitudinal wave velocity,  $\sqrt{E^M / \rho^M}$ , for typical metallic, ceramic, and polymeric materials used in MEMS.

There are two main types of nanotubes, namely, single-walled carbon nanotubes (SWNT) and multi-walled carbon nanotubes (MWNT) [1]. For purpose of analysis, the nanotubes are modeled as homogeneous, linear-elastic, cylindrical nanofibres of length  $L$  and outer diameter  $D$  (Figure 2.4). Theoretical and experimental studies from the literature indicate that this continuum representation is accurate provided that the aspect ratio of length to diameter is  $> 10$  [31, 32]. Since carbon nanotubes can be grown with aspect ratios of several thousand, the range considered for analysis is  $10 < (L/D) < 10^4$ .

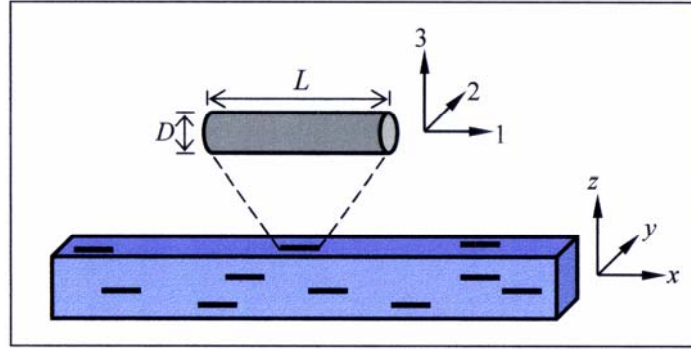


**Figure 2.4: Schematic illustration of a nanocomposite actuator beam with perfectly-aligned nanotubes embedded in an isotropic matrix**

**Table 2.1: Nominal properties of bulk materials [22, 25]**

Material	$\rho^M$ (kg/m <sup>3</sup> )	$E^M$ (GPa)	$\nu^M$	$\sqrt{E^M / \rho^M}$ (m/s)
Silicon carbide, SiC	3200	400	0.2	11100
Silicon, Si	2320	160	0.2	8300
Silicon dioxide, SiO <sub>2</sub>	2600	70	0.2	5200
Aluminum, Al	2643	70	0.3	5150
Nickel, Ni	8900	180	0.3	4497
Gold, Au	18900	70	0.4	1920
Polymethyl methacrylate, PMMA	1150	3.1	0.4	1641

In addition to individual carbon nanotubes, we also consider the use of arrays of single-walled carbon nanotubes (*SWNT-arrays*) as reinforcing fibres. This is motivated by the well-known difficulty in dispersing nanotubes in different host materials. Instead, nanotubes exhibit a pronounced tendency to form close-packed bundles (or arrays), which have different mechanical properties than individual SWNT or MWNT [33]. In the equivalent continuum representation, the diameter of the entire SWNT-array is denoted  $D$ , and all nanotubes in the array are assumed to have a length  $L$ .

The elastic properties of the nanofibres are obtained based on the assumption that carbon nanotubes and nanotube-arrays exhibit transverse-isotropy. Five independent elastic constants are required to describe the deformation of such structures. With respect to the 1–2–3 fibre coordinate system shown in Figure 2.4, these constants can be chosen to be:  $E_{11}^N$  (longitudinal Young’s modulus),  $E_{22}^N$  (transverse Young’s modulus),  $\nu_{12}^N$  (major Poisson’s ratio),  $G_{12}^N$  (in-plane shear modulus), and  $G_{23}^N$  (transverse shear modulus) [24]. The values of these constants are cataloged in Table 2.2 for SWNT [34], MWNT [35], and SWNT-arrays [36].

In general, nanotubes and nanotube-arrays can be introduced into the matrix with varying degrees of alignment with respect to the beam axes. In this chapter, bounds on the effects of alignment on elastic properties are obtained by analyzing two extreme cases. The first is denoted a *Perfectly Aligned Composite* in which the nanotubes are aligned with the fibre coordinates coinciding exactly with the global beam coordinates, as illustrated in Figure 2.4. This composite structure is transversely-isotropic and characterized by five independent effective elastic constants ( $E_{xx}^{AC}$ ,  $E_{yy}^{AC}$ ,  $\nu_{xy}^{AC}$ ,  $G_{xy}^{AC}$ , and  $G_{yz}^{AC}$ , where the superscript denotes *Aligned Composite*). The second case is denoted a *Perfectly Random Composites*, in which the orientation distribution of nanotubes is perfectly uncorrelated with the beam coordinates. The composite structure is then isotropic and characterized by two independent elastic constants given by  $E_{xx}^{RC}$  and  $\nu^{RC}$ , where the superscript denotes *Random Composite*.

**Table 2.2: Properties of nanotubes and nanotube-arrays [34-36]**

	(10,10) SWNT	(30,30) <sub>10</sub> MWNT	Array of (10,10) SWNT
Diameter (nm)	1.4	7.5	14.6
$E_{11}^N$ (GPa)	1060	800	580
$E_{22}^N$ (GPa)	6.63	15.58	9.4
$G_{12}^N$ (GPa)	442	320	17.2
$G_{23}^N$ (GPa)	17	4.1	2.47
$\nu_{12}^N$	0.16	0.14	0.18
$\rho^N$ (kg/m <sup>3</sup> )	1440	2090	1150

Having described the characteristics of the matrix and nanotubes, we next address the critical issue of interfacial bonding between nanotubes and matrix. The ability of nanotubes to reinforce the composite relies upon an efficient transfer of applied stress from the matrix to the nanotubes [24]. The magnitude of the load transfer is a function of the local chemistry and defect structure associated with the nanotube/matrix interface. Previous studies suggest that pristine nanotubes bond weakly to polymers, and that adhesion can be significantly improved by incorporating functional sidegroups on the nanotubes [37-40]. Here, it is assumed that the interfacial properties are optimized to give a *perfect load transfer* between nanotubes and matrix. In that sense, the analysis and results presented in the following sections constitute an *upper bound* on elastic modulus and longitudinal wave velocity for perfectly-aligned and perfectly-random nanocomposites.

## **2.6 Theoretical Mechanics of Nanocomposite Actuators**

The theoretical approach used in this chapter is based upon the classical continuum mechanics of composites reinforced with short fibres. Specifically, the

Young's modulus of the nanocomposite is obtained as a function of the nanotube orientation, dispersion, aspect-ratio, and volume fraction by using the Mori-Tanaka theory. These results are then combined with a structural model based on Euler-Bernoulli beam theory to determine the longitudinal wave velocity of the nanocomposite beam, as explained in the following sub-sections.

### **2.6.1 Theory of Mori-Tanaka**

As discussed in the previous section, to evaluate the functionality of a microactuator, its elastic modulus must be determined. For the case of CNT composites, there are different theoretical approaches to extract the elastic properties. Considering the nanometric size of carbon nanotubes, the best approach is perhaps a non-continuum model such as molecular dynamics in which the interaction of carbon nanotubes and polymer molecules is modeled more realistically. However, these models are computationally expensive. On the other hand, continuum models based on micromechanics are much less expensive computationally. As a result, the applicability of these techniques for modelling CNT-based composites has been verified by both theories and experiments [41]<sup>2</sup>. The continuum model based on the method of Mori and Tanaka is the most powerful micromechanics technique for elastic characterization of short-fibre composites [42] and is capable of addressing the following characteristics of short-fibre composites:

- 1) The geometry, i.e. aspect ratio, of the fibres or inclusions
- 2) The volume fraction of the inclusions
- 3) The alignment or orientation of the inclusions
- 4) The elastic properties of matrix and fibre (for both isotropic and anisotropic properties)

---

<sup>2</sup> For a more detailed review of this subject, the reader can refer to the M. Eng. thesis of the author (Reference 41).

All these issues are important for CNT composites. More specifically, carbon nanotubes show a highly anisotropic behavior. As a result, a major advantage of this method over other micromechanical approaches, for example the Halpin-Tsai technique [43, 44], is the possibility of considering anisotropic elastic properties of inclusions. Here, it is assumed that the interfacial properties are optimized to give a perfect load transfer between fibres and matrix. In that sense, the analysis will lead to upper bound on the elastic properties.

The objective is to obtain the elastic properties of a short-fibre composite, i.e. stiffness constants, as a function of the variables mentioned previously. The effective stiffness tensor of the composite ( $C^C$ ) is defined as

$$\bar{\sigma} = C^C \bar{\varepsilon} \quad (2.7)$$

where  $\bar{\sigma}$  and  $\bar{\varepsilon}$  are, respectively, the averaged stress and the averaged strain of the composite. It has been shown that this stiffness tensor can be obtained through the following equation [45]:

$$C^C = C^M + V_f \langle (C^I - C^M) A \rangle \quad (2.8)$$

Here,  $C^C$  and  $C^M$  are the stiffness tensors of the inclusions and the matrix, respectively.  $V_f$  is the volume fraction of inclusions, and the angular brackets denote the averaged quantity over all orientations. Moreover,  $A$  is called the concentration factor and is defined as:

$$\varepsilon^I = A \bar{\varepsilon} \quad (2.9)$$

Here,  $\varepsilon^I$  is the orientation dependent average strain in the inclusion. As a result, the knowledge of the concentration factor is sufficient to obtain the elastic properties of the composite.

The next two sections explain two approaches used to obtain the concentration factor for dilute media in which the inclusion interactions are neglected (Eshelby approach) and non-dilute mediums in which this effect will be considered (Mori-Tanaka approach). In other words, the Mori-Tanaka approach is the extension of Eshelby approach for higher concentrations of inclusions when interactions between them are not negligible. As a result, understanding the Eshelby approach is necessary and explained below.

### 2.6.1.1 Eshelby Approach

Internal stresses are commonly encountered in composite materials due to their inhomogeneous nature. As an example, when an external force is applied to a composite, the stiffer inclusion tends to deform much less than the softer matrix, which produces internal stresses. To calculate these internal stresses, no closed-form solution is available for an arbitrary inclusion. However, for a special case of an ellipsoid inclusion J. D. Eshelby developed an analytical method to calculate these stresses [46]. This is due to the fact that stresses inside an ellipsoid, with any aspect ratio, remain uniform. In this method, each inclusion is represented by an equivalent homogeneous inclusion, made from the matrix material, with a stress field equal to the actual inclusion. First, we can imagine that a specific area of a homogeneous medium with an ellipsoid shape is separated from the main body and experiences a shape change with a transformation strain ( $\varepsilon^T$ ) so that the strain is stress-free. As a result, to insert it back inside the medium, a surface traction should be applied to the sample to be fitted inside. After equilibrium, a constrained strain ( $\varepsilon^C$ ) will be imposed inside the inclusion relative to its initial shape before removal (Figure 2.5 shows this in detail). Considering the uniformity of stress and strain inside an ellipsoid inclusion, this stress ( $\sigma^I$ ) can be calculated from Hooke's Law

$$\sigma^I = C^M (\varepsilon^C - \varepsilon^T) \quad (2.10)$$

As a result, for any specific transformation strain, it is enough to calculate the constrained strain in order to compute the inclusion stress. Eshelby proved that the relation between the constrained strain and the transformation strain can be given by a tensor,  $S$ , later called the Eshelby tensor [46]

$$\varepsilon^C = S\varepsilon^T \quad (2.11)$$

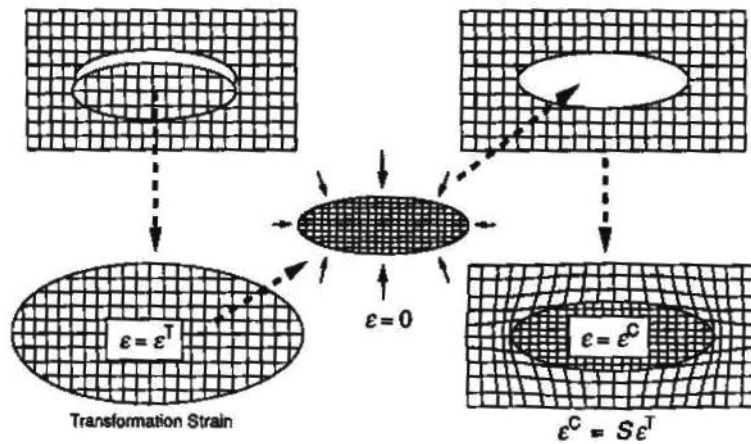


Figure 2.5: Definition of the equivalent homogeneous inclusion. First the homogeneous inclusion is subjected to a stress-free shape change. An appropriate surface traction is applied to the inclusion to put it back inside the matrix. After equilibrium, the constrained strain inside the inclusion can be obtained by the Eshelby tensor [47].

The Eshelby tensor is a function of the inclusion aspect ratio ( $s$ ) and the Poisson's ratio of the matrix,  $\nu^M$ . Table 2.3 summarizes the components of the Eshelby tensor. As a result, the inclusion stress is given by:

$$\sigma^I = C^M (S - I)\varepsilon^T \quad (2.12)$$

where  $I$  is the identity tensor. A more realistic case of a composite with a homogeneous inclusion subjected to an external loading is now to be considered. Since it is an elastically homogeneous medium, the external load causes a uniform strain ( $\varepsilon^A$ ) over the entire medium. As a result, the stress at each point is the summation of the external stress ( $\sigma^A = C^M \varepsilon^A$ ) and the internal stress ( $\sigma^I$ ):

$$\sigma^I + \sigma^A = C^M (\varepsilon^C - \varepsilon^T) + C^M \varepsilon^A \quad (2.13)$$

Here, the internal stress is obtained from Equation (2.10). We will now look at the real composite. It is clear that the effect of a real inclusion is very different from that of a homogeneous inclusion. However, since we have complete freedom to choose the stress-free misfit ( $\varepsilon^T$ ), it is possible to choose this parameter in such a way that the behavior of the homogeneous inclusion imitates that of the real inclusion. As a result, the constrained shape change of both the homogeneous inclusion and the real inclusion is equal to:

$$\varepsilon^I = \varepsilon^C + \varepsilon^A \quad (2.14)$$

The stress of the homogeneous inclusion is given by  $C^M (\varepsilon^C + \varepsilon^A - \varepsilon^T)$ . For the real inclusion, however, the stress is obtained from  $C^I (\varepsilon^C + \varepsilon^A)$ . By equating these two stresses, we obtain:

$$C^M (\varepsilon^C + \varepsilon^A - \varepsilon^T) = C^I (\varepsilon^C + \varepsilon^A) \quad (2.15)$$

**Table 2.3: Components of Eshelby tensor,  $S$ , for ellipsoidal and circular cylinder inclusions**

[47]

	<b>Ellipsoid</b> (aspect ratio, $s$ )	<b>Circular cylinder</b> ( $\lim s \rightarrow \infty$ )
$S_{11}$	$\frac{4Q}{3} + RI_3 + 2s^2T$	$0$
$S_{22} = S_{33}$	$Q + RI_1 + \frac{3T}{4}$	$\frac{5 - 4\nu^M}{8(1 - \nu^M)}$
$S_{23} = S_{32}$	$\frac{Q}{3} - RI_1 + \frac{4T}{3}$	$\frac{-1 + 4\nu^M}{8(1 - \nu^M)}$
$S_{21} = S_{31}$	$-RI_1 - s^2T$	$\frac{\nu^M}{2(1 - \nu^M)}$
$S_{12} = S_{13}$	$-RI_3 - T$	$0$
$S_{44}$	$\frac{Q}{3} + RI_1 + \frac{T}{4}$	$\frac{3 - 4\nu}{8(1 - \nu)}$
$S_{55} = S_{66}$	$2R - \frac{RI_1}{2} - \frac{1 + s^2}{2}T$	$\frac{1}{4}$
<i>For other <math>S_{ij}</math></i>	$0$	$0$
$I_1 = \frac{2s}{\sqrt{(1-s^2)^3}} \left[ s\sqrt{s^2-1} - \cosh^{-1}(s) \right]$		
$Q = \frac{3}{8(1-\nu^M)}$		
$R = \frac{1-2\nu^M}{8(1-\nu^M)}$		
$T = Q \frac{4-3I_1}{3(s^2-1)}$		
$I_3 = 4 - 2I_1$		

Now, using Equations (2.11) and (2.15), the strain misfit required for the homogeneous inclusion is obtained as

$$\varepsilon^T = -\left[(C^I - C^M)S + C^M\right]^{-1}(C^I - C^M)\varepsilon^A \quad (2.16)$$

By replacing this strain into Equation (2.13), the stress inside the real inclusion can be found as

$$\sigma^I + \sigma^A = -C^M(S - I)\left[(C^I - C^M)S + C^M\right]^{-1}(C^I - C^M)\varepsilon^A + C^M\varepsilon^A \quad (2.17)$$

Finally, Equations (2.9), (2.11), (2.14) and (2.16) together can be used to extract the concentration factor of the dilute composites:

$$A^{dil} = \left[I + S(C^M)^{-1}(C^I - C^M)\right]^{-1} \quad (2.18)$$

### 2.6.1.2 Mori-Tanaka Approach

The approach developed by Mori and Tanaka assumes that the average stress inside the matrix is uniform over the medium [48]. In other words, problems of fluctuation of stress components are eliminated through the application of an average stress. Following that, an energy method is utilized to consider the interaction between inclusions. Based on this approach, Benveniste [49] presented a close-form solution to calculate the concentration factor for a non-dilute composite:

$$A^{non-dil} = A^{dil} \left[ (1 - V_f)I + V_f \langle A^{dil} \rangle \right]^{-1} \quad (2.19)$$

Obviously, this is a more general form of the concentration factor and can be used for both dilute and non-dilute cases ( $V_f \rightarrow 0 \Rightarrow A^{non-dil} \rightarrow A^{dil}$ ).

## 2.6.2 Young's Modulus of Composite Microactuator

The properties of fibre-reinforced composites have been extensively studied and many different approaches have been developed to predict their elastic properties [24]. For the case of perfectly-aligned, dispersed, continuous fibres, a simple method for estimating the Young's modulus of the composite in the direction parallel to fibre axis,  $E_{xx}^C$ , is the volume-averaged rule-of-mixtures [24]:

$$E_{xx}^C = (1 - V_f)E^M + V_f E_{11}^N \quad (2.20)$$

where  $V_f$  is the volume fraction of nanotubes. This equation, however, does not take into account the aspect-ratio and orientation distribution of the fibres. Instead, it is necessary to apply a more computationally-intensive approach based on the well-known Mori-Tanaka theory [46, 48-52]. Previous studies have established the validity of this approach for analyzing the properties of composites reinforced with short, misaligned, carbon-fibre and carbon-nanotube reinforced composites [51, 52].

An essential ingredient of the Mori-Tanaka method is the approximation of short fibres as ellipsoidal inclusions of aspect ratio  $s = L/D$ . By combining Equations (2.8) and (2.19), the elastic constants can be calculated using the expression:

$$\mathbf{C}^C = \mathbf{C}^M + V_f \left\langle (\mathbf{C}^N - \mathbf{C}^M) \mathbf{A}^N \right\rangle \left[ (1 - V_f) \mathbf{I} + V_f \left\langle \mathbf{A}^N \right\rangle \right]^{-1} \quad (2.21)$$

where terms enclosed in the angular brackets represent the average over all orientations. The dilute concentration factor,  $\mathbf{A}^N$ , is given by Equation (2.18):

$$\mathbf{A}^N = \left[ \mathbf{I} + \mathbf{S}(\mathbf{C}^M)^{-1}(\mathbf{C}^N - \mathbf{C}^M) \right]^{-1} \quad (2.22)$$

where  $\mathbf{S}$  is the Eshelby tensor. The elements of the Eshelby tensor are functions of the aspect ratio of the inclusion,  $s$ , and Poisson's ratio of the matrix. Expressions for the independent elements of this fourth-rank tensor are listed in Table 2.3 for ellipsoidal inclusions. The above equations were used to calculate the elastic constants (including  $E_{xx}^{AC}$  and  $E_{xx}^{RC}$ ) of perfectly-aligned and perfectly-random composites as a function of nanotube aspect ratio, dispersion, and volume fraction.

Also tabulated in Table 2.3 are the elements of the Eshelby tensor for circular cylindrical inclusions, which are obtained in the limit  $s \rightarrow \infty$ . As a check on the numerical analysis, it was verified that the results for very large aspect-ratios ( $s = 10^4$ ) converge with the results obtained by using the Eshelby tensor for cylindrical inclusions.

### 2.6.3 Longitudinal Wave Velocity of Composite Microactuator

The longitudinal wave velocity of the composite is obtained by analyzing the flexural vibrations of the structure. This is accomplished by modelling the perfectly-aligned and perfectly-random composites as effectively homogeneous Euler-Bernoulli beams exhibiting transverse-isotropic and isotropic elastic behavior, respectively. The density of the nanocomposite beam (for both perfectly-aligned and perfectly-random orientations) is given by the rule-of-mixtures [53]:

$$\rho^C = (1 - V_f)\rho^M + V_f\rho^N \quad (2.23)$$

where  $\rho^C$ ,  $\rho^M$ ,  $\rho^N$  are the densities of the composite, matrix and nanotube, respectively. The density of carbon nanotubes is calculated from the total mass of carbon atoms in the enclosed volume [54]:

$$\rho^N = \frac{nM_w}{\pi N_a R^2} \quad (2.24)$$

where  $n$  is the number of the carbon atoms per unit length,  $M_w$  is atomic weight of carbon,  $N_a$  is Avogadro's number, and  $R$  is the radius of nanotube or nanotube-array. It directly follows from the theory of transverse vibrations of Euler-Bernoulli beams that the longitudinal wave velocity of perfectly-aligned composites is given by [55]:

$$c^{AC} = \sqrt{\frac{E_{xx}^{AC}}{\rho^C}} \quad (2.25)$$

For perfectly-random composite beams, the longitudinal wave velocity is [55]:

$$c^{RC} = \sqrt{\frac{E_{xx}^{RC}}{\rho^C}} \quad (2.26)$$

Equations (2.21) – (2.26) constitute a framework for calculating the effective materials indices of nanotube-reinforced electrostatic actuators. This framework is used to explore the effects of nanotube characteristics (type of nanotube, dispersion, aspect ratio, and volume fraction) and choice of matrix on the properties of perfectly-aligned and perfectly-random nanocomposite structures. The principal results are presented in the next section.

## 2.7 Numerical Results

First, we examine the dependence of the Young's modulus of the nanocomposite on the aspect-ratio of nanotubes (Figure 2.6). This graph shows the calculated curves for representative metallic (Ni), ceramic ( $\text{SiO}_2$ ), and polymeric (PMMA) matrix materials reinforced with single-walled carbon nanotubes at a volume fraction of 10%. For each material, two curves are shown corresponding to perfectly-aligned and perfectly-random orientation, respectively.

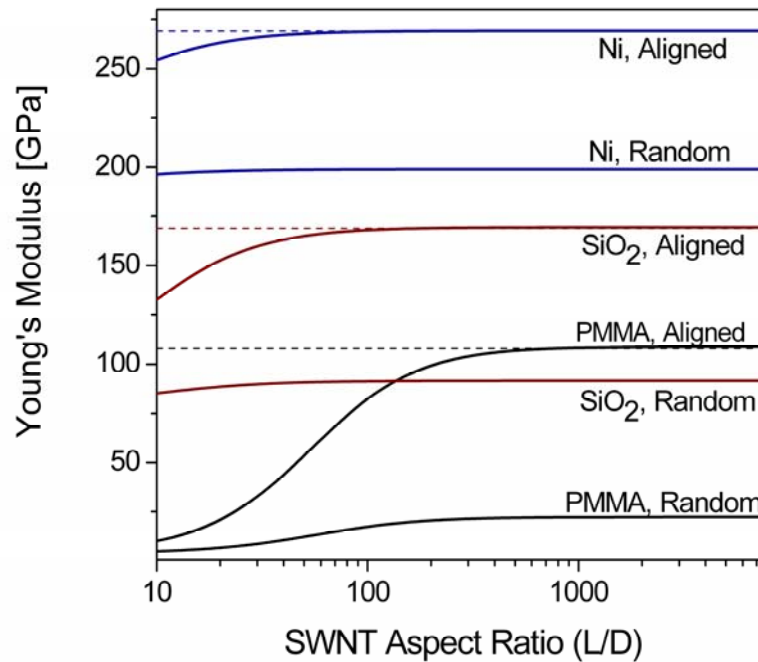


Figure 2.6: Effect of SWNT aspect ratio and alignment on Young's modulus.

Figure 2.6 shows that the Young's modulus of the composite is a strong function of nanotube aspect-ratio for small values of ( $L/D$ ). However, a critical value of aspect ratio can be identified beyond which the modulus is independent of ( $L/D$ ). The values of the critical aspect ratio range from 50 (for Ni) to 1000 (for PMMA). Furthermore, for perfectly-aligned nanocomposites with nanotube aspect ratios exceeding the critical values, the simple rule-of-mixtures (represented by the discontinuous lines on the graph) is accurate to within 1% in predicting the Young's modulus. As a corollary, the use of Equation (2.20) will

lead to considerable errors in predicting the elastic modulus of perfectly-random composites. These results are consistent with previous theoretical studies of macroscale composites [51] and nanotube-reinforced composites [52].

Next, consider the effects of nanotube volume fraction on the Young's modulus of the composite (Figure 2.7). Shown on this graph are the calculated values for three different types of nanofibre reinforcement (SWNT, MWNT, and SWNT-array) in perfectly-aligned and perfectly-random orientations. The matrix material is PMMA and, in all cases, the aspect ratio of the nanotube and nanotube arrays exceeds the critical value. The elastic modulus is observed to increase linearly with nanotube volume fraction, but the rate of increase is a function of the type of nanotube and alignment. Aligned, dispersed SWNT are the most efficient reinforcements. *Indeed, at a SWNT volume fraction of 15%, the modulus of the polymer-composite exceeds that of silicon.*

An additional intriguing observation follows from Figure 2.7. For a given volume fraction, aligned, SWNT-arrays lead to a higher composite modulus compared with dispersed, randomly-oriented SWNT. This observation has significant implications for manufacturing trade-offs between alignment, which typically requires micropatterning, and dispersion, which usually requires chemical functionalization of nanotubes.

The effects of nanotube volume fraction on the longitudinal wave velocity of the nanocomposite are shown in Figure 2.8. As before, the matrix material is PMMA and, in all cases, the aspect ratio of the nanotube and nanotube arrays exceeds the critical value. The wave velocity is observed to be a non-linear function of volume fraction and the rate of increase is a function of the type of nanotube and alignment. In particular, aligned SWNTs lead to a dramatic increase of the wave velocity of the polymer matrix. It was verified that the longitudinal wave velocities of these perfectly-aligned composites is predicted accurately by a rule-of-mixtures given by:

$$c^{AC} = \sqrt{\frac{E_{xx}^{AC}}{\rho^C}} = \sqrt{\frac{(1-V_f)E^M + V_f E_{11}^N}{(1-V_f)\rho^M + V_f \rho^N}} \quad (2.27)$$

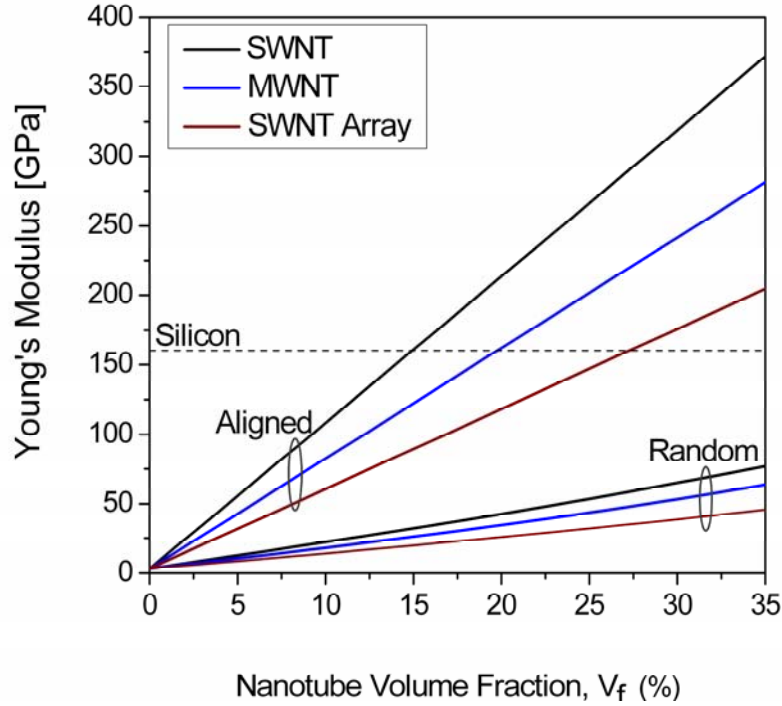


**Figure 2.7: Effect of volume fraction and alignment of SWNT, MWNT, and SWNT arrays on Young's modulus of PMMA-matrix nanocomposites. The Young's modulus of monolithic silicon is also shown for comparison.**

Finally, we consider the effects of the matrix properties on the longitudinal wave velocity of the composite. Figure 2.9 shows the calculated values for ceramic (Si, SiC), metallic (Al, Ni, Au) and polymeric (PMMA) materials reinforced with aligned, dispersed SWNT. The nanotube aspect ratio is chosen to be 1000, which exceeds the critical value for all cases. Whereas the longitudinal wave velocity of all materials increases with the volume fraction of SWNT, the rate of increase of PMMA is dramatic in comparison with the metals and ceramics. Indeed, Figure 2.9 suggests that the longitudinal wave velocity of the polymer-matrix nanocomposite can exceed those of Si and SiC. This result is primarily due to

material property values, as can be seen by considering the specific examples of silicon and PMMA reinforced with SWNT. The Young's modulus of the three materials differs by orders of magnitude, but their densities are comparable (Table 2.1 and Table 2.2). Thus, to a first approximation, we set  $\rho^N \approx \rho^M$ , and Equation (2.27) reduces to:

$$c^C = \sqrt{\frac{E^M}{\rho^M}} \sqrt{1 + \left( \frac{E_{11}^N - E^M}{E^M} \right) V_f} = c^M \sqrt{1 + \alpha V_f} \quad (2.28)$$

Here,  $\alpha$  is the normalized difference of elastic constants enclosed in the parenthesis and attains values of 5 and 320 for silicon and PMMA, respectively. Other polymers also exhibit similarly high values of  $\alpha$ , which indicates that nanotube-reinforcement is particularly effective for this class of materials.

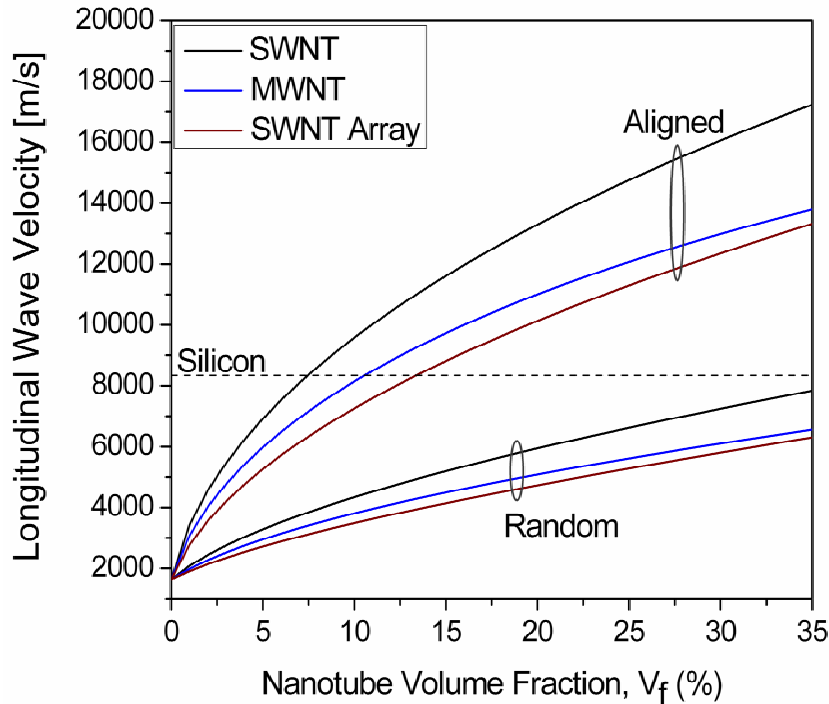


**Figure 2.8:** Effect of volume fraction and alignment of SWNT, MWNT, and SWNT arrays on the longitudinal wave velocity of PMMA-matrix nanocomposite. The wave velocity of monolithic silicon is also shown for comparison.

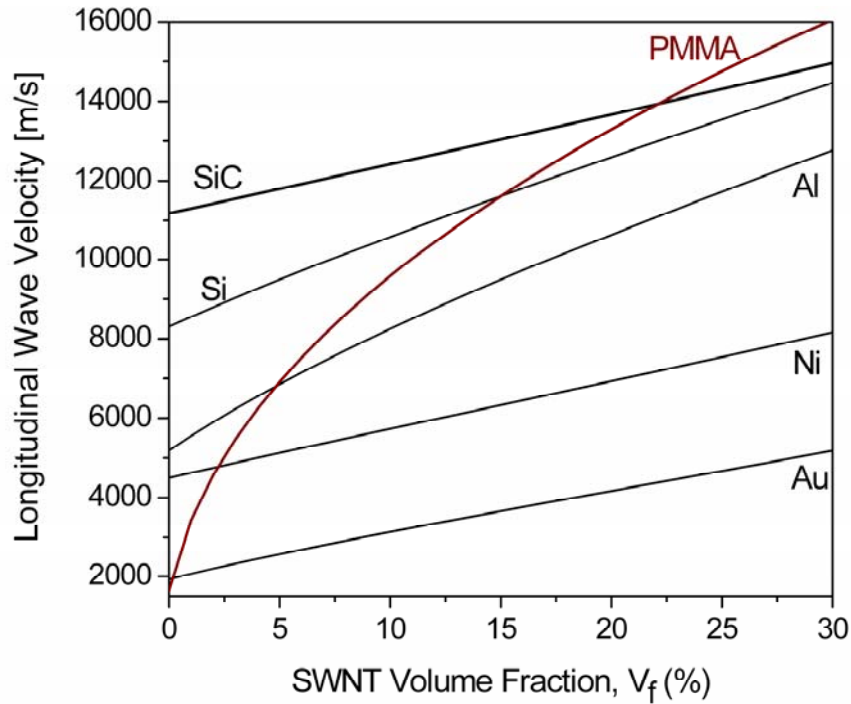
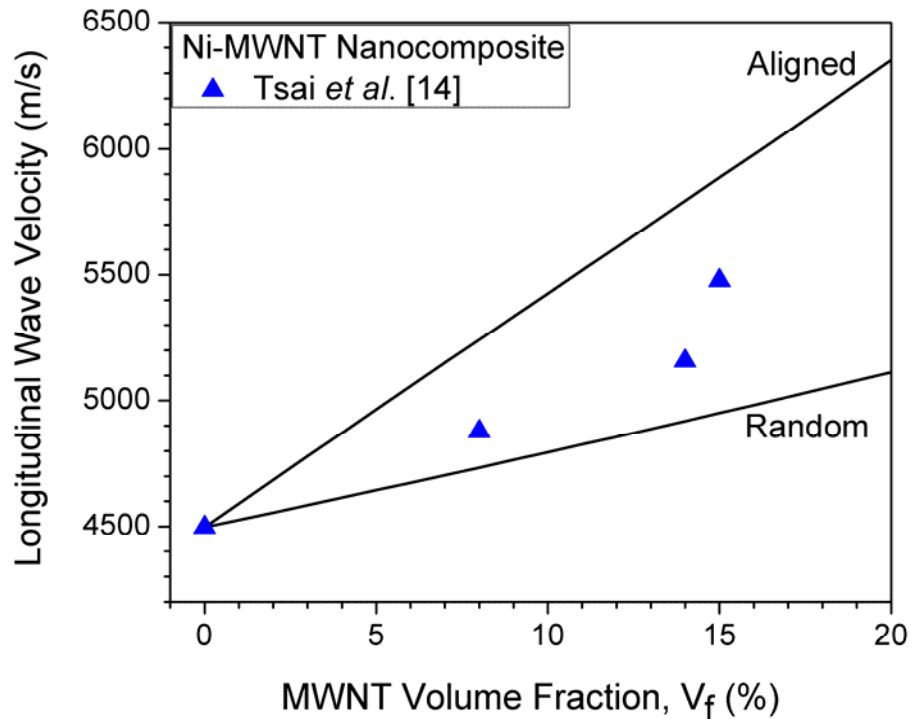


Figure 2.9: Effect of SWNT volume fraction on longitudinal wave velocity for representative metal-, ceramic- and polymer-matrix nanocomposites.

### 2.7.1 Comparison with Previously Reported Experiments

Tsai *et al.* [14] developed a process to surface-micromachine electrothermal actuators using a Ni thin film reinforced with multi-walled carbon nanotubes. Electrical conductivity measurements of these films suggested that the orientation of the nanotubes was neither perfectly-aligned nor perfectly-random in these films. Figure 2.10 is a plot of the measured longitudinal wave velocity at different volume fractions of MWNT. The curves are the calculated values for perfectly-aligned and perfectly-random orientations obtained from the Mori-Tanaka method.



**Figure 2.10: Comparison of measured longitudinal wave velocities of Ni-MWNT nanocomposite microresonators with calculated values for perfectly-aligned and perfectly-random composites.**

This comparison shows that the measurements fall within the bounds predicted by the continuum analysis. It is notable that the measured wave velocity increases only by 20% over pure nickel even at a relatively high nanotube volume fraction of 15%. The graph suggests that a further modest increase to 6000 m/s can be obtained by aligning the nanotubes in the nickel matrix.

There are few reliable measurements of the Young's modulus of micromachined nanocomposites, but a large number of reports have been published on the mechanical characterization of bulk nanocomposites [56-74], as discussed in the excellent review articles by Coleman *et al.* [29, 30]. This varied set of data includes different matrix materials (predominantly, polymers and elastomers such as poly vinyl alcohol (PVA), poly methyl methacrylate (PMMA), polypropylene (PP), and epoxy), different types of nanotubes (single-walled, double-walled, and

multi-walled nanotubes manufactured by chemical vapor deposition and arc discharge), different composite manufacturing methods (solution-processing, melt-processing, surface functionalization, *in situ* polymerization, infiltration, and surface micromachining<sup>3</sup>), and different measurement methods (resonance tests, tensile tests, dynamic mechanical analysis, and nanoindentation). As a representative example, consider the extensive set of tensile test data of poly (vinyl alcohol) ( $E^M = 1.9 \text{ GPa}$ ,  $\rho^M = 1300 \text{ kg/m}^3$ ) reinforced with MWNT [58, 59]. Figure 2.11 is a plot of the measured Young's modulus at different nanotube volume fractions. Also shown on this graph are the curves calculated for perfectly-aligned and perfectly-random nanocomposites using the Mori-Tanaka method.

We conclude that the theoretical bounds capture the entire range of measured values, indicating again the utility of the continuum analysis in estimating the limiting properties of nanocomposite materials. In addition, the difference between the calculated upper bound and measured value at a volume fraction of 1.5% is striking, and is indicative of the enormous difficulty in incorporating a high loading of aligned, dispersed nanotubes into polymer matrices.

Finally, for purpose of illustration only, we plot the measured Young's modulus against the longitudinal wave velocity for different polymer-matrix materials and different processing methods on a single graph (Figure 2.12). The wave velocities on this graph are calculated based on the density of the polymer matrix. Also shown for comparison is the predicted curve for PMMA reinforced with aligned, dispersed single-walled carbon nanotubes, and the coordinates of common metals (Al, Ni) and ceramics (Si, SiC).

---

<sup>3</sup> For more details on the nanocomposite processing techniques, please refer to Appendix 2

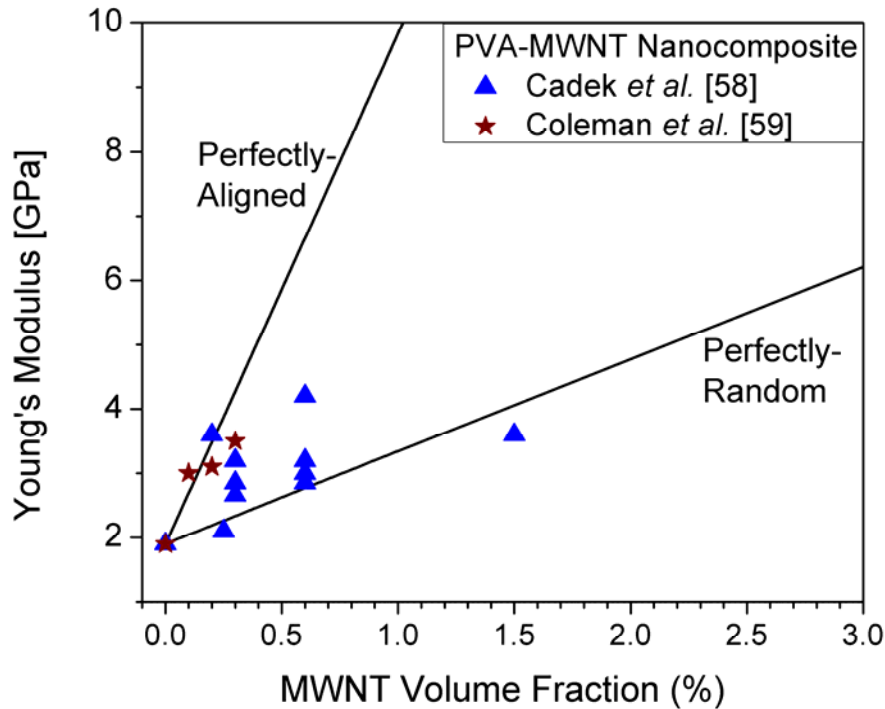


Figure 2.11: Comparison of measured Young's modulus of PVA-MWNT nanocomposites with the calculated values for perfectly-aligned and perfectly-random composites.

Figure 2.12 reinforces the observation that, under the ideal case, polymer-matrix nanocomposites can attain longitudinal wave velocities comparable to metals and ceramics, *but at significantly lower Young's modulus*. These materials, therefore, are excellent candidates for low-force, high-speed microactuators. However, there is an enormous gap between the state-of-the-art in nanocomposites technology (as represented by the data) and the calculated curve for PMMA reinforced with aligned, dispersed, SWNT. Bridging this gap will require the solution of several manufacturing challenges including dispersion, alignment, loading at high volume fractions, and optimization of nanotube-matrix interfacial properties.

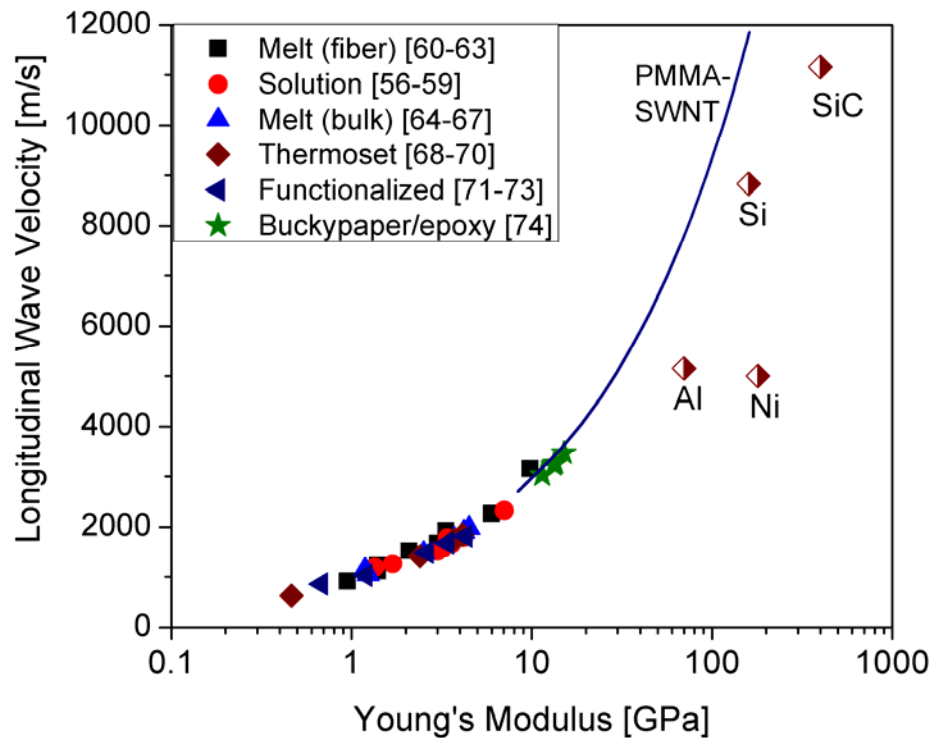


Figure 2.12: Materials selection chart for nanocomposite microactuators. The curve represents the calculated upper bound for PMMA-matrix reinforced with aligned SWNT.

## 2.8 Summary

Microelectromechanical systems are being developed for applications ranging from information systems and communication to portable power generation and medicine. Enhancing the functionality, performance, reliability, and manufacturability of MEMS requires the integration of advanced nanomaterials with micromachining process flows [75, 76]. However, materials processing, micromachining, and microscale mechanical property measurements are notoriously time-consuming and costly [17, 77]. The development of robust, scale-dependent, structure-property relationships for micromachined materials and structures is therefore essential to guide materials development.

In that spirit, this chapter investigated the utility of carbon-nanotube-reinforced composites as structural materials for high-speed multifunctional microactuators. The nanocomposite structure was modeled as an isotropic matrix reinforced with transversely-isotropic carbon nanotubes. Three different types of nanotubes, namely, single-walled carbon nanotubes (SWNT), multi-walled carbon nanotubes (MWNT), and arrays of single-walled carbon nanotubes (SWNT-array) were considered in this analysis. The elastic properties of the nanocomposite structure were analyzed by recourse to classical continuum mechanics within the framework of the Mori-Tanaka method, with the important assumption that the interfacial bonding between nanotubes and matrix is assumed to be optimized for perfect load transfer. The key results are listed below.

First, there exists a critical value of the aspect ratio of nanotubes beyond which the Young's modulus of the nanocomposite is independent of aspect ratio. This critical value ranges from 50 to 1000, depending upon the properties of the matrix material.

Second, the volume-averaged rule-of-mixtures is accurate to within 1% in predicting the elastic properties of perfectly-aligned nanocomposites in which the aspect ratio exceeds the critical value. This observation greatly simplifies the calculation of material property values for such nanocomposites.

Third, theoretical bounds obtained from Mori-Tanaka method are consistent with measurements reported in the literature. This comparison must be interpreted only in a qualitative sense because many important parameters (especially, orientation-distribution of nanotubes and strength of nanotube-matrix bonding) have not been reported in the experimental studies. The primary conclusion, therefore, is that the continuum analysis is a useful first step in the design and analysis of nanotube-reinforced composites.

Forth, reinforcement with carbon nanotubes enhances the axial Young's modulus and longitudinal wave velocity of nanocomposite beams. The extent of enhancement is a function of dispersion, alignment, aspect-ratio, and volume fraction of nanotubes, and the choice of matrix material.

Fifth, it is theoretically possible for polymers reinforced with aligned, high aspect-ratio, dispersed, single-walled carbon nanotubes to match the longitudinal wave velocities of common metals and ceramics. Thus, these nanocomposites are ideal candidates for low-force high-speed microactuators and for high-frequency micromechanical resonators.

Sixth, a qualitative comparison between the state-of-the-art in nanocomposite manufacturing technology and the predicted upper bound on property values highlights the enormous improvements needed in materials processing and micromachining to realize the potential of carbon nanotube-reinforced composites for low-force high-speed microactuators in MEMS.

We conclude by considering the implications of these results for two important classes of microdevices, namely electrostatic microactuators and flexural-mode microbeam resonators. Electrostatic actuators are widely employed in MEMS for applications ranging from displays and micro-flow controllers to sensing and communications [17-21]. Engineering the structural stiffness and natural frequency of bending vibrations is of paramount importance since these parameters govern the actuation voltage (which can be as large as several hundred volts in commercial MEMS) and the speed of actuation [20]. The results presented in this chapter demonstrate that, even within the current limitations on nanocomposite manufacturing technology, reinforcement with aligned carbon nanotubes is an excellent approach for tuning the stiffness and natural frequency of electrostatic microactuators. The bounds obtained from the Mori-Tanaka analysis can guide the trade-off between the increases in actuation voltage and

actuation speed for polymer-, metal- and ceramic-matrix nanocomposites used in MEMS.

The common requirements for flexural-mode microresonators used in sensing and communications are to increase the natural frequency of vibration (in the range 100 MHz to 1 GHz) and to minimize energy dissipation due to damping. For resonators operated at atmospheric pressure, energy dissipation is dominated by air-damping and is largely independent of material properties [21]. Therefore, nanotube composites are optimal candidates for such resonators. In some applications, however, the devices are operated at low pressures to reduce air-damping, and energy dissipation is then due to internal friction mechanisms [21]. A few studies have considered internal friction in laminated layered microbeams [78], but the extent of increase in damping due to nanotube reinforcement is unknown. Detailed experimental studies of structural damping in nanotube-reinforced microbeams are required to establish the utility of these nanocomposites for vacuum-operated microresonators.

## Chapter 3

# Elastic Characterization of Soft Thin Films through Nanoindenter-Based Bending Tests

### 3.1 Introduction

In this chapter, a new technique is developed to characterize the elasticity of soft thin films, i.e. polymer films and polymer-based composite films. The proposed technique is based on the bending behaviour of the films. A need for a new technique arises from the fact that traditional techniques such as tensile tests, bending and stretch tests, bulge tests and nanoindentation present difficulties for the elastic characterization of soft thin films. Table 3.1 summarizes the advantages and disadvantages of these traditional techniques. The primary issues during a tensile test are proper alignment and gripping of the sample [77]. This technique, however, is the only direct method of measuring Young's modulus. All other tests require the knowledge of the sample's Poisson's ratio. Bulge testing is a very simple tool used to characterize the elastic properties of different thin films. This technique has been successfully used to characterize mechanical properties of a few polymer systems [79, 80] but the precise measurement of the deflection of the polymer film – for example, by an optical interferometer – is difficult due to the low optical reflectivity of most polymers [81]. Moreover, this method is only applicable for films with no porosity. Elastic characterization of polymer films through nanoindentation techniques is now emerging. However, the traditional Oliver-Pharr method [82] typically overestimates the Young's modulus of polymers due to viscoelastic effects [83, 84]. Using nanoindentation testing, several researchers have tried different techniques to extract viscoelastic properties of polymer films from creep tests [85-87], stress relaxation tests [88], and dynamic tests [89, 90] or a combination of these tests [91, 92]. Compared to traditional techniques, these typically resulted in a more accurate estimation of Young's moduli. Results obtained through these techniques are, however, highly

dependent on theoretical assumptions, for example, linear versus non-linear viscoelasticity assumptions or the number of dashpot and springs. As a result, there is currently no standard technique to extract the Young's modulus of polymer films from these tests.

**Table 3.1: Advantages and disadvantages of traditional techniques for the elastic characterization of soft thin films**

<b>Test method</b>	<b>Advantage</b>	<b>Disadvantage</b>
<b>Tensile Tests</b>	<ul style="list-style-type: none"> <li>• Simplicity of test set-up</li> <li>• Direct measurement of modulus</li> <li>• Well developed theory</li> </ul>	<ul style="list-style-type: none"> <li>• Alignment</li> <li>• Gripping</li> <li>• Sample preparation for brittle samples</li> </ul>
<b>Flexural Tests</b>	<ul style="list-style-type: none"> <li>• Easy preparation of samples</li> <li>• Well developed theory</li> </ul>	<ul style="list-style-type: none"> <li>• Application of boundary conditions</li> <li>• Need for accurate force and displacement measurement</li> <li>• Sensitivity to measurement of the film thickness</li> </ul>
<b>Bulge Tests</b>	<ul style="list-style-type: none"> <li>• Simplicity of test set-up</li> <li>• Well developed theory</li> </ul>	<ul style="list-style-type: none"> <li>• Not applicable for porous films</li> <li>• Difficulties in accurate measurement of film deflections for most polymers</li> </ul>
<b>Nanoindentation</b>	<ul style="list-style-type: none"> <li>• Local characterization</li> <li>• Sophisticated commercial instrumentation for accurate measurement of forces and displacements</li> </ul>	<ul style="list-style-type: none"> <li>• Complex mechanical deformations</li> <li>• Viscoelasticity effects of soft films</li> <li>• Instrumental difficulty (thermal drift, tip calibration and machine compliance)</li> </ul>

The difficulties associated with elastic characterization of soft thin films using the traditional methods listed in Table 3.1 have motivated the development of new methods based on bending deformation under an applied point load [93-99].

In general, the governing equations of thin films under different point loads depend upon the magnitude of applied loads and properties of the film. For small loads, the deformation is dominated by the bending stiffness and the films can be considered as plates. However, with increasing load, the deformation is increasingly dominated by stretching and the films behave as membranes. The deformation of elastic clamped circular plates and membranes has been extensively studied and it has been established that the load-deflection

relationship is linear for plates and non-linear for membranes [100]. Films have been characterized in both plate and membrane regimes. (Please refer to [97, 98] for plate testing and [93-96, 99] for membrane testing.) In general, membrane testing is more useful for sub-micrometer thick films. This is partly due to the requirement of extremely small forces to characterize these films under plate deformation, which makes it convenient to use currently available instrumentation and characterize ultra-thin films as membranes. For thicker films, bending tests in the plate regime are more convenient and this is the method described in this chapter. A commercial nanoindenter (Hysitron TriboIndenter) capable of applying loads and measuring deflections in the micro-Newton and nanometer range, respectively, is used to perform the tests.

The following sections of this chapter are organized as follows. Section 3.2 describes the theory of deformation under a point load and describes criteria developed by Begley *et al.* [101] to distinguish between plate and membrane regimes. Section 3.3 presents a critical assessment of the underlying assumptions in the theoretical formulations by recourse to the method of finite-elements. Section 3.4 describes the test protocols for measuring the elastic properties of soft thin films using the TriboIndenter. Results are presented for epoxy and low-density polyethylene, and compared with values obtained from other techniques including tensile testing and nanoindentation.

## **3.2 Theory**

Figure 3.1-a shows a plate deflected under a central load,  $P$ , applied by a sphere. This load causes two simultaneous deflections: plate deformation,  $\delta_p$ , and contact indentation,  $\delta_c$ . These two deflections occur in series (Figure 3.1-b), and therefore we have

$$\delta_T = \delta_C + \delta_P \quad (3.1)$$

where  $\delta_T$  is the total displacement of the plate. The relationships between these deformations and the applied load are discussed sequentially below.

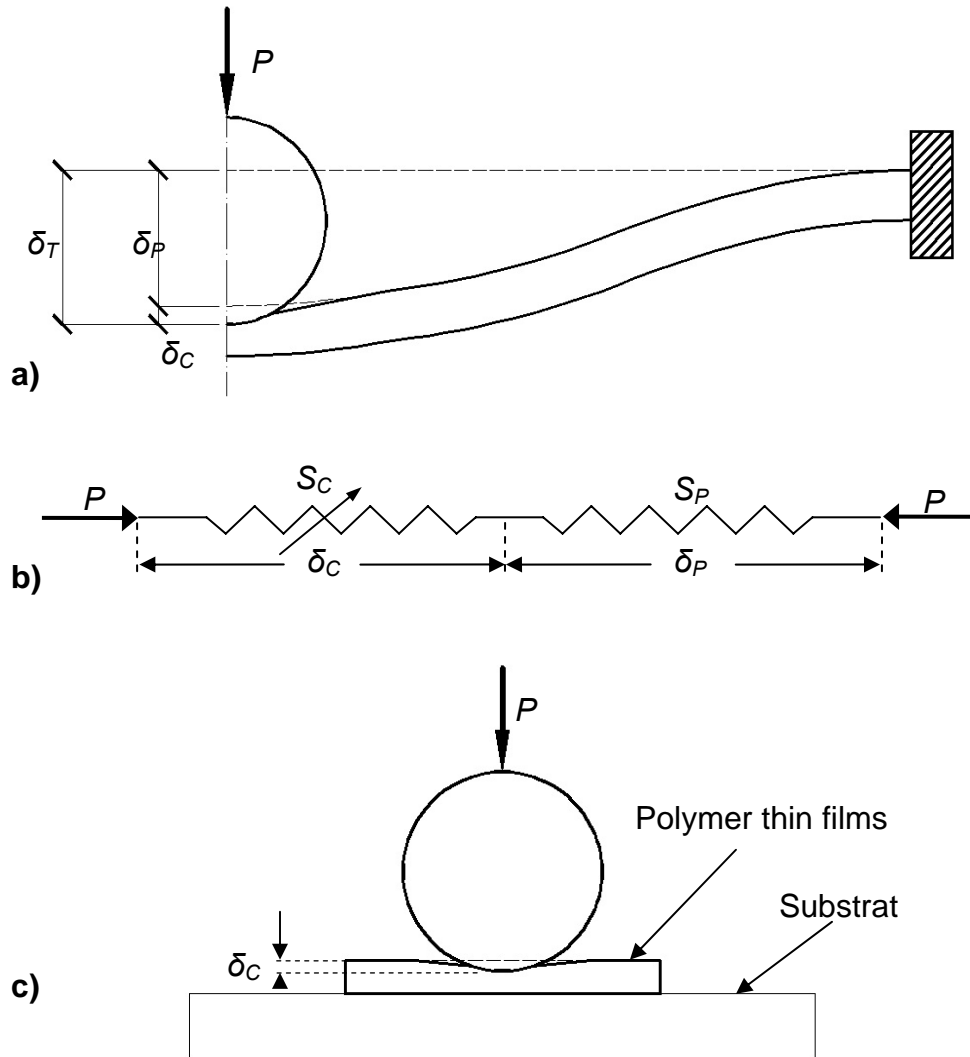


Figure 3.1: a) Contact indentation ( $\delta_C$ ) and plate deflection ( $\delta_P$ ) as a result of load  $P$ . b) A series of springs representing Figure 2-a.  $S_C$  and  $S_P$  are, respectively, the contact stiffness and the plate stiffness of the film. c) Experimental valuation of contact indentation ( $\delta_C$ ) through a thin film attached to a substrate.

### 3.2.1 Bending Deformation of a Clamped Circular Plate

The displacement of the centre of a circular plate clamped at its edge and loaded with a point load at its center is given by [100]:

$$\delta_p = \frac{3(1-\nu^2)}{4\pi E} \frac{a^2}{h^3} P \quad (3.2)$$

where  $P$  is the load applied at the center of a plate with radius  $a$  and thickness  $h$ ,  $E$  and  $\nu$  are, respectively, Young's modulus and Poisson's ratio of the plate.

Komaragiri *et al.* [101] have defined two dimensionless variables (one representing loading, the other corresponding to pre-straining) to identify an appropriate analytical solution for freestanding circular films under a point load. Since we are interested in films with no pre-strain, only the variable representing loading is relevant to the characterization of the film behaviour. This variable,  $\lambda$ , depends on the thickness, radius, Young's modulus and Poisson's ratio of the circular film as well as the force applied to its center as defined by:

$$\lambda(P, E, a, h, \nu) = \frac{\log\left(\frac{P}{2\pi E a h}\right)}{\log\left(\frac{h}{a\sqrt{12(1-\nu^2)}}\right)} \quad (3.3)$$

For a clamped circular film under a point load, using a boundary layer analysis, Begley *et al.* [101] prove that for  $\lambda > 3$ , the film behaves as a plate and Equation (3.2) is valid. As a result, Equation (3.3) can be used to obtain the maximum possible force ( $P_{\max}$ ) when  $\lambda=3$  for a thin film of known geometry and properties. If forces in excess of  $P_{\max}$  are applied to the film, the resulting deformation is not pure bending, but instead is a combination of bending and stretching.

### 3.2.2 Contact Indentation due to a Spherical Tip

Spherical tips are commonly employed for bending tests because they minimize local plastic deformation and have well-defined geometries and contact stiffness [102]. Analytical results for contact indentation of a clamped circular plate by a spherical tip are not available. Therefore, as a first approximation, the contact indentation is assessed using Hertzian contact mechanics. The depth of indentation ( $\delta_C$ ) caused by a spherical tip on an elastic half-space is given by [103]:

$$\delta_C = \sqrt[3]{\frac{9}{16} \frac{P^2}{RE_r^2}} \quad (3.4)$$

where  $P$  is the applied load,  $R$  is the tip radius and  $E_r$  is the reduced modulus (combined modulus) defined as [103]:

$$\frac{1}{E_r} = \frac{1-\nu^2}{E} + \frac{1-\nu_I^2}{E_I} \quad (3.5)$$

Here  $E_I$  and  $\nu_I$  are the known values of the elastic constants for the indenter.

### 3.2.3 Bending-Indentation of a Plate under a Spherical Tip

As a first approximation, Hertzian theory can be used for an estimation of the contact displacement. By substituting for  $\delta_P$  and  $\delta_C$  in Equation (3.1) from Equations (3.2) and (3.4), we obtain:

$$\delta_T = \sqrt[3]{\frac{9}{16} \frac{P^2}{RE_r^2}} + \frac{3(1-\nu^2)}{4\pi E} \frac{a^2}{h^3} P \quad (3.6)$$

Equation (3.6) provides a link between the applied force  $P$  and the measured total deflection of the plate,  $\delta_T$ . By measuring the geometric properties of the film (thickness and radius), assuming a value for the Poisson's ratio of the film, and using the known properties of the indenter (tip radius and elastic properties), the Young's modulus of the film can be extracted from measured load-deflection ( $P - \delta_T$ ) curves.

While Hertzian theory is a starting point for the evaluation of contact deformation, it typically results in an underestimation of the Young's modulus due to the surface roughness of the sample. This fact has been proved by both experiments [102] and simulations [104] and is more pronounced for shallower indents, i.e. by nanoindentation. As a result, a more accurate evaluation of the contact indentation can be obtained empirically by a set of spherical indentations on thin films attached to a substrate (Figure 3.1-c). This results in an explicit evaluation of the Young's modulus through:

$$E = \frac{3(1-\nu^2)}{4\pi} \frac{a^2}{h^3} \frac{P}{\delta_T - \delta_C} \quad (3.7)$$

The critical assumption in Equations (3.6) and (3.7) is the use of Hertzian contact mechanics or spherical indentations to estimate contact indentation on thin films. The validity of this assumption is examined in the next section using the method of finite-elements.

### **3.3 Finite Element Modelling**

A finite element model of the plate-bending test was created to validate the theory presented in the previous section. The commercial finite element package ANSYS 10.0 [105] was used to model nonlinear contact and large deformation based on continuum mechanics theory. The main advantage of using FEA software is that

the displacement contributions from plate bending and contact can be calculated separately. Two models were computed to validate the theory: a simple half-space to compute solely Hertzian elastic contact, and a full model representing the plate with corresponding boundary conditions undergoing bending and indentation.

A time-independent, isothermal, static solution is used to solve the deformation process. The solution is divided into multiple loadsteps. The FE problem is displacement-driven, meaning that a displacement is prescribed on the modeled indenter and ANSYS calculates the required force for each loadstep. The force applied by the indenter, the displacement of the plate and the displacement of the indenter tip are monitored at each loadstep. Contact is modeled between the indenter and the plate. Therefore, for each loadstep, the penetration of the indenter into the plate and the contact area is also monitored. A combination of penalty parameters and Lagrange multipliers, known as the augmented Lagrange contact algorithm [105, 106], is used to determine the force contributions from both bodies during the deformation. This allows the solver to reach equilibrium at each load step. Due to the small strain in the lateral direction near the indenter tip, friction is considered negligible. Thus, a friction coefficient of zero is used. The augmented Lagrange contact algorithm determines the force contributions from both bodies during the deformation. All materials are modeled as linear elastic, isotropic, homogeneous continua.

Due to the symmetry of the boundary conditions and to minimize the degrees of freedom, the problem was reduced to a 2-dimensional axisymmetric representation; see Figure 3.2 and Figure 3.4. Due to the small ratio of the plate stiffness to the indenter tip stiffness, the indenter deformation was considered negligible. Hence, the indenter was represented as an arc, further reducing the total number of degrees of freedom. A finite element study was also conducted to confirm this assumption. The model was then discretized using 8-noded, quadratic, PLANE 183 elements [105]. This method was chosen to properly represent the curvature of the indenter. The center of the modeled film is

constrained against lateral motion and all nodes respond with  $360^\circ$  symmetry. For the plate model, the circumference has a cantilever constraint. The spherical indenter was reduced to an axisymmetric cross section with a radius of  $100\mu\text{m}$ ; the same radius as the indenter. The mesh sizes of the half-space and plate are locally refined at the point of contact with the indenter. Element sizes range from  $50\text{nm} \times 50\text{nm}$  at the point of contact to approximately  $40\mu\text{m} \times 40\mu\text{m}$  distant from the contact area. Element dimensions are selected to optimize computational time, result accuracy and desired refinement. Models have approximately 3000 elements and 200 loadsteps.

The validity of the first finite element (FE) model – the spherical indenter in contact with the half-space (Figure 3.2) – was established by comparison with Hertzian elastic contact theory (Equation (3.4)). The half-space is modeled in ANSYS as a large ( $250\mu\text{m} \times 250\mu\text{m}$ ), 2-dimensional axisymmetric body. As the indent depth is always less than  $1\mu\text{m}$ , i.e. less than 0.5% of the subspace height, the boundary conditions have a negligible effect and the model can be considered as a half space. The elastic half-space is modeled with a Poisson's ratio of 0.4 and five different moduli: 0.1, 0.5, 1, 5 and 10 GPa. The indenter is rigid.

Figure 3.3 compares the results from the first phase of the FE model with the Hertzian contact mechanics. The contact stiffness ( $P:\delta_C$ ) is plotted as a function of the applied force for five representative polymers. The comparison between the FE model and Hertzian contact theory is used here to confirm the validity of our finite element model. FEA and Hertzian mechanics show very good agreement, as after contact establishment between the tip and the sample, the error between the FE model and the Hertzian theory remains lower than 5%. This error decreases to below 3% as the load is increased.

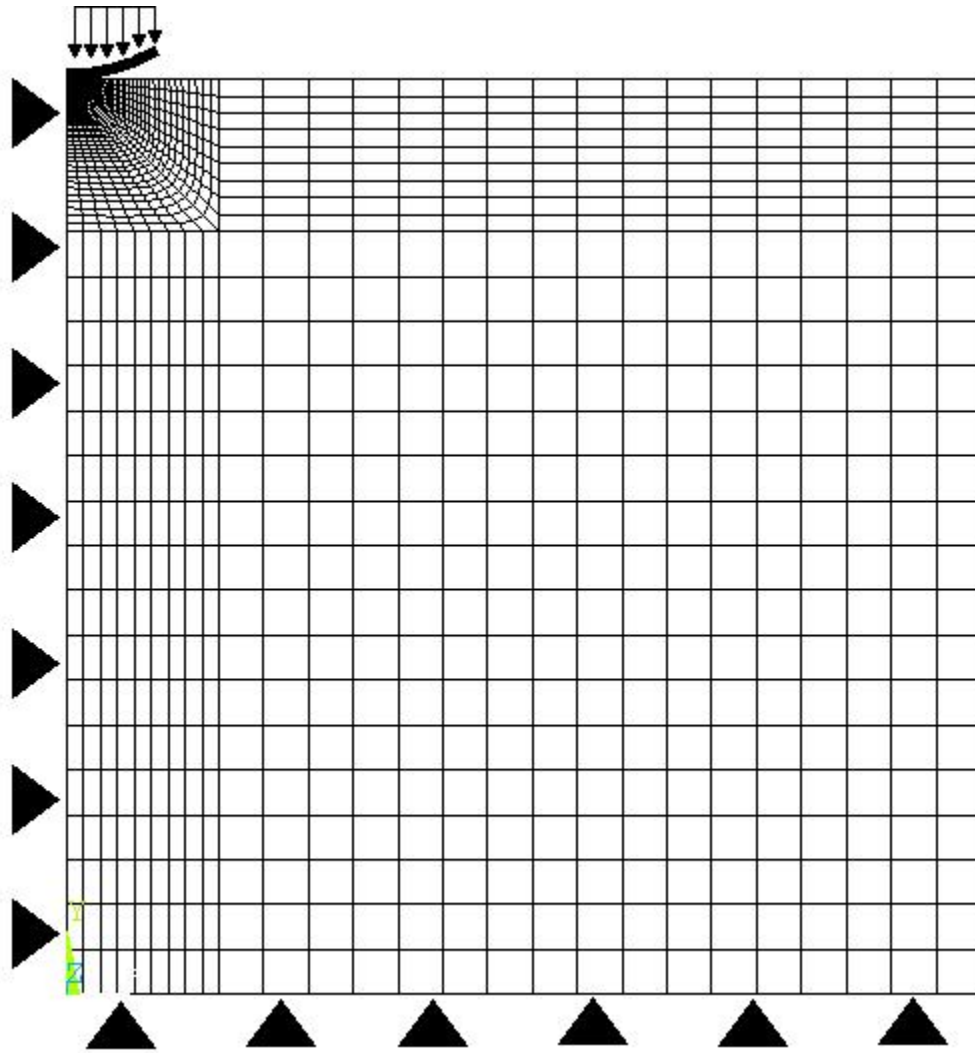


**Figure 3.2: Mesh, geometry and boundary conditions of the FE model of Hertzian contact mechanics. Indenter is modeled as an arc to reduce numbers of elements.**

With Hertzian contact validated, the plate model can be computed. The thickness of the plate is modeled to be 50, 100 and 150 $\mu\text{m}$ . For each thickness, Young's modulus values of 0.1, 1 and 10 GPa are studied, resulting in 9 different cases. The Poisson's ratio is assumed to be 0.4 (constant) and the plate has a radius of 1.25mm. The indenter is modeled as a rigid solid (See Figure 3.4 for a typical representation of this problem). The applied load is limited to the plate regime for this analysis according to Equation (3.3).

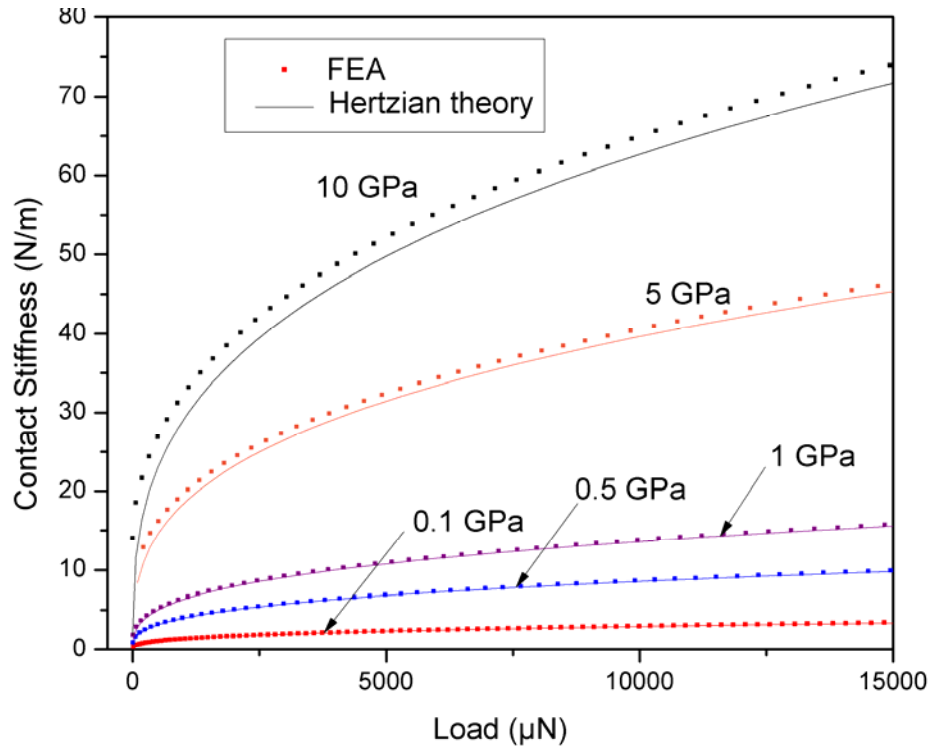


Figure 3.3: Comparison between FEA and Hertzian contact theory for contact stiffness. The Young's modulus of the film for each case is indicated on the figure.

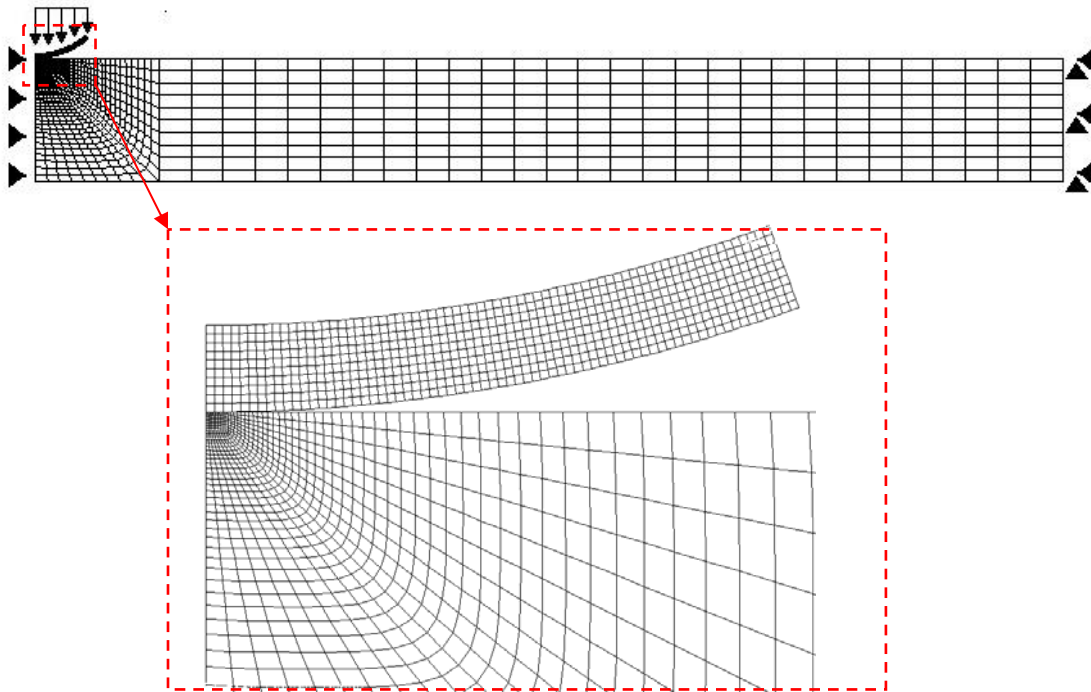


Figure 3.4: a) Mesh, geometry and boundary conditions of the FE model of a clamped circular plate under a point load.

Figure 3.5 compares the contact and bending displacement as obtained from the FE model and the theory, for the specific case of  $h=100 \mu\text{m}$ ,  $E=1 \text{ GPa}$ . The error between these two methods is plotted against the scale on the right-hand side of the figure. The vertical dashed line shows the maximum allowable force for this specific geometry to remain in the plate regime, according to Equation (3.3) where  $\lambda=3$ . The error between the Hertzian calculations and the FE model for contact displacement increases from 0 to less than 9%. This result is consistent with those presented in Figure 3.3, as in both cases, the FE model slightly underestimates the contact indentation. In the comparison between the plate theory and the FE model, the error remains almost constant (less than 4%) for all loads, and the FE model slightly overestimates the displacement. Although results for only one specific thickness and modulus were presented here, all other eight cases gave very similar results (Table 3.2). In summary, errors of contact indentation never exceeded 11% and those of plate displacement remain less than 7%. It is also worth mentioning that these errors were almost independent of the film's Young's modulus and moderately decreased as the film thickness was reduced from  $150 \mu\text{m}$  to  $50 \mu\text{m}$ .

**Table 3.2: Difference between Hertzian theory, plate theory and FE results**

Film thickness	h= 50 $\mu\text{m}$		h= 100 $\mu\text{m}$		h= 150 $\mu\text{m}$	
	Hertz	Plate	Hertz	Plate	Hertz	Plate
0.1 GPa	7.53%	0.79%	9.30%	3.31%	10.59%	6.95%
1 GPa	7.56%	0.79%	9.32%	3.31%	10.61%	6.95%
10 GPa	7.51%	1.38%	9.35%	3.31%	10.60%	6.98%

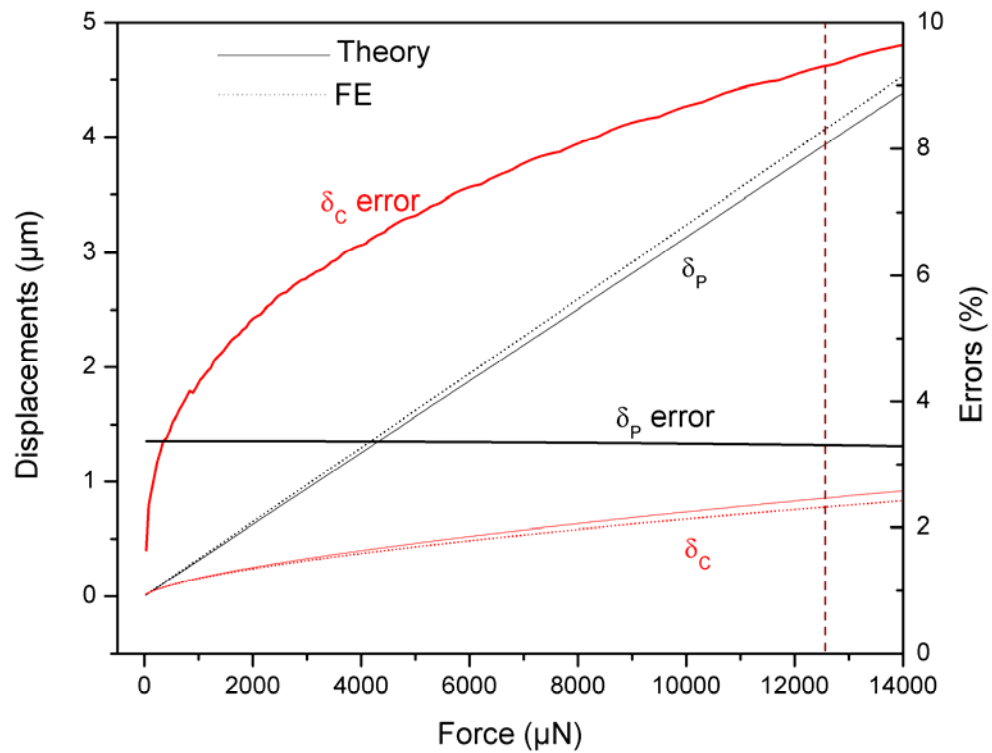


Figure 3.5: Comparison between the plate theory, the Hertzian theory and the FE model for  $h=100 \mu\text{m}$  and  $E=1 \text{ GPa}$ . Associated errors between theories and the FE model are represented. Vertical dashed line shows  $P_{\text{max}}$ .

### 3.4 Experimental Protocols

#### 3.4.1 Nanoindenter-Based Bending Tests in the Plate Regime

The soft polymer and carbon-nanotube reinforced polymeric films of interest have Young's modulus values ranging from 0.1 GPa to 10 GPa, and thickness ranging from 1  $\mu\text{m}$  to 100  $\mu\text{m}$ . The proposed test aims at utilizing a commercial nanoindenter (Hysitron TriboIndenter) to apply loads and measure deflections. This instrument is capable of applying loads ranging from 10  $\mu\text{N}$  to 15000  $\mu\text{N}$ , and can measure deflections with a resolution of 1 nm. The maximum deflection permitted by the instrument is 5  $\mu\text{m}$ . Thus, the first task is to establish the

conditions under which the test can be performed such that the deformation is within the plate regime.

In order to ensure that the film is under clamped boundary conditions, a jig was designed such that the film is clamped between two plates. Figure 3.6 shows an exploded schematic diagram and photograph of the jig. The constraints imposed by the transducers and loading head of the TriboIndenter lead to a minimum value of 1.25 mm for the radius of film that can be tested (This fact is further explained in Section 3.4.2).

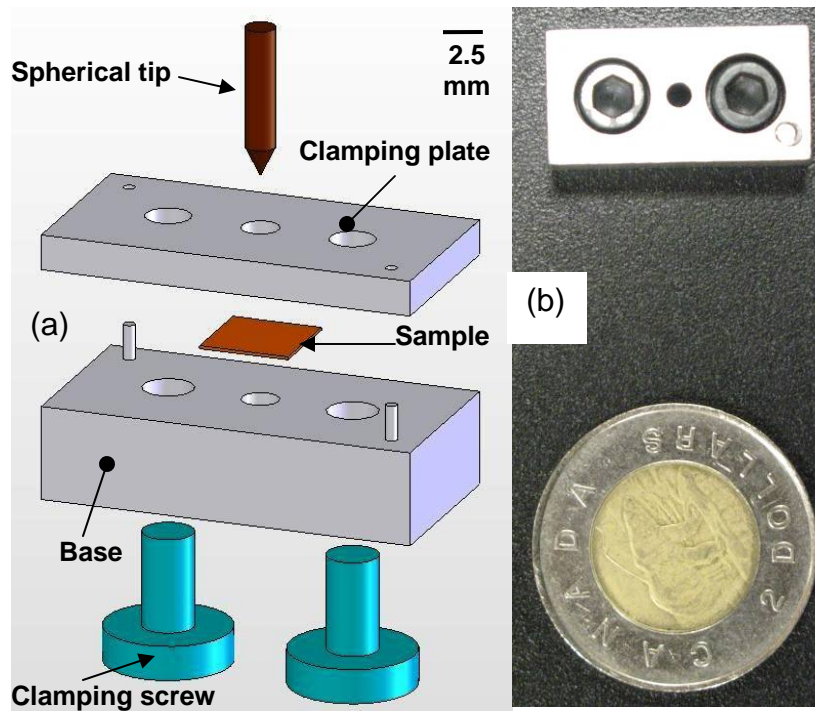


**Figure 3.6: a) A schematic design of the fixture and its components. b) Top view of the fixture**

Figure 3.7 is a graph of the dimensionless parameter  $\lambda$  as a function of the maximum applied load. The region corresponding to plate deformation ( $\lambda = 3$ ) is highlighted, and limits corresponding to the loading capabilities of the Hysitron TriboIndenter are indicated. As the load increases, the deformation shifts from

plate-like behaviour to mixed plate-membrane deformation. Figure 3.7 can be used to guide the analysis of different films using the proposed technique. For example, consider films operating at the practical limits of a small force of  $10 \mu\text{N}$  and a film radius of  $1.25 \text{ mm}$ . In this case, the minimum film thickness corresponding to plate deformation is  $30 \mu\text{m}$  and  $10 \mu\text{m}$  for Young's modulus of  $0.1 \text{ GPa}$  and  $10 \text{ GPa}$ , respectively.

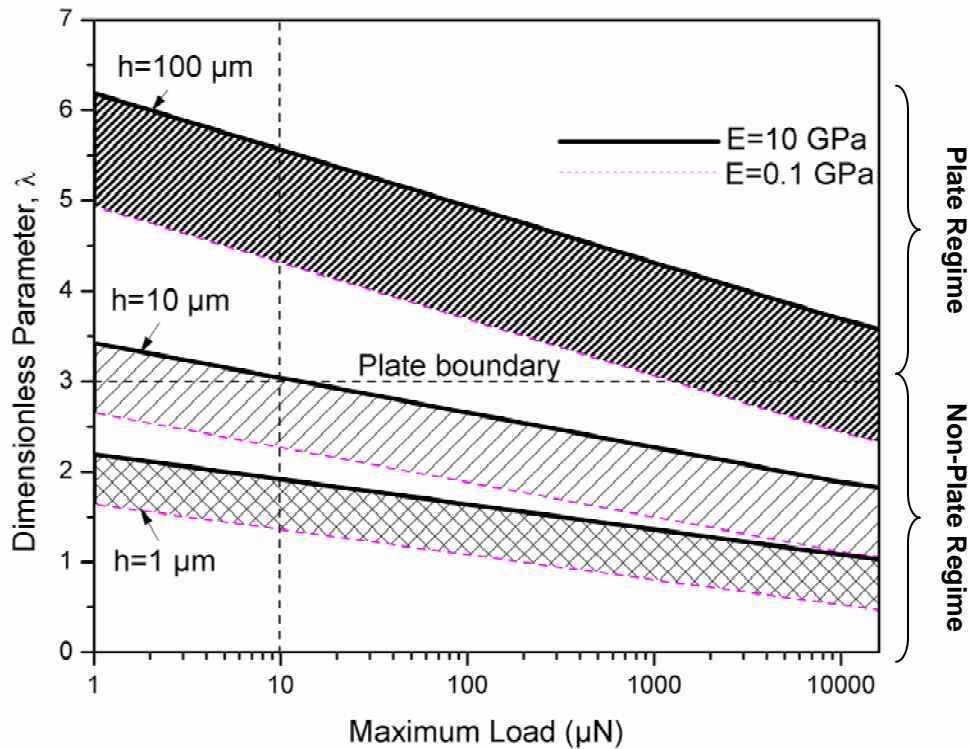


**Figure 3.7: Effect of the maximum load on the behaviour of 1, 10, and  $100 \mu\text{m}$  films for a typical range of polymers. The vertical dashed line shows the minimum limit of typical Hysitron indenters.**

A second consideration in the choice of the maximum applied load is the ratio of the bending deformation to contact indentation. This ratio must be maximized in order to minimize errors in the assessment of contact indentation. This consideration implies that the applied load must be as high as possible while maintaining the structure in the plate deformation regime. Figure 3.8 displays

$P_{\max}$  as a function of the Young's modulus for various film thicknesses. The two horizontal dashed lines are the lower and upper limits of feasible loads using the TriboIndenter.

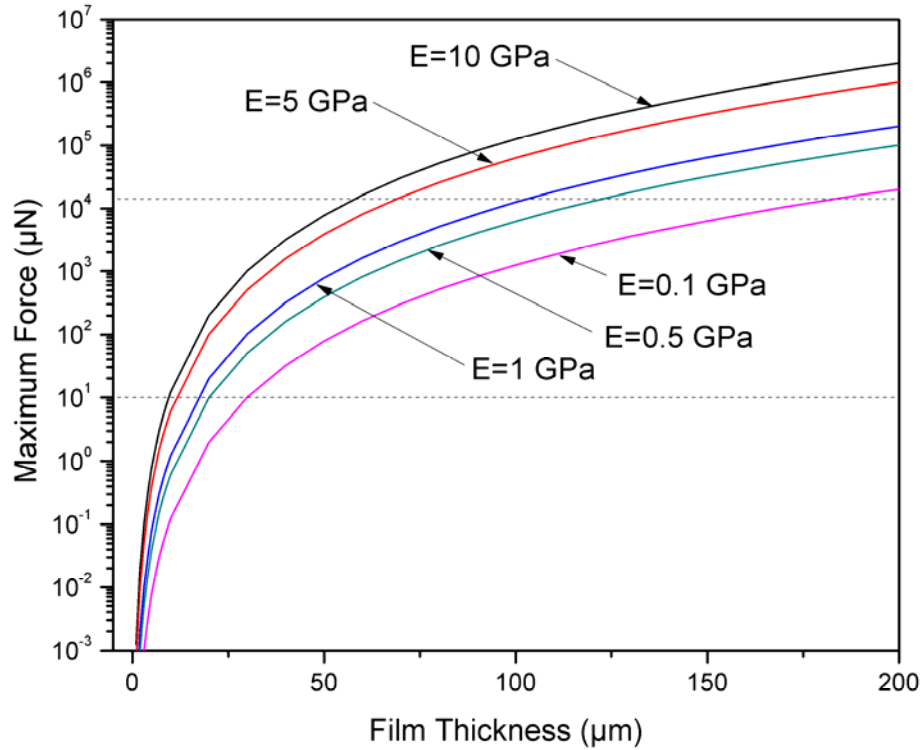


**Figure 3.8:** The maximum possible force that can be applied in the plate deformation regime as a function of film thickness. The Young's modulus corresponding to each curve, and the force range of the Hysitron TriboIndenter, are indicated.

Figure 3.9 shows the ratio of contact indentation to plate deformation ( $\delta_C:\delta_P$ ) on a logarithmic scale as a function of film thickness, under the condition that the maximum permissible force  $P_{\max}$  is applied in the plate deformation regime. The contact indentation is estimated using Hertzian mechanics and the radius of the spherical indenter is assumed to be  $100 \mu\text{m}$ . As long as the film is characterized with the maximum plate-regime force, the displacement ratio is not dependent on the film's Young's modulus (Thick curve). However, since the maximum possible

force in the nanoindenter is limited to a maximum force of 15 mN, it is not possible to reach the maximum plate-regime force with thicker films. As a result, the displacement ratio depends on the film's Young's modulus, and a higher displacement ratio will be obtained. Figure 3.9 also shows the contribution of contact indentation relative to the total deformation as a function of film thickness and Young's modulus when a maximum force of 15 mN is applied to the film.

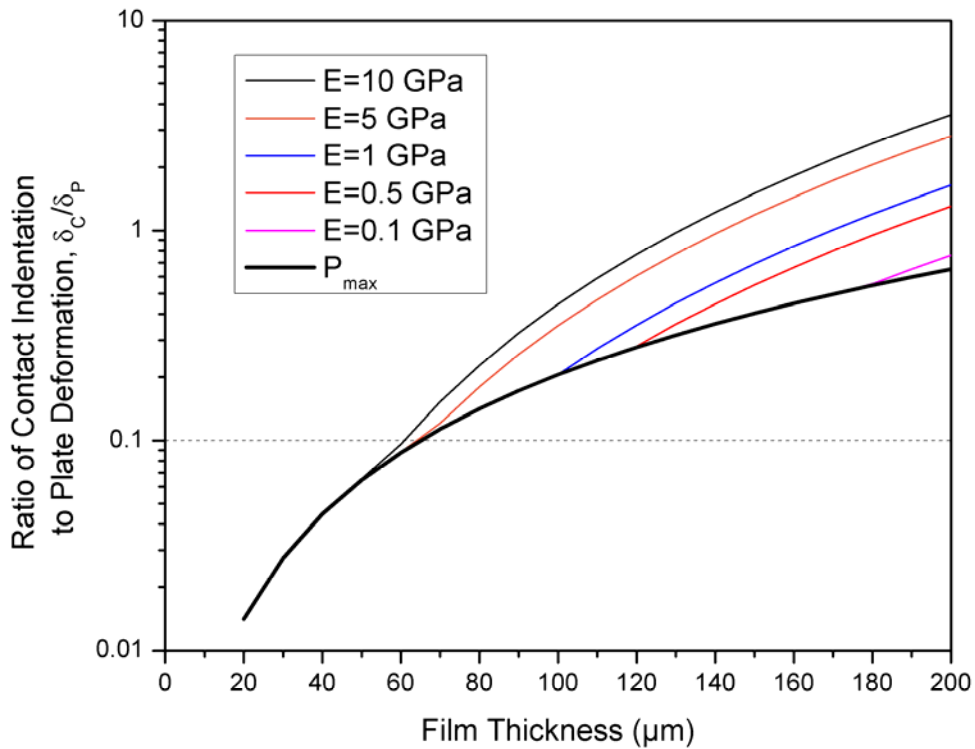


**Figure 3.9:** Contact-to-plate displacement ratio as a function of film thickness for representative polymers. The solid curve shows the ratio for all polymers when the maximum force ( $P_{\text{max}}$ ) is applied. Thin curves show the ratio for  $P=15$  mN (the maximum force of a typical Hysitron indenter).

### 3.4.2 Design of Test Jigs

Figure 3.6 shows the clamping fixture designed for the tests. The thin film is clamped between two steel plates using two driving screws. There are holes with equal radii at the centre of each plate, and guide pins located at two corners of the

fixture guarantee concentricity of the holes (see the Appendix 1 for the blueprint of the fixture with dimensions). The steel plates are flat with an RMS roughness of less than  $1\ \mu\text{m}$ , allowing a uniform clamping condition on the edge of the films. The base of the TriboIndenter tip has a square cross section with a side length of  $1.35\ \text{mm}$ . Therefore, a hole radius of  $1.25\ \text{mm}$  was used for the fixture. This is the minimum possible radius still permitting the base of the nanoindenter tip to pass through the hole without touching the fixture. Considering the geometry of TriboIndenter Transducer (Figure 3.10), the width of the jig should be considerably less than  $2.5\ \text{cm}$  to guarantee no accidental contact with the transducer. The width of the jig is designed  $1.25\ \text{cm}$ . Figure 3.10 shows the position of transducer before the nanoindenter tip enters the jig's hole. The steel fixture is attached to a magnetic stage in the TriboIndenter. The TriboIndenter is equipped with an optical microscope that permits the user to define the location for tip engagement. This location is the center of the clamped film, which appears as the center of a circular hole when viewed through the microscope.

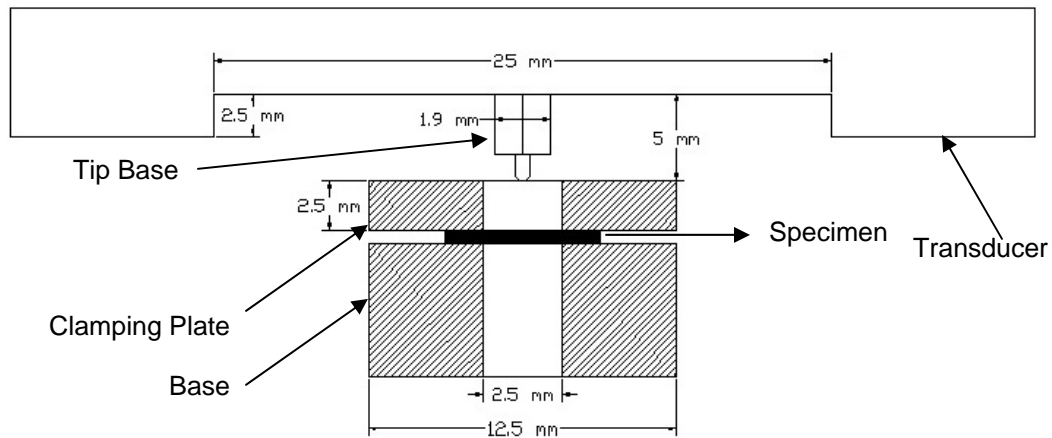


**Figure 3.10: Schematic view and dimensions of the jig and the nanoindenter transducer.**

Finally, various commercial spherical tips with different radii ranging from sub-micrometer to  $100\ \mu\text{m}$  are available. Here, a commercial spherical indenter tip

with a large radius (100  $\mu\text{m}$ ) is used to minimize contact indentation when the bending load is applied.

### 3.4.3 Specimen Preparation

Tests were performed on two standard thin film systems to validate the technique of measuring Young's modulus using the nanoindenter-based test method. The first system is low density polyethylene (LDPE) with thickness ranging from 100 to 130  $\mu\text{m}$ <sup>4</sup>.

The second system is Araldite® MY0510 epoxy obtained from Huntsman. Films of the epoxy were prepared using 4,4-Diaminodiphenyl Sulphone (DDS) as the hardener. Table 3.3 summarizes the basic properties of this resin using information obtained from the data sheet provided by the manufacturer.

**Table 3.3: Typical properties of Araldite MY0510 epoxy systems**

Density	1210-1220 Kg/m <sup>3</sup>
Viscosity @ 25°C	0.55-0.85 Pa.s
Glass transition temperature	270 °C
Flexural modulus	3.4 GPa
Tensile modulus	3.5 GPa
Visual appearance	Clear, no contamination
Storage	Under 5°C

Thin films were synthesized by curing mixtures of epoxy and hardener between two glass plates. Metallic shims with thickness ranging from 25 to 100  $\mu\text{m}$  were used to control the thickness. The details of these protocols are as follows:

1. Mixing of resin and hardener: as recommended by manufacturer, a mixture of five parts by weight of resin was added to three parts by weight of hardener.

---

<sup>4</sup> Provided by Professor Pierre Carreau (Department of Chemical Engineering, École Polytechnique de Montréal)

Mixing was initiated by manually stirring the mixture inside a plastic container using a stirring rod. Subsequently, a high speed electric drill with a spatulate bit was employed to ensure uniform mixing. The mixture was then maintained under low pressures (1 bar) at 50°C for about 30 minutes to remove air bubbles introduced during the mixing process. This step minimizes undesirable porosity in the film.

2. Application of a thin layer of release agent: a release agent is necessary to facilitate removal of the epoxy film from the glass substrate after synthesis. The release agent used was Chemlease 41-90 produced by Chem-Trend. Three coats of the agent were applied for the first use of new glass substrates. For subsequent re-use, the glass substrates were cleaned using a razor blade, and one or two coats of the release agent were applied. The application of release agent was done using paper towel. First, a few drops of release agent were poured on the paper towel. A thin layer of the agent was dispersed on the surface of the glass. Then, another dry towel paper was used to absorb the extra liquid. The cure time between coats was at least 10 minutes and final cure time, prior to sample manufacturing, was at least 30 minutes.
3. Deposition of resin between two glass substrates and a metal shim: Glass stirring rods were used to deposit an appropriate amount of resin at the center of the glass substrates. The amount was calculated based on the inner diameter of the shim (4 cm), the thickness of the shim (25, 50, 75 and 100  $\mu\text{m}$ ) and the density of resin (1210  $\text{Kg/m}^3$ ). As an example, for a 100  $\mu\text{m}$  shim, 0.2 gr. of the resin was used, and the remainder of the resin and hardener was stored inside a refrigerator for future use. Figure 3.11 shows a photograph of a thin film sandwiched between two glass plates. A Sartorius GP5202 Precision Balance with a resolution of 0.01 mg was used for all weight measurements.
4. Curing of resin: curing of epoxy thin films sandwiched between glass substrates was accomplished in a custom-made oven. The oven has a cavity of 50×50×30  $\text{cm}^3$ . The maximum achievable temperature of this oven is 400°F (205°C). The details of the time-temperature steps followed in the cure cycle

- are shown in Figure 3.12. During curing, a force of  $\sim 50$  N was applied on the glass plates to ensure uniformity of the films.
5. Finally, the thin film was removed from the glass substrate using a razor blade and stored for characterization.

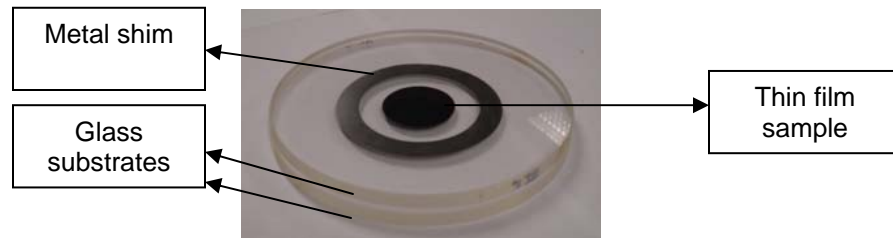


**Figure 3.11: Manufacture of thin films using a steel shim and two glass substrates.**

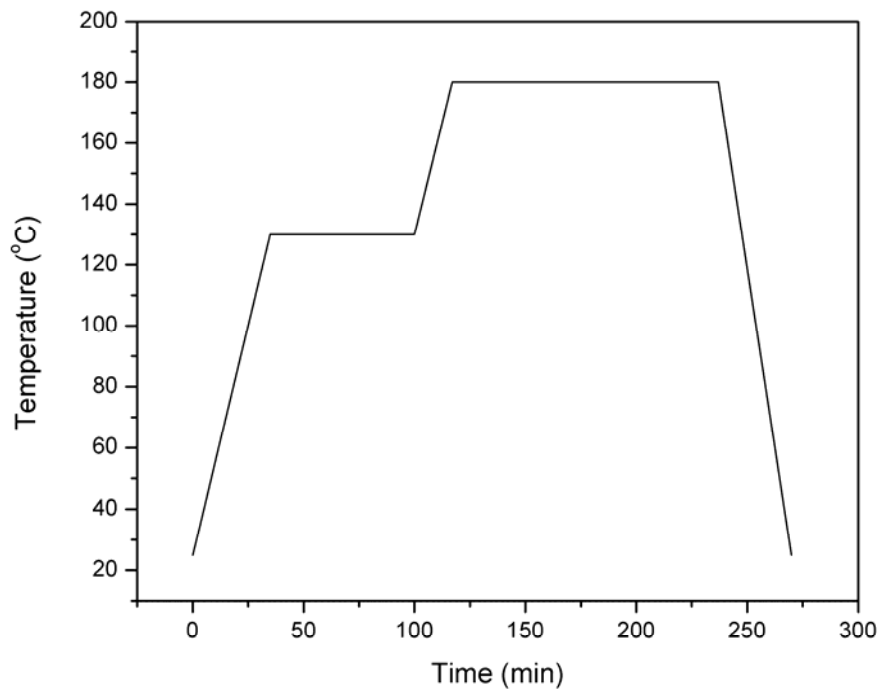


**Figure 3.12: Cure cycle for MY0510 epoxy system (ramp rates:  $3^{\circ}\text{C}/\text{min}$ ).**

### 3.4.4 Protocol for Nanoindenter-Based Tests

To characterize the films, the following procedure was performed:

#### 1. Preparation for testing

First, a piece of the film, approximately  $4\text{mm} \times 4\text{mm}$ , was cut and its thickness was measured with a Mitutoyo micrometer to a precision of  $\pm 1\ \mu\text{m}$ . Then, the film was clamped between the two steel plates in the jig, and the fixture was attached to the magnetic stage of the TriboIndenter. To find the center of the hole, four points on the periphery of the hole (A, C, B and D in Figure 3.13) were located using the optical microscope. The optical microscope has a magnification of  $100\times$ . Figure 3.13-a shows the positions of these four points, and Figure 3.13-b presents a screen-image of the process used to locate one point during a test. The coordinates of these four points were utilized to find the coordinate of the center of the hole to a precision of  $10\ \mu\text{m}$ . The coordinates of each point can be read from the machine with a resolution of  $100\ \text{nm}$  (bottom of Figure 3.13-b). However, since each end point was located by the user, the last two digits of the coordinate were neglected. Therefore, the coordinate of each point was reported with a precision of  $10\ \mu\text{m}$ .

#### 2. Testing

The viscoelastic nature of polymeric materials implies that the measurements will be sensitive to loading rate. Therefore, tests were conducted over a range of loading rates from  $20\ \mu\text{N}/\text{sec}$  to  $10\ \text{mN}/\text{sec}$ . For each loading rate, a sequential set of bending and conventional nanoindentation tests were performed in a single session. The latter tests were performed on a film of the same material that was glued to a steel substrate, and ten indents were performed with  $100\ \mu\text{m}$  spacing between indents. Finally, another bending test was performed on the clamped film to complete the sequence. The TriboIndenter is susceptible to thermal drift during prolonged testing periods [7]. Hence, tests were considered for further analysis only if the first and second bending tests differed by less than 5% in load and displacement. For each material, this sequence of tests was performed on five

different specimens. The TriboIndenter is equipped with an acoustic/thermal enclosure guaranteeing the temperature uniformity during tests (Please refer to Appendix 3 for more information).

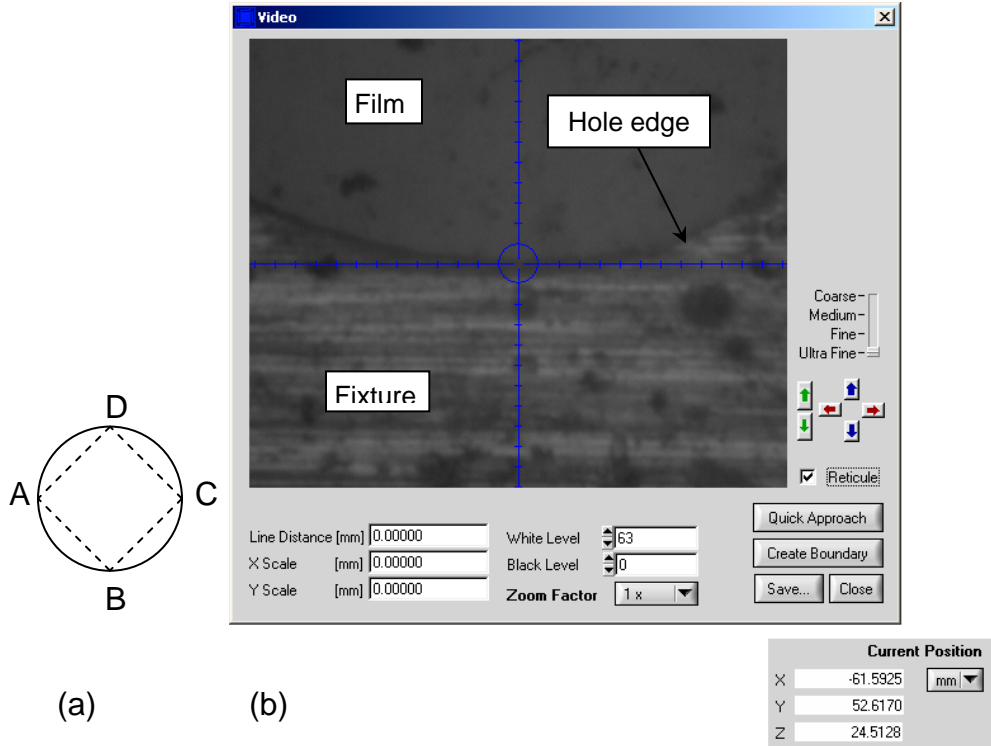


**Figure 3.13: a) Using optical microscope to define the sample (points A, B, C, and D). b) A snapshot of the Triboindenter software when the optic was focused at point B.**

### 3. Post-testing verification of clamping

The film was examined under an optical microscope after testing to confirm the quality of clamping. A continuous circular imprint corresponding to the circular edge of the fixture was interpreted as an indication of clamping. If an imprint was not observed, then the test was not considered for further analysis, and the test procedure was repeated. Finally, the thickness of the film was measured again to confirm that no changes had occurred during the test.

### 4. Conventional nanoindentation using a Berkovich Tip

In order to compare results from the bending tests with conventional nanoindentation, a series of tests were performed using a Berkovich tip in the

TriboIndenter. The Berkovich tip is a three-sided pyramid tip with a half angle of 65.35 degrees and the most commonly used for nanoindentation. The area of the diamond tip was calibrated using a quartz standard.

The polymer thin films were attached to steel substrates using superglue (Instant Krazy Glue®) as recommended by Hysitron. A maximum load of 2 mN, and a dwell time of 30 s at the peak load, was used to reduce viscoelastic effects [30]. The film thickness exceeded 100  $\mu\text{m}$  in all cases, and the maximum indentation was less than 1  $\mu\text{m}$ . The method of Oliver and Pharr [82] was used to calculate Young's moduli from the indentation load-displacement curves. For each loading rate, 20 tests were performed on each sample.

#### 5. Tensile tests:

A set of tensile tests was performed on the LDPE samples using Dynamic Mechanical Analyzer (DMA) with a Q800 instrument. Tests were done by the force control module with three different rates: 0.1 N/min, 1 N/min and 10 N/min. LDPE films have a thickness of 100 to 130  $\mu\text{m}$ . Based on the recommendation of the machine manual, a width of 4.8-5.2 mm and a length of 2.0-2.5 cm were chosen for the rectangular specimens. A total number of 5 tests were performed for each load rate and the average result was reported as the Young's modulus of LDPE. No tensile tests were performed on the epoxy samples as this resin was extremely brittle and cutting crack-free rectangular films suitable for tensile tests was impossible.

#### 6. Roughness measurement:

The scanning probe microscope (SPM) capability of the TriboIndenter was used to obtain the roughness of both LDPE and epoxy systems. Here, a nanoindenter tip was moved in a raster scanning of a 50  $\mu\text{m}$   $\times$  50  $\mu\text{m}$  square using a three-axis piezo positioner. TriboView, the complementary commercial software of Hysitron Triboindenter, was used for image analysis to extract the roughness and maximum asperity height of the surface.

### 3.5 Results

First, results related to the characterization of epoxy films will be presented. For all calculations a Poisson's ratio of 0.4 is assumed. Figure 3.14 shows three different deflection curves as functions of loads. The first curve ( $\delta_T$ ) is the total displacement of a 100  $\mu\text{m}$ -thick circular plate when loaded at its center with a maximum load of 1 mN. The second curve ( $\delta_C$ ) is obtained through nanoindentations on the epoxy film attached to a substrate. By subtracting the second curve from the first curve (Equation (3.1)), it is possible to obtain the pure bending behaviour of the plate ( $\delta_P$ ). For all three curves, the loading rate is 300  $\mu\text{N}/\text{sec}$ . As expected from Equation (3.2), this curve should be linear. A linear curve fitting results in a correlation coefficient ( $R^2$ ) of 0.997. The slope of this curve is used to extract the Young's modulus of the epoxy film based on Equation (3.2). Error bars of  $\delta_T$  correspond to standard deviations from five different tests, while those of  $\delta_C$  are from ten tests. As can be seen from this figure, bending tests result in smaller error bars as compared to nanoindentation tests [107].

Table 3.4 gives the Young's modulus for three different rates (50  $\mu\text{N}/\text{sec}$ , 300  $\mu\text{N}/\text{sec}$ , and 2500  $\mu\text{N}/\text{sec}$ ). The load rate has only a small effect on the Young's modulus of epoxy films. This is expected as this epoxy is designed to be very brittle at room temperature. The modulus of elasticity in bending presented in this table should be compared to the flexural modulus of 3.4 GPa reported by the MY 0510 epoxy manufacturer (Huntsman Company) based on ASTM D790 standard. This standard recommends that a displacement rate of 3.5 micron/sec be used in bending tests, which is equivalent to a loading rate of 2.5 mN/sec (last row in Table 3.4).

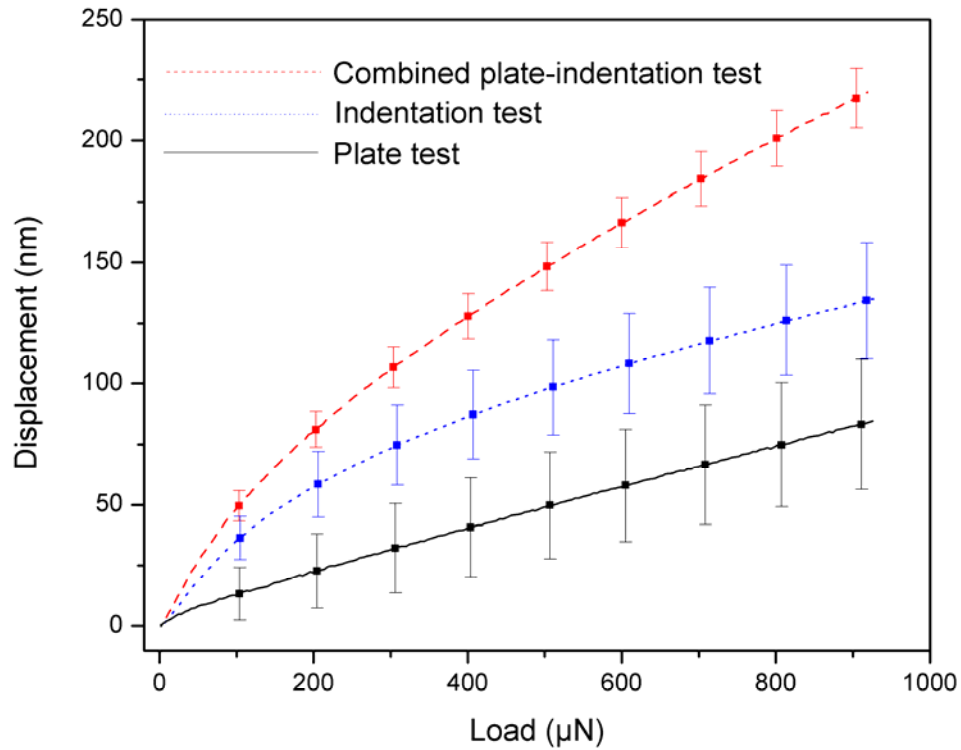


Figure 3.14: Load versus displacement for an epoxy film characterized with a load and load rate of 1 mN and 300  $\mu\text{N}/\text{sec}$ . Pink curve shows the combined plate-indentation behaviour, blue curve shows the nanoindentation behaviour and the black curve is the subtraction of the former curve from the latter one, representing pure plate behaviour.

Table 3.4: Young's modulus of epoxy films obtained through different methods for three different load rates

Load rate ( $\mu\text{N}/\text{sec}$ )	Combined plate and indentation test <sup>†</sup>	Hertzian-corrected bending test <sup>‡</sup>	Hertzian theory	Nanoindentation (Oliver-Pharr)
50	$3.5 \pm 0.5$	$1.7 \pm 0.3$	$0.9 \pm 0.4$	$6.0 \pm 0.2$
300	$3.6 \pm 0.5$	$2.0 \pm 0.2$	$1.0 \pm 0.3$	$5.8 \pm 0.1$
2500	$3.6 \pm 0.5$	$2.2 \pm 0.2$	$1.2 \pm 0.4$	$5.8 \pm 0.1$

<sup>†</sup>Equation (3.7)

<sup>‡</sup>Equation (3.6)

Figure 3.15 compares the results for films with three different thicknesses when the two methods mentioned ahead were used to compensate for contact indentation. For both cases the loading rate is 300  $\mu\text{N}/\text{sec}$ . In the first method, the combined plate-indentation tests were used (Equation (3.7)). In the second method, the Hertzian theory was used to estimate for  $\delta_c$  and Equation (3.6) was used to obtain the Young's modulus directly from the force and the total deflection of the film (Hertzian corrected bending test). It is clear from this figure that the Hertzian-corrected bending test results in a major reduction in properties as thickness increases. On the right side of this graph, the ratio of  $\delta_c:\delta_p$  is given. It is clear from this figure that as the contribution of contact indentation increases, the second method results in a significant underestimation of the predicted modulus. This fact can be explained by observing Figure 3.16. In this figure, the results from the spherical nanoindentation of epoxy films are fitted with the Hertzian theory to extract Young's moduli. The results for three different loading rates are also given in Table 3.4. The results obtained through this technique are almost one third of the expected Young's modulus.

Figure 3.17 shows the results for the LDPE samples. For all calculations a Poisson's ratio of 0.45 is used. The results are the averages from five different films. Young's moduli vary from 120 MPa to 220 MPa as the loading rate increases over almost three orders of magnitude (20  $\mu\text{N}/\text{sec}$  - 10  $\text{mN}/\text{sec}$ ). The change in Young's moduli is almost linear against the logarithm of the load rate (a 31% increase for one order of magnitude rise in the load rate). It is again clear that results obtained through the combined plate-indentation tests are higher than those calculated through the Hertzian-corrected bending tests. This effect is more pronounced for higher load rates. Results of DMA tensile tests are also shown in this figure in which a 24% increase in Young's modulus is observed for an increase of one order of magnitude in load rate. This increase of LDPE Young's modulus is comparable to the results reported by other researchers. As an example, using a tensile test, Drozdov and Yuan [108] showed a linear increase of a 25% on LDPE Young's modulus for an order of magnitude increase in strain

rate. It is worth noting that a direct comparison between our proposed technique and tensile tests is not possible because in the case of tensile tests, all points of the sample experience the same load rates while in the case of bending tests of circular plates, load rates change through both the thickness and radial direction of the plate. Figure 3.17 also shows the Young's modulus obtained by nanoindentation (Oliver-Pharr and Hertz). As with the bending results, Young's modulus is seen to increase almost linearly with the logarithm of the loading rate. However, Young's modulus is exaggerated for Oliver-Pharr approximation and underestimated for Hertzian approximation, similar to the case of epoxy systems.

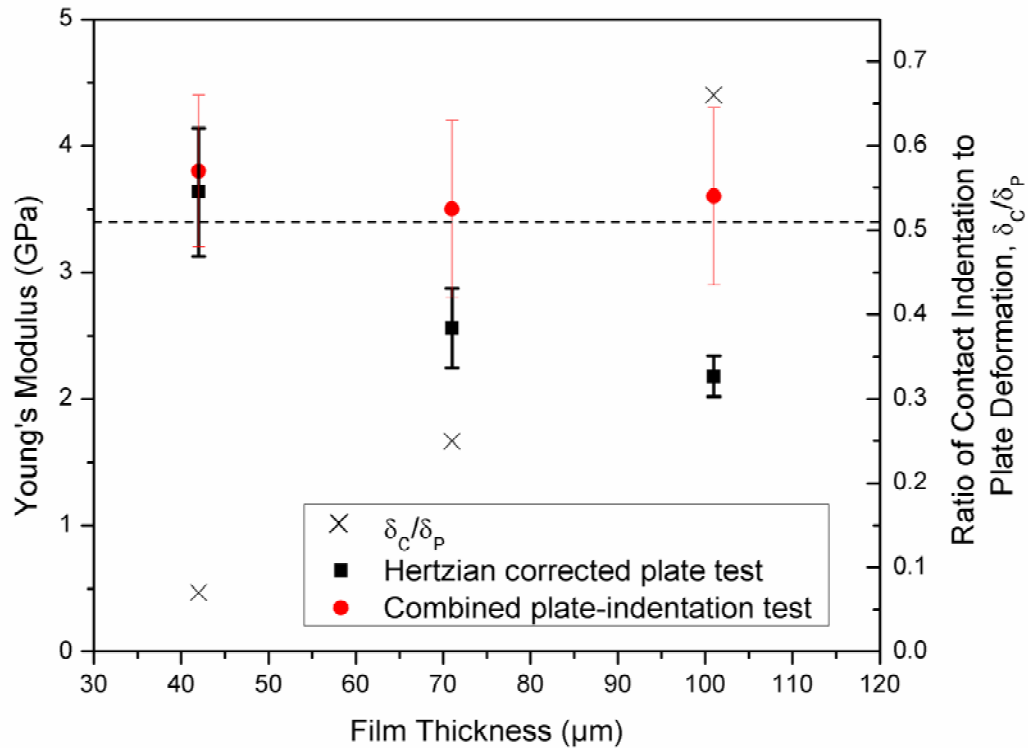
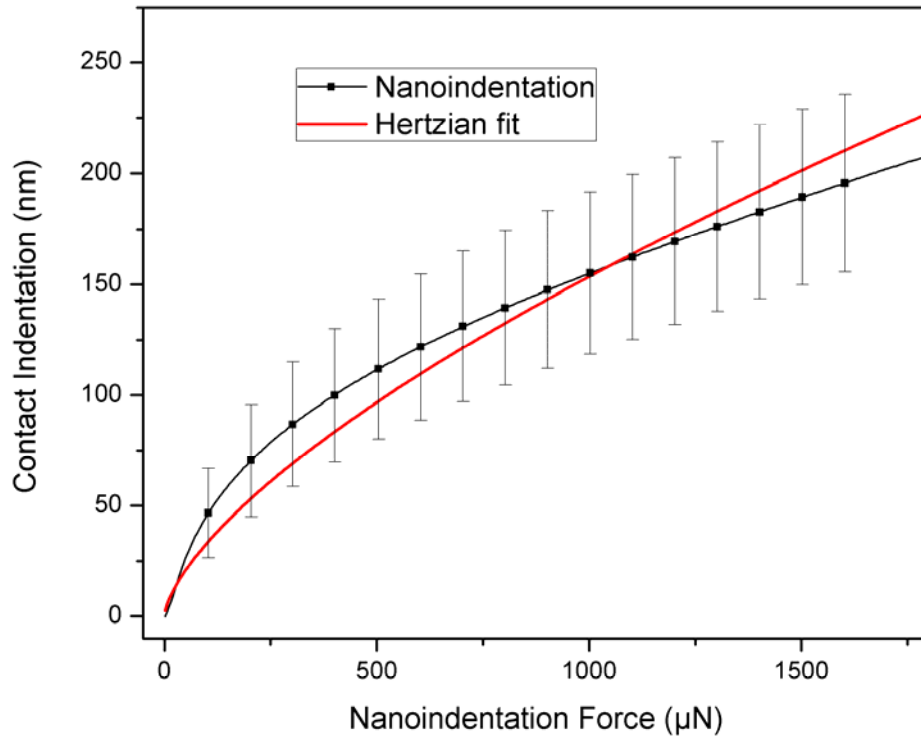


Figure 3.15: Young's modulus as a function of the thickness of epoxy films measured through two techniques, the "Hertzian corrected plate tests" and the "Combined plate-indentation tests". Contact-to-plate displacement ratios are shown for each thickness.



**Figure 3.16:** Load-displacement curve of the epoxy film attached to a steel substrate (load rate of  $300 \mu\text{N}/\text{sec}$ ). Hertz equation was fitted to the curve to extract the epoxy's Young's modulus.

### **3.6 Summary and Discussion**

In this chapter, a novel technique was developed for the elastic characterization of soft thin films based on their bending behaviour by using a nanoindenter. A combination of theoretical and numerical techniques was used to develop this method. A modest variation of less than 11% was predicted between theories and finite element modelling. This error was a weak function of the film thickness but did not depend on the film's Young's modulus. This fact was consistent with the result presented in Figure 3.9. In this figure, ratios of contact indentation to plate deformation were not dependent on the film's Young's modulus as long as maximum possible forces within the range of the plate behaviour were applied to

the film. Moreover, the effect of contact indentation at the place of loading was experimentally evaluated. This resulted in more accurate measurements of the polymers' Young's moduli. The radius of the fixture's hole was designed so that the tip base could pass through the hole. This sets a limitation on the minimum film thicknesses possible to be characterized with this technique. Therefore, there is a possibility of designing a special tip-base in order to characterize thinner films by decreasing the radii of the fixture's holes.

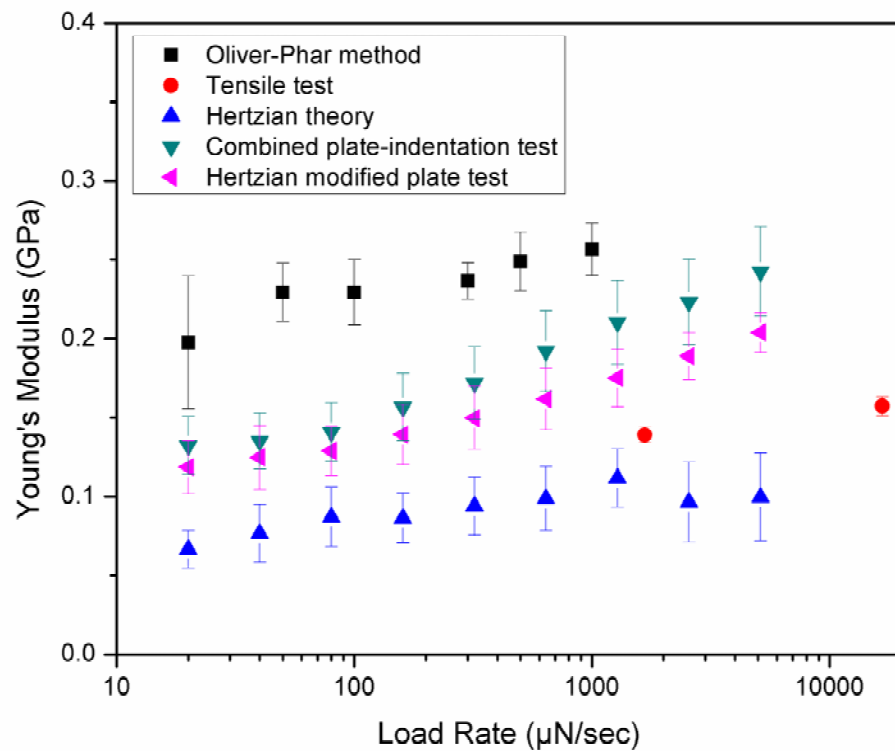


**Figure 3.17: Young's modulus of LDPE as a function of load rates. The results are compared with those obtained through nanoindentation.**

It was also shown that the resulting Young's moduli of both polymer films obtained through bending tests were more accurate than those acquired through nanoindentation tests (Hertz and Oliver-Pharr). This is due to the fact that

nanoindentation techniques, including the Oliver-Pharr method, typically overestimate the Young's moduli [83, 84]. In the case of Hertzian theory, one primary reason resulting in an underestimation of Young's modulus for both epoxy and LDPE systems is the effect of the surface roughness of samples. This has been proved by both experiments [102] and simulations [104]. This is due to the fact that with the application of the same pressures, smooth surfaces deform less than rough surfaces. Gerberich *et al.* [102] have shown that when  $\Delta^{\max}:2\delta_c > 0.05$ , surface roughness plays a role on the modulus measurements. Here,  $\Delta^{\max}$  is the maximum asperity height of the surface. As a result, the effect of surface roughness is more evident for tips with larger radii, as in the present study, since indents will be shallower. In the case of epoxy samples, this ratio was around 0.43 ( $\Delta^{\max} \approx 170$  nm). In the case of LDPE samples, this ratio is around 0.31 ( $\Delta^{\max} \approx 500$  nm). Therefore, the effect of surface roughness is important in both cases. This surface effect, however, does not have a significant effect on the sample characterized by the combined plate-indentation method because the effect of roughness appears in both the plate test and nanoindentation. As a result, the effect is cancelled out when pure bending deflection is calculated. Also, tip imperfection resulting to a decrease in the real radius of the tip might be another reason responsible for the underestimation of the Young's moduli of polymer films from the Hertzian method. This effect is also cancelled out when the combined plate-indentation test is used.

In general, the nanoindenter-based bending technique presented in this chapter has the following advantages:

- The test setup was very simple
- Appropriate application of boundary conditions to films curtails related problematic issues typical of tensile tests.
- Accurate measurement of both force and displacement were achieved through the nanoindenter, thereby overcoming an issue plaguing the bulge testing of polymer thin films.

- Calculation of Young's modulus based on combined plate-indentation was straightforward when compared to nanoindentation tests in which no further elaborations for the area measurement and the contact stiffness of the tip were needed.
- For brittle polymers, similar to the epoxy system used in this work, cutting rectangular pieces for tensile tests is extremely difficult, resulting in micro-cracks at the edges of the sample. However, this is not an issue for bending tests.

Moreover, this technique can be easily utilized for elastic characterization of thin polymer-based composite films (Chapters 4 and 5). The technique presented here can immediately be used for characterizing randomly dispersed nanocomposite films, suitable for structural elements of microactuators. In the case of anisotropic composites, such as aligned or partially aligned nanocomposite films, the theoretical formulation should be revised in order to include effects of anisotropy. Finally, a strong dependency of our proposed method on film thickness is a primary issue since it requires accurate measurement of the film thickness. Since the micrometer used to measure film thicknesses was only precise to 1  $\mu\text{m}$ , only films with thicknesses of 40  $\mu\text{m}$  or more were characterized. In order to characterize thinner films, other methods of thickness measurement are needed to preserve the technique accuracy.

## Chapter 4

# Elastic Characterization of Dilute SWNT-Reinforced Polymer Thin Films

### **4.1 Introduction**

Carbon nanotube-reinforced polymer thin films are being investigated for applications in micromechanical resonators and actuators [109, 110], damping layers [111], and wear resistant films [112]. An accurate characterization of the mechanical properties of nanocomposite thin films is necessary in order to evaluate their suitability for these different applications.

In Chapter 3, a new technique, a nanoindenter-based bending test, was introduced for the elastic characterization of polymer thin films. In this chapter, this technique will be used to measure the elastic properties of epoxy-matrix and vinyl ester epoxy-matrix nanocomposites films (ranging from 50 to 70  $\mu\text{m}$  in thickness) reinforced with low contents of single-walled carbon nanotubes ( $\leq 1$  wt %). At these concentrations, the interactions between reinforcing agents can be safely neglected; as a result, such composites are called dilute nanocomposites. The sections of this chapter are organized as follows. Section 4.2 describes the procedures used for the synthesis of polymer nanocomposite thin films. Section 4.3 explains the experimental procedure for the elastic characterization of these films using two different techniques (nanoindenter-based bending tests and dynamics mechanical analysis). Finally, results on the elastic characterization of these films are presented in Section 4.4.

### **4.2 Synthesis of Polymer Nanocomposite Thin Films**

The nanotubes used in this work were single-walled carbon nanotubes (SWNT) supplied by the Steacie Institute for Molecular Sciences of the National Research

Council of Canada (SIMS-NRC) in Ottawa, ON, Canada. Two different classes of nanocomposite films were manufactured, as described below.

#### 4.2.1 SWNT-Reinforced Epoxy Thin Films

The nanotubes were synthesized using a laser-oven technique (Laser) and plasma process (Plasma) that is proprietary to SIMS-NRC. Carboxylic acid functional groups, which are assumed to aid in the de-bundling and dispersion of nanotubes, were applied at the level of ~4 wt%. The nanotube/epoxy mixture was prepared at SIMS-NRC by mixing SWNT in the MY0510 epoxy. To decrease the viscosity of the resin, and to enable better dispersion of the functionalized SWNTs, the resins were first dissolved in Tetrahydrofuran (THF) solvent and then the nanotubes were dispersed in the mixture. The THF was removed by placing the THF/SWNT/MY0510 at low pressure at 80°C for about 2.5 hrs until all the solvent had evaporated (Boiling point of THF is 66 °C). As recommended by the resin manufacturer, a mixture of 5 parts by weight of resin was added to 3 parts by weight of hardener. The mixture was then maintained under low pressures (1 bar) at 50°C for about 30 minutes to remove air bubbles introduced during the mixing process. This step minimizes the level of undesirable porosity in the film. The same heating cycle and thin-film manufacturing technique described in Section 3.4.3 for MY 0510 epoxy were used to manufacture nanocomposite thin films with thicknesses ranging from 50 µm to 70 µm (4 to 5 films per sample). Table 4.1 lists the specifications of different epoxy nanocomposite thin films.

**Table 4.1: Specifications of SWNT-reinforced epoxy films**

<b>Sample Name</b>	<b>Weight Fraction (%)</b>	<b>Nanotube Type</b>
<b>Polymer film</b>	-	-
<b>Plasma 1</b>	0.125	Plasma
<b>Plasma 2</b>	0.25	Plasma
<b>Plasma 3</b>	1	Plasma
<b>Laser 1</b>	0.125	Laser
<b>Laser 2</b>	0.25	Laser

### **4.2.2 SWNT-Reinforced Epoxy Vinyl Ester Thin Films**

The epoxy vinyl ester used was Derakane Momentum 411-350, supplied by Ashland Inc. The nanotube/epoxy mixture was prepared at SIMS-NRC by mixing 0.6 wt% of carboxylic acid functionalized SWNT in the epoxy vinyl ester. The copolymerization reaction was initiated via the addition of a catalyst (Trigonox 239 A, an organic peroxide type F, produced by Akzo Nobel) and promoted by using NL-49P Cobalt (II) 2-ethylhexanoate, 1 wt% Co, in aliphatic ester (Akzo Nobel). Specimens with lower concentrations of SWNT (0.1, 0.2, 0.3, and 0.4 wt %) were also produced by the dilution of the as-received mixture. To dilute the mixture, an appropriate ratio of epoxy vinyl ester resin and SWNT-modified resin was added to a small plastic container. The two systems were carefully mixed by hand using a stirring rod for about 5 minutes. Thin films with thicknesses ranging from 50  $\mu\text{m}$  to 120  $\mu\text{m}$  were manufactured using glass substrates and metal shims (Section 3.4.3) and cured at room temperature for at least 24 hours.

## **4.3 Experimental Procedure for Elastic Characterization**

### **4.3.1 Nanoindenter-Based Bending Tests**

Tests were performed based on the protocol for nanoindenter-based bending tests described in Chapter 3 (Section 3.4). Since the nanocomposite films had thicknesses between 50  $\mu\text{m}$  and 70  $\mu\text{m}$ , the ratio of contact indentation to plate deformation remained less than 0.1 (Figure 3.9). As a result, Hertzian contact mechanics was accurate enough to evaluate the contact indentation. Thus, Equation (3.6) was utilized to obtain the Young's modulus. For each specimen, four films were tested at a load rate of 300  $\mu\text{N}/\text{sec}$ .

### **4.3.2 Tensile Dynamic Mechanical Analysis Tests**

A set of tensile tests were performed on the vinyl ester nanocomposite films using the film tension module of a TA Instrument Q800 Dynamic Mechanical Analyzer (DMA). The samples had thicknesses between 100 and 120  $\mu\text{m}$ . Strips of films

with a width of 4.8-5.2 mm and a length of 2.0-2.5 cm were cut using razor blades for the DMA tension tests. These dimensions are within the range recommended by the instrument manufacturer. Five tests were performed for each specimen (0, 0.2, 0.4 and 0.6 wt %). Under a static load of 1 N, an oscillatory displacement with a magnitude of 1  $\mu\text{m}$  and a frequency of 1 Hz was applied to the film. The temperature was changed from room temperature to 110°C at a rate of 3°C/min. As shown in Figure 4.1-a, the cutting of the epoxy vinyl ester specimens resulted in fairly uniform edges with no evidence of crack formations, and hence these samples were appropriate for DMA tests. Since epoxy specimens were extremely brittle, cutting rectangular pieces for DMA tests was extremely difficult, resulting in non-uniformity and micro-crack formations at the edges of the sample. Figure 4.1-b illustrates the non-uniformity of the edges of epoxy-based nanocomposite films and Figure 4.1-c shows the formation of micro-cracks of 1 mm long at the edges of the specimens. Therefore, DMA tests were not performed on these samples.

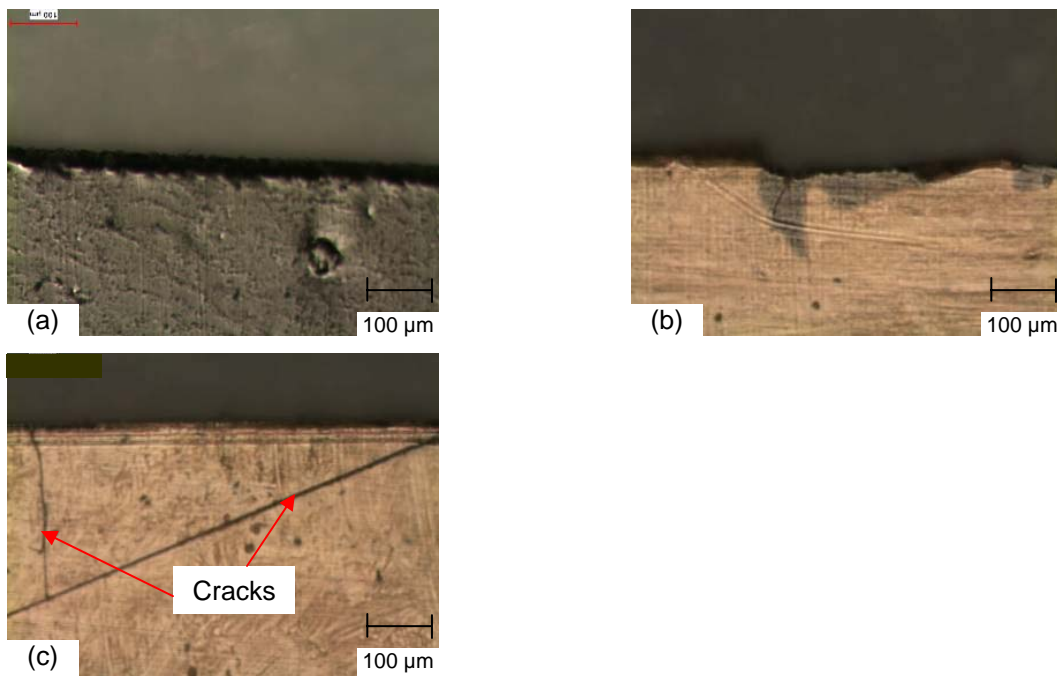


**Figure 4.1: Edges of DMA films a) Epoxy vinyl ester nanocomposite films. b) Epoxy nanocomposite film (Plasma 1) with non-uniform edge. c) Micro-cracks of a few hundreds micrometers on epoxy nanocomposite films.**

## 4.4 Elastic Characterization of SWNT-Reinforced Polymer Thin Films

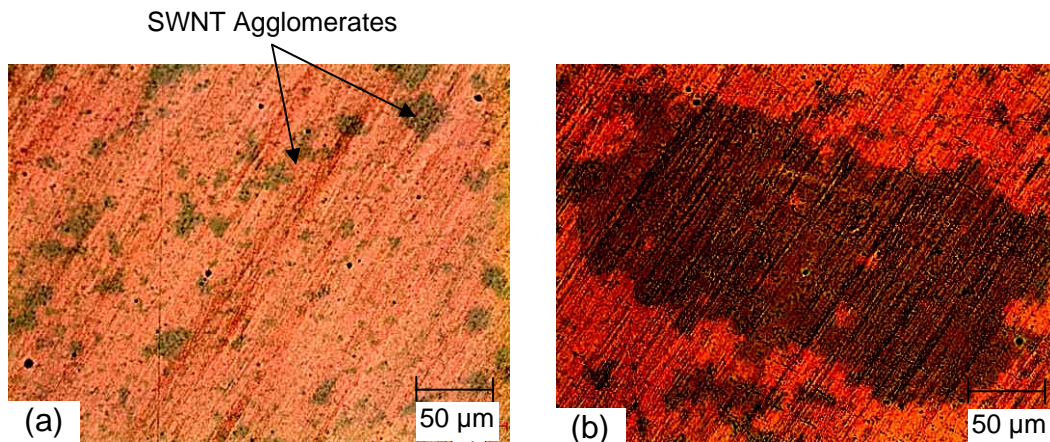
### 4.4.1 SWNT-Reinforced Epoxy Thin Films

Table 4.2 summarizes the Young's modulus of epoxy samples obtained through bending tests. The values reported in the table represent an average over four different films. The last column in the table shows the predicted improvement in elastic properties by applying the Mori-Tanaka method described in Chapter 2. These calculations assume that the reinforcing agents are SWNT arrays with an aspect ratio of 1000. The laser samples did not exhibit any measurable improvement in properties but the Plasma 3 specimen (with 1 wt% of SWNT) showed a maximum increase of 16% in the elastic modulus. This increase can be placed in context by noting that the predictions of the Mori-Tanaka calculation (which assumes good dispersion and perfect bonding between reinforcement and matrix) is 30% for the case of the Plasma 3 specimen.

The optical micrographs in Figure 4.2 provide some insight into the relatively low enhancement of elastic properties in these films. Both micrographs were obtained using the Plasma 1 specimen containing 0.2 wt% of SWNT. Two distinct regions were clearly observed on films: resin-rich regions containing small pockets (5 – 20  $\mu\text{m}$ ) of SWNT (Figure 4.2-a), and large domains with clusters of SWNT ranging from 100 to 500  $\mu\text{m}$  in dimension. As a result, for these specimens, the dispersion of SWNT inside resin is poor, resulting in no major increase in the elastic properties of nanocomposite films.

**Table 4.2: Elastic properties of epoxy polymer and its composites**

Sample name	Weight fraction (%)	Young's modulus (GPa)	Increase/Decrease	
			Experiments	Mori-Tanaka
Polymer film	-	3.6±0.2	-	-
Plasma 1	0.125	3.6±0.2	0%	3.75%
Plasma 2	0.25	3.3±0.3	-8%	7.5%
Plasma 3	1	4.2±0.2	16%	30%
Laser 1	0.125	3.4±0.2	-5%	3.75%
Laser 2	0.25	3.6±0.2	0%	7.5%



**Figure 4.2: Micrographs of the plasma 1 specimen. The dark regions are identified as CNT-rich agglomerates a) resin-rich region with small SNWT agglomeration; b) Agglomerated SWNT region with a size of ~300  $\mu\text{m}$ .**

#### **4.4.2 SWNT-Reinforced Epoxy Vinyl Ester Thin Films**

Figure 4.3 shows a graph of the storage modulus as a function of temperature for various epoxy vinyl ester specimens obtained through DMA tests. The results are an average over 5 tests. A uniform increase in Young's modulus is measured due to an increase in carbon nanotube wt% at room temperature. At higher temperatures, the addition of carbon nanotubes delays the modulus drop (curves are shifted to the right). This fact demonstrates that carbon nanotubes assist the polymer in preserving the elastic modulus at higher temperatures. For all samples, a relative increase of the storage modulus is observed above 60°C. One possible explanation is that the increase in temperature results in the post-curing of the epoxy vinyl ester, increasing the storage modulus [113].

Figure 4.4-a shows the Young's modulus of epoxy vinyl ester nanocomposite films as a function of SWNT weight fraction obtained through DMA and bending tests. While both techniques predict a similar trend of increase in the Young's modulus of the nanocomposite films, the bending technique predicts a higher

modulus for the nanocomposite films. One possible explanation is the difference between the flexural and tensile moduli of epoxy vinyl ester polymer since the bending test measures the bending modulus but the DMA test determines the tensile modulus. However, when the Young's modulus is normalized with respect to the pure polymer, the results from both techniques are identical, as shown in Figure 4.4-b. This graph also shows the results obtained from the Mori-Tanaka approach for individual SWNT and SWNT arrays (and assuming an aspect ratio of 1000 for both types of reinforcements). The increases in the elastic modulus measured through both techniques are comparable and follow the results predicted for SWNT arrays.

Figure 4.5 shows optical micrographs of the pure polymer film at a magnification of 100 $\times$ , and a nanocomposite (containing 0.6wt% SWNT) at three different magnifications. The parallel lines observed on the pure polymer film (Figure 4.5-a) are scratches transferred from the glass substrate. The inhomogeneous regions observed in the optical micrographs of the nanocomposite (Figure 4.5-b and -c) are interpreted as evidence of agglomerated SWNTs. These agglomerations range in size from 5  $\mu\text{m}$  to 10  $\mu\text{m}$ . Figure 4.5-d shows the evidence of a small resin-rich region with a lateral size of a few tens of micrometers. These observations suggest that the dispersion of the nanotubes in the vinyl ester epoxy is not yet optimal, but also that the SWNT distribution is significantly more homogeneous compared to the case of the MY0510 epoxy system.

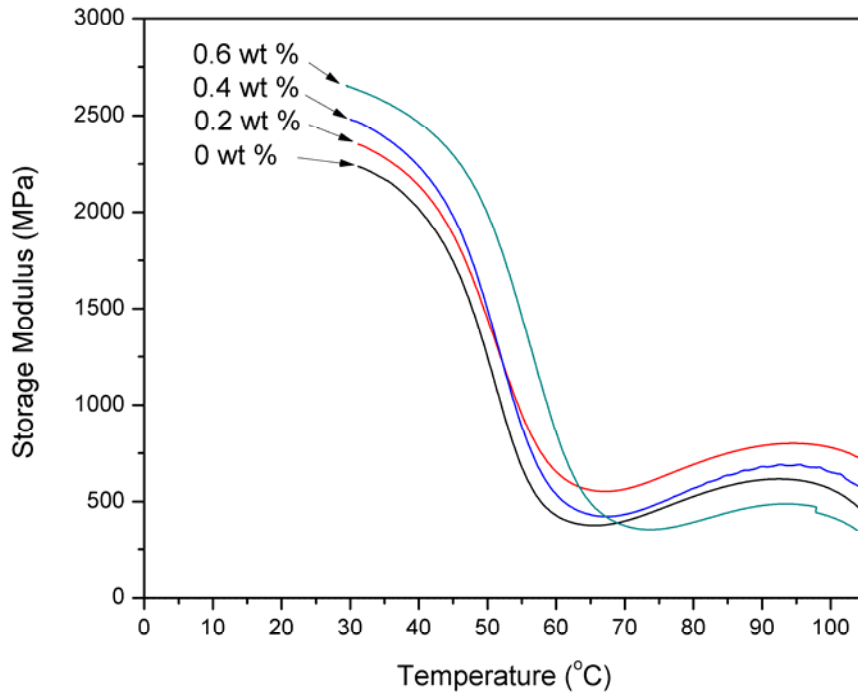


Figure 4.3: Storage modulus of epoxy vinyl ester nanocomposite films obtained through tensile DMA tests.

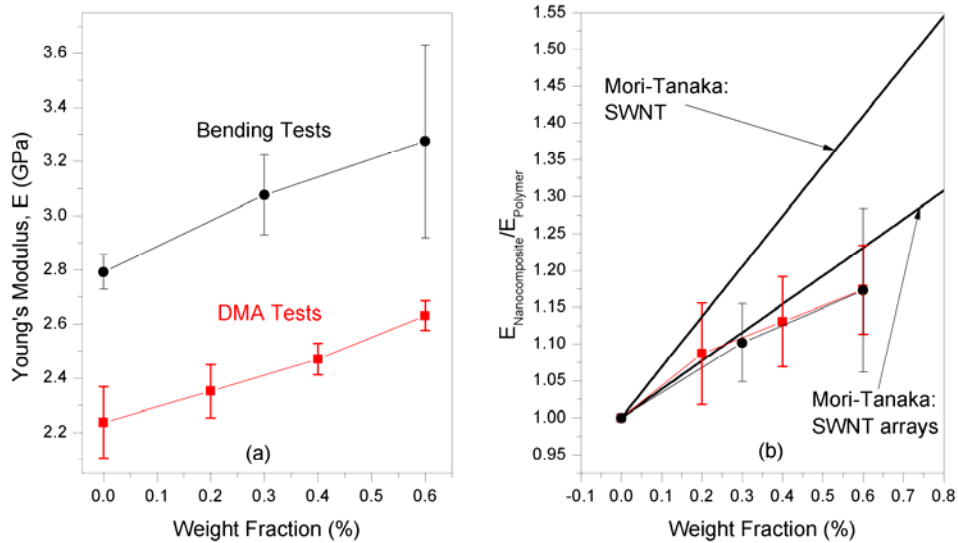
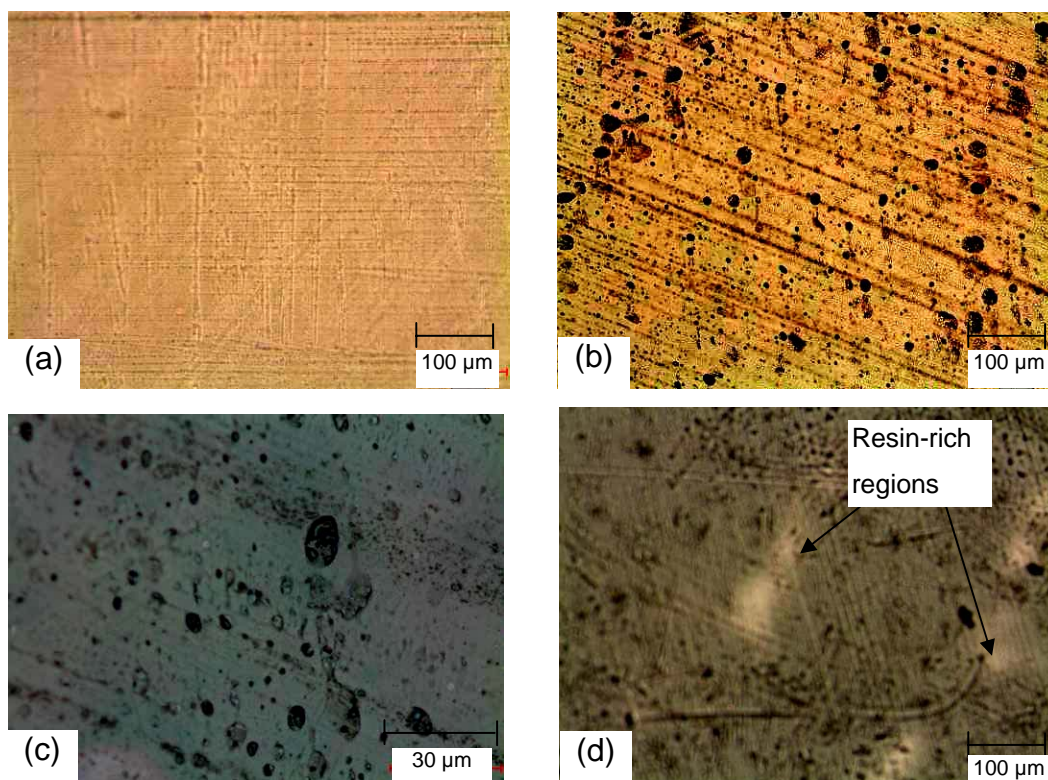


Figure 4.4: a) Young's modulus of SWNT-vinyl ester thin films as a function of SWNT volume fraction predicted through two techniques: DMA and nanoindenter based bending tests. b) Experimental results were compared with theoretical results obtained through Mori-Tanaka approach.



**Figure 4.5: Micrographs of epoxy vinyl ester specimens. a) Pure polymer film ( $\times 100$ ). Lines of scratches can be seen the entire surface transferred from the glass substrates. b) Nanocomposite films with 0.6 wt % SWNT: small agglomerates of a few micrometers are seen. c) Higher magnification ( $\times 500$ ) of nanocomposite films with 0.6 wt % SWNT. The average size of agglomeration is between 5 to 10  $\mu\text{m}$  spread the entire sample. d) Resin-rich region with a size of a few tens of micrometers.**

## 4.5 Conclusions

The results from the characterization of MY0510-epoxy-matrix nanocomposite films show no significant increase in the elastic modulus for nanotube loading of 0.125 wt%. The expected increase, as predicted by the Mori-Tanaka method, ranges from 3.75% to 7.5% for these specimens. Since these increases are comparable to the resolution of the nanoindenter-based bending tests (estimated at 10%), these results indicate that the technique was not sufficiently sensitive to detect any small increase in elastic properties. However, the one specimen with a larger loading (1 wt% SWNT) showed a significant increase of 16% in the elastic modulus. In comparison, the Mori-Tanaka method predicts an increase of 30% for

this specimen. A primary source for the difference between the measured and theoretical results is attributed to poor dispersion of nanotubes in the matrix, as evidenced by agglomerations observed in optical micrographs. In addition, several other factors also deserve investigation in future studies including (i) poor bonding between the epoxy matrix and the reinforcing nanotubes; (ii) the high percentage of impurities in the plasma specimens, which effectively lowers the nanotube loading; and (iii) the high viscosity of the laser specimens, which impedes nanotube dispersion and thin-film manufacturing [5]. These nanotubes have a high aspect ratio ( $>10,000$ ), which is one order of magnitude larger than the optimal value necessary to achieve good mechanical reinforcement with minimal increase of viscosity.

In contrast, the results from the characterization of the epoxy vinyl ester-based nanocomposite showed an increase of mechanical properties that is consistent with the predictions of Mori-Tanaka theory for randomly-oriented SWNT arrays. Furthermore, two different test methods (nanoindenter-based bending and DMA) resulted in comparable values for the normalized increase in the elastic modulus (using the value for the pure polymer as the base-line). These results suggest that: (i) there is significantly better bonding between the nanotubes and the epoxy vinyl ester than between the nanotubes and MY0510 epoxy, and (ii) that the nanotubes are more homogeneously distributed in the vinyl ester, which is also supported by optical microscopic observations.

## Chapter 5

# Elastic Characterization of Polymer-Impregnated Buckypaper Thin Films

### 5.1 Introduction

Porous carbon nanotube sheets, also known as buckypaper, are typically formed by vacuum infiltration of a suspended solution of carbon nanotubes. Buckypaper is appropriate for a wide range of applications including electrodes [114], gas separators [115], field emitters [116], actuators [117], and structural reinforcement [74, 118-122]. Depending on its application, the mechanical properties of buckypaper can directly or indirectly influence its functionality.

A few researchers have theoretically and experimentally characterized the elastic properties of pristine buckypaper. Zhang *et al.* [123] performed tensile tests to measure a Young's modulus of 0.8 GPa for this material. Through nitric acid oxidation, they were able to increase the Young's modulus of buckypaper to 5 GPa. Whitten *et al.* [114] characterized the effects of both humidity and an ionic liquid on the mechanical properties of buckypaper, both reducing the Young's modulus of buckypaper from 2.3 GPa to 1.32 GPa and 0.28 GPa, respectively. Berhan *et al.* [124] measured a range of Young's modulus for buckypaper manufactured using two types of carbon nanotubes (Hipco, High pressure CO conversion, and Laser ablation), and investigated the effects of annealing on the elastic properties. A theoretical model was also presented to predict the upper-bound moduli of buckypaper containing nanotube ropes with an emphasis on the effect of joint morphology. The Young's modulus of a sheet ranging from 1% to 10% of the rope's Young's modulus was predicted. This suggested the possibility of 2- to 15-fold increases in the Young's modulus of buckypaper compared to the state-of-the-art experimental data if the area (volume) fraction and the connection numbers between nanotube ropes were increased. In another theoretical

investigation [125], the classical Cox model [126] was utilized to obtain the mechanical properties of buckypaper, and to determine the effects of the rope properties (diameter, length, and Young's modulus) and sheet porosity on the Young's modulus of the buckypaper. For typical values of these parameters, Young's moduli ranging from 0.9 to 1.4 GPa were predicted.

Several researchers have tried to manufacture composites using buckypaper. Wang *et al.* [74] used a thickness-through infiltration technique to impregnate buckypaper with an acetone-diluted epoxy resin. Using a hot press, they transformed a few superimposed impregnated buckypaper sheets into a uniform film. The impregnated buckypaper films were characterized using the DMA technique resulting in a Young modulus of up to 15 GPa. No correlation between the SWNT volume fraction and Young's modulus was observed. A permeability of around  $2 \times 10^{-19} \text{ m}^2$  was reported for buckypaper sheets. A similar technique was utilized to impregnate buckypaper with diluted polycarbonate (PC) resins [119]. The modulus of the impregnated buckypaper was 6.2 GPa, which is a factor of 3.4 times higher than that of the polycarbonate film.

Coleman *et al.* [120] used the polymer intercalation of organic polymers, poly vinyl alcohol (PVA), poly vinyl pyrrolidone (PVP) and poly styrene (PS), to impregnate buckypaper. The improvement in Young's modulus was measured by DMA techniques and the enhancement of the modulus was reported to be independent of the type of polymer. For a 64-hour soaking time, they reported a modulus of 6.9 GPa for PVA-impregnated buckypaper (which has a three-fold increase with respect to the non-impregnated buckypaper). A similar technique was used for the impregnation of buckypaper to observe the effect of the molecular weight of the polymer on the mechanical properties of the composites [121]. A maximum increase of 3.5 times in Young's modulus was found for the longer chain polymer when compared to the pristine buckypaper. In another work, the impregnation of buckypaper was achieved through the electro-spinning of a

silicone elastomer, resulting in a two-fold increase in the Young's modulus of the composite with respect to the elastomer [122].

Song *et al.* suggested a hot-compress technique to sandwich buckypaper between poly-ether-ether-ketone (PEEK) polymer films [118]. They reported an increase of about 40% in the Young's modulus of the sandwich laminate. By using rule-of-mixtures, they calculated a Young's modulus of 8 GPa for the polymer-impregnated buckypaper layer of the sandwich, which is 2.9 times that of pure PEEK.

Table 5.1 summarizes the experimental results found in the literature for the elastic properties of pristine buckypaper. A summary of elastic properties of polymer nanocomposite films manufactured using buckypaper sheets is tabulated in Table 5.2.

**Table 5.1: Elastic properties of pristine buckypaper and resin-impregnated buckypaper**

Reference	$E_{BP}$ (GPa)	Test method
[123]	0.8-5.0	Tensile test using DMA
[114]	0.3-2.2	Tensile test using DMA
[124]	1.1-4	Tensile test using DMA
[117]	1.2	–
[120]	2.3	Tensile test using DMA
[121]	0.9	Tensile test using DMA
<b>This work</b>	<b>0.5</b>	<b>Bending test</b>

**Table 5.2: Elastic properties of resin-impregnated buckypaper sheets**

Ref..	$E_{BP}^\dagger$ (GPa)	Polymer	$E_P^\dagger$ (GPa)	Impregnation method	Test method	$E_C^\dagger$ (GPa)	$E_C/E_{BP}$	$E_C/E_{BP}$
[122]	–	Silicone elastomer	0.20	Spin coating	Tensile test using DMA	0.42		2.1
[120]	2.3	PVA, PS, PVP		Intercalation	Tensile test using DMA	6.9	3	
[121]	0.9	PVP		Intercalation	Tensile test using DMA	3.2	3.5	
[118]	–	PEEK	2.7	Hot compress	Tensile test	8		3
[74]	–	Epoxy	3.5	Resin infiltration	DMA	13.3		3.8
[119]	–	PC	1.8	Resin infiltration	DMA	6.2		3.4
<b>This work</b>	<b>0.5</b>	<b>Epoxy</b>	<b>3.4</b>	<b>Vacuum infiltration</b>	<b>Bending Test</b>	<b>11</b>	<b>22.0</b>	<b>3.1</b>
<b>This work</b>	<b>0.5</b>	<b>Epoxy</b>	<b>3.4</b>	<b>Hot compress</b>	<b>Bending Test</b>	<b>3.5</b>	<b>7.0</b>	<b>1</b>

<sup>†</sup> BP, P, and C stand for buckypaper, polymer and composite, respectively.

The remaining sections of this chapter are organized as follows. Section 5.2 describes the procedure used for manufacturing of the buckypaper by Dr. J. Guan and Dr. B. Simard at SIMS-NRC. Section 5.3 presents results on the characterization of pristine buckypaper. Section 5.4 discusses the theory for a bending deformation of bi-layer circular plates under a point load. This discussion is an extension of the theory for isotropic circular plates developed in Chapter 3 and will later be used for the elastic characterization of resin-impregnated buckypaper sheets. Section 5.5 describes two approaches for the resin impregnation of buckypaper (hot-press and vacuum infiltration). Finally, the results on the qualitative evaluation of impregnation techniques through scanning electron microscopy as well as the results on the elastic properties of impregnated samples are presented in Section 5.6.

## **5.2 Buckypaper Manufacturing**

### **5.2.1 Purification of Raw SWNT Manufactured with Double Laser Ablation System**

The raw SWNT samples were purified with in-house developed procedures called 3×3 WCPP purification [127, 128]<sup>5</sup>. The recovery of purified dry SWNT is 30 to 50% by weight, and the purity is over 90% by weight.

### **5.2.2 Preparation of Suspension of SWNTs**

A dried and purified SWNT sample (800 g) was grounded in a small amount of Tetrahydrofuran (THF) with mortar. The fine paste was transferred into a two-litre beaker with 1.5 litre of ethanol or methanol. The mixture was sonicated with a sonication probe for more than 1 hour until a well dispersed suspension was attained.

### **5.2.3 Preparation of Buckypaper**

The above well-dispersed suspension was filtered through a polycarbonate (PC) membrane with a pore size of 20 µm and a diameter of 47 mm with the low vacuum of a water-pump. As soon as the solvent was drained away, the water pump was stopped immediately. The wet buckypaper together with the membrane was placed in between two isolation papers and then inserted between two metal cylinders with flat surfaces. In addition, on both sides of each buckypaper sandwich, one or two filter papers were added in order to create more space for pressing. The metal cylinders were then mounted on the press and kept under the pressure of 10 MPa overnight.

### **5.2.4 Post-Treatment of Buckypaper**

After pressing, the PC membrane was carefully removed. Care should be taken to avoid any damage to the buckypaper sheets. At this stage, the buckypaper was

---

<sup>5</sup> A purification technique developed by Dr. Jingwen Guan and Dr. Benoit Simard in SIMS-NRC

almost 80% dry. Finally, the pristine buckypaper was put back into the isolation paper sandwich in a Petri dish and dried in an oven at 85°C overnight.

### 5.3 Characterization of Pristine Buckypaper

#### 5.3.1 Characterization Using Scanning Electron Microscope

A Hitachi S-4700 Field Emission Scanning Electron Microscope (SEM) was utilized to characterize the pristine buckypaper. Field Emission SEMs provides high resolution at relatively high magnification. Figure 5.1 shows images of pristine buckypaper taken by a scanning electron microscope with magnifications of 10K, 25K, 100K and 200 K. Based on these images, the SWNT ropes in the buckypaper have diameters ranging from 10 nm to 50 nm. This is consistent with the fact that buckypaper is made of ropes or arrays rather than individual SWNTs. These SEM images clearly show the presence of impurities inside the buckypaper.

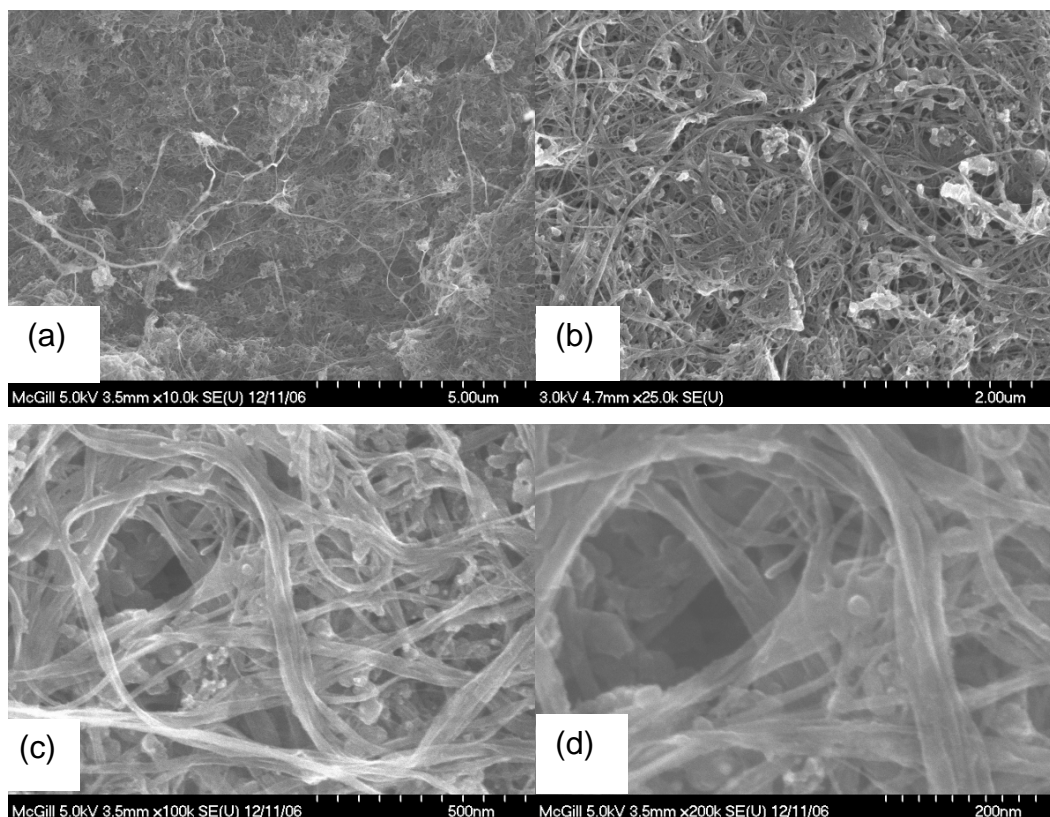


**Figure 5.1: SEM images of pure buckypaper with 10K, 25K, 100K and 200 K magnifications.**

### 5.3.2 Characterization of Impurities

A Thermo Gravimetric Analyzer (TGA-TA instruments Q500) was used to characterize the pristine buckypaper sheets. Two tests were carried out in the nitrogen purge gas from room temperature to 1000°C with a heating rate of 20°C/min. Figure 5.2 presents percentile weight reduction as a function of temperature. A weight residue of between 8% and 10% was observed after reaching 1000°C. These impurities are mainly either metal oxides (around 3%) or quartz glass sand<sup>6</sup>. This percentage represents only a minimum level of impurities that remain following the heating process and greater values of impurities are possible in the buckypaper, considering impurities that burn at temperatures lower than 1000 °C.

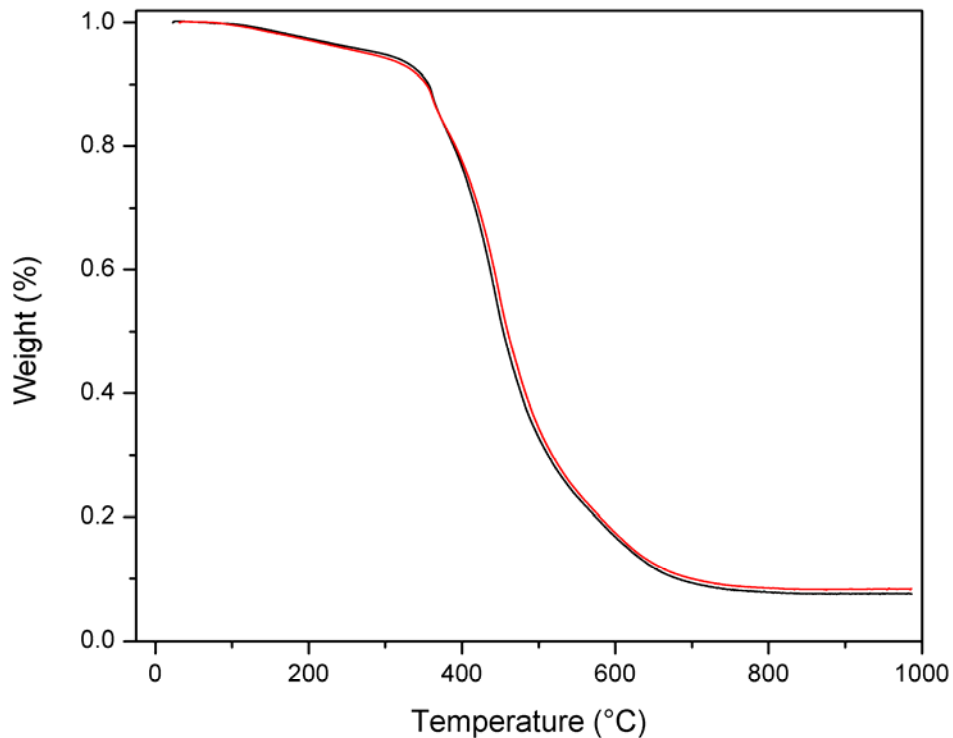


**Figure 5.2: Weight change of two buckypaper sheets under nitrogen purge gas as a function of temperature.**

---

<sup>6</sup> Private communication with Dr. Jingwen at SIMS-NRC.

### 5.3.3 Density Characterization

To find the density, the following procedure was used for each sheet of buckypaper. First, the total weight ( $W_t$ ) of buckypaper was measured using a Sartorius CP225D balance. The diameter of the buckypaper sheet was measured using a calliper to obtain its area ( $A$ ). The thickness ( $h$ ) of the buckypaper was measured with a Mitutoyo micrometer. As a result, the density of buckypaper ( $\rho^{BP}$ ) was obtained through:

$$\rho^{BP} = \frac{W_t}{Ah} \quad (5.1)$$

The density of a carbon nanotube rope (array) depends on its diameter [54]:

$$\rho^{rope} = \frac{V_a N M_w}{\pi N_a R_{SW}^2} \quad (5.2)$$

Here,  $N_a$  is the Avogadro's number,  $N$  is the number of carbon atoms per unit length,  $M_w$  is the carbon atomic weight,  $R_{SW}$  is SWNT radius and  $V_a$  is the SWNT rope packing fraction, which for hexagonal packing is 0.906.

Considering impurities inside the buckypaper sheets with a weight of  $W_i$ , the volume fraction of SWNT arrays or rope is given by:

$$V_f = \frac{W_t - W_i}{Ah} \cdot \frac{1}{\rho_{SWNT-rope}} \quad (5.3)$$

Therefore, by combining Equations (5.2) and (5.3), the volume fraction of SWNT arrays inside the buckypaper was obtained through:

$$V_f = \frac{(W_t - W_i)}{Ah} \cdot \frac{\pi N_a R_{SW}^2}{V_a N M_w} \quad (5.4)$$

Table 5.3 gives the density of buckypaper for four different sheets. Here, an average SWNT diameter of 1.4 nm was used in order to obtain the densities of SWNT arrays. Considering 10% (weight) impurities inside buckypaper, volume fractions of 30 to 40% were calculated for the buckypaper.

**Table 5.3: Density, volume fraction and Young's modulus of buckypaper**

Sample	Density (gr/cm <sup>3</sup> )	Volume fraction (%)	E (GPa)
1	0.46	30	0.58
2	0.48	35	0.74
3	0.49	35	0.40
4	0.55	39	0.30
<b>Average</b>	<b>0.49±0.04</b>	<b>35±4</b>	<b>0.51±0.20</b>

### 5.3.4 Elastic Characterization of Pristine Buckypaper

The nanoindenter-based bending test technique developed in Chapter 3 was used to characterize the elastic properties of pure buckypaper. For all samples, a maximum force of 1 mN was used to measure the deflection of the center of a clamped circular buckypaper plate. Tests with different load rates ranging from 20  $\mu\text{N}/\text{sec}$  to 5000  $\mu\text{N}/\text{sec}$  rates were done on the buckypaper. Table 5.3 lists the Young's modulus of 4 different buckypaper films for a load rate of 300  $\mu\text{N}/\text{sec}$ . From this table, no correlation between the volume fraction and the Young's modulus is evident. Also, the change in the load rate does not result in any significant change of the Young's modulus of the buckypaper, indicating no significant viscoelastic behavior during testing. This is consistent with the results found by Zhang *et al.* [123].

Table 5.4 summarizes the properties of the pristine buckypaper films.

**Table 5.4: Properties of buckypaper**

<b>Thickness</b>	60-100 $\mu\text{m}$
<b>Impurities</b>	>10%
<b>Diameter of SWNT</b>	$\sim 1.3$ nm
<b>Diameter of SWNT rope</b>	10-50 nm
<b>Aspect ratio of SWNT rope</b>	>10000
<b>Density</b>	0.46-0.55 $\text{gr/cm}^3$
<b>Volume fraction</b>	30-39 (%)
<b>Functionalization</b>	Unfunctionalized
<b>Young's modulus</b>	0.50 $\pm$ 0.2

#### **5.4 Bending Deformation of Isotropic Bi-Layer Films**

Based on Timoshenko's plate theory, the deflection ( $\delta_p$ ) of a clamped circular plate under a point load ( $P$ ) is given by [100]:

$$\delta_p = \frac{1}{16\pi} \frac{a^2}{D} P \quad (5.5)$$

Here,  $a$  is the radius of the plate and  $D$  is the bending stiffness of the film. For single-layer, isotropic film the bending stiffness is given by [100]:

$$D = \frac{Eh^3}{12(1-\nu^2)} \quad (5.6)$$

In this equation,  $E$  and  $\nu$  are the Young's modulus and the Poisson's ratio of the film and  $h$  is the film's thickness.

For the case of an orthotropic film, the bending stiffness of the circular plate can be approximated as [129]:

$$D \approx \frac{1}{8}(3D_{11} + 2(D_{12} + D_{66}) + 3D_{22}) \quad (5.7)$$

Here, axes  $1$  and  $2$  are located parallel to the surface of the plate and axis  $6$  is perpendicular to the surface of the plate. For a plate with two or more isotropic layers, Equation (5.7) is simplified as [130]:

$$D \approx D_{11} \quad (5.8)$$

For isotropic bi-layer films  $D_{11}$  is given by [130]:

$$D_{11} = \frac{E_{L1}}{1-\nu_{L1}^2} \left( h_{L1} z_{L1}^2 + \frac{h_{L1}^3}{12} \right) + \frac{E_{L2}}{1-\nu_{L2}^2} \left( h_{L2} z_{L2}^2 + \frac{h_{L2}^3}{12} \right) \quad (5.9)$$

Here, subscripts  $L1$  and  $L2$  refer to the properties of the first and second layers, respectively. Also,  $z_{L1}$  and  $z_{L2}$  are distances of each layer from the neutral axis (N.A.) of the plate (Figure 5.3).

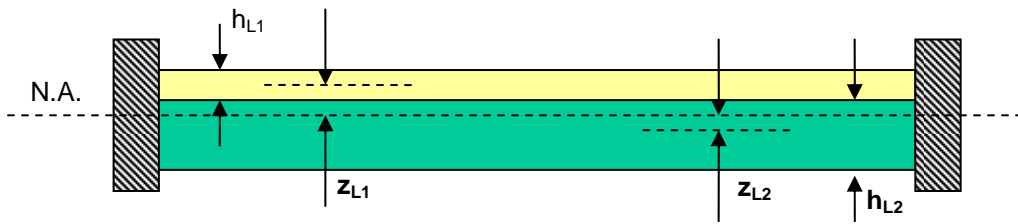


Figure 5.3: Definition of geometric constants for an isotropic bi-layer plate.

## 5.5 Impregnation Techniques

Two different techniques were employed to impregnate the buckypaper, as described below.

### 5.5.1 Vacuum Infiltration Technique

In this technique, a vacuum pressure of 1 Bar was applied to the system to infiltrate the buckypaper with epoxy MY0510 resin. A breather was used to transfer the negative pressure to one side of the buckypaper. A release film was inserted between the buckypaper and the breather to separate the buckypaper from the breather after impregnation. The requisite amount of resin was placed over the buckypaper using a stirring rod (This amount was calculated based on the approximate porosity of the buckypaper, i.e. ~70%). A thin layer of vacuum tape was used to prevent the resin from escaping at the edges of the buckypaper (Figure 5.4).

This resin has a viscosity of 10 Pa.s at room temperature and this viscosity decreases to 0.1 Pa.s when the temperature is increased to 100°C. Figure 5.5 shows the viscosity of MY0510 epoxy system as a function of time for four different temperatures (60, 100, 120, and 140°C). This curve was obtained through the rheological experiment conducted on a TA instruments AR2000 Rheometer with the Environmental Test Chamber (ETC) accessory (For more details, please refer to [131]). Based on Figure 5.5, an infiltration at 100°C is preferable as the viscosity of the resin is minimized and does not significantly change with time.

In accordance with Darcy's law for one-dimensional flow, the infiltration time ( $t$ ) is given by [119]:

$$t = \frac{\eta h^2}{2K_f \Delta P} \quad (5.10)$$

Here,  $\eta$  is the viscosity of the resin,  $h$  is the film's thickness,  $\Delta P$  is the vacuum pressure, and  $K_f$  is the permeability of the film.

Wang *et al.* [74] obtained a permeability ( $K_i$ ) of  $2 \times 10^{-19} \text{ m}^2$  through the thickness of the film. As a first approximation, the permeability of our buckypaper was considered to be equal to this value. As a result, an impregnation time of around 2.5 hours was necessary to impregnate the sample for a typical thickness of  $60 \text{ }\mu\text{m}$ , a vacuum pressure of 1 Bar, and a viscosity of 0.1 Pa.s. Figure 5.6 shows the modified cure cycle used to cure the resin. In this cycle, a holding time of 3 hours was added to the original cure cycle at  $100^\circ\text{C}$  to increase the time for the impregnation of the buckypaper.

After removing the sample, the bottom surface of the film was rough because it had been in contact with the release film. The other surface adjacent to the glass substrate was, however, mirror-like. Since the characterization technique based on bending test is very sensitive to the thickness uniformity of each film, sand papers of different grades (600 and 800 Grits) were used to polish the rough surface until a uniform surface finish was achieved.

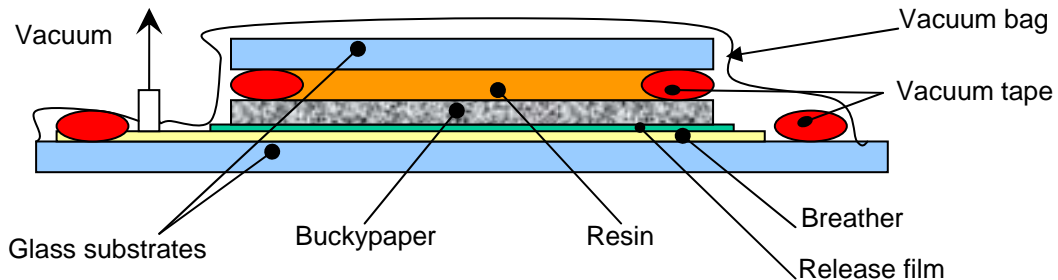


**Figure 5.4: Schematic illustration of the vacuum infiltration technique used for impregnation of the buckypaper.**

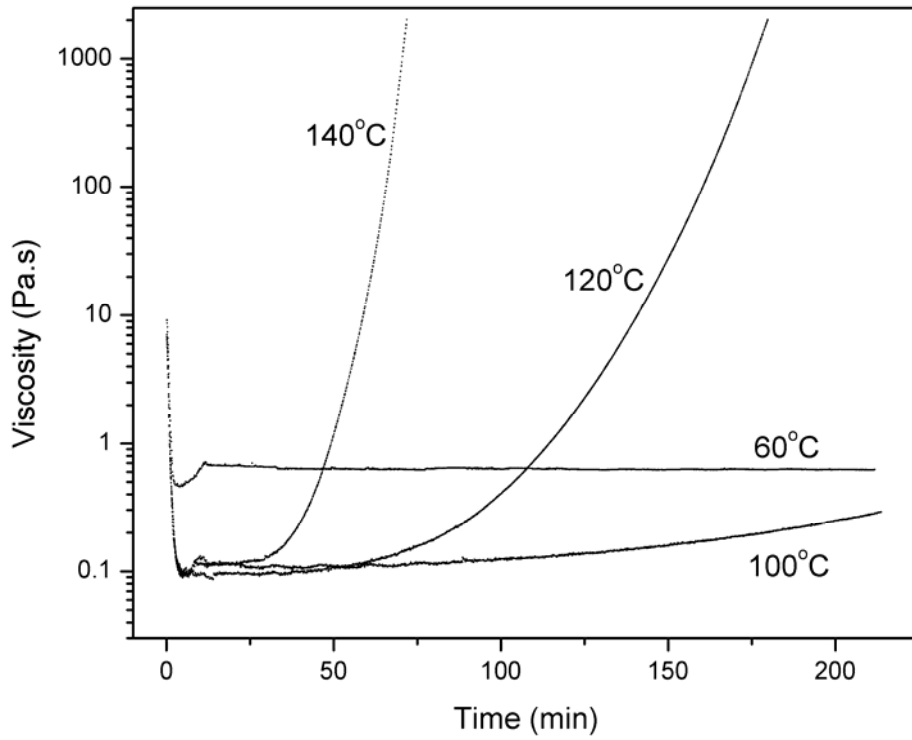


Figure 5.5: Viscosity of MY0510 epoxy system as a function of time for 4 different temperatures (adapted from [131])

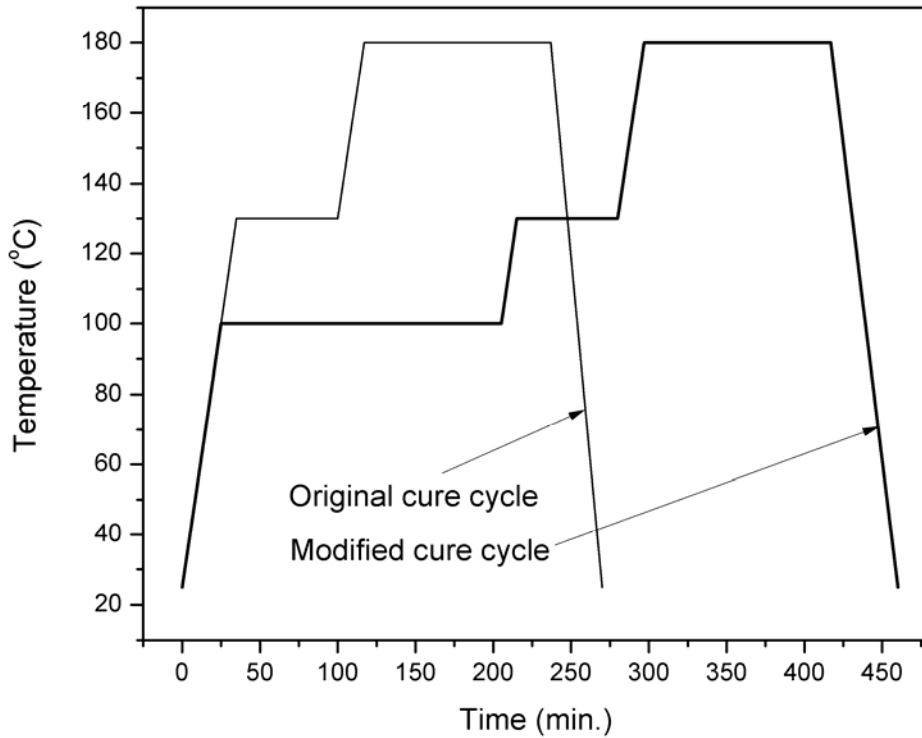


Figure 5.6: Modified cure cycle used during impregnation of buckypaper. For comparison, original cure cycle of MY0510 epoxy is also shown.

## 5.5.2 Hot-Press Technique

In this method, a hot-press was utilized to impregnate buckypaper. An appropriate amount of resin was placed on the buckypaper. An O-ring was used to confine the resin and eliminate leakage to the outside of the cavity. A steel shim was used to control the thickness. In this technique, the two plates were placed in contact with each other but no excessive pressure was applied to the top plate (Figure 5.7). Then, the steel plates were heated to 100°C. The temperature is consistent with the minimum viscosity of the resin (Figure 5.5). A pressure of 40 MPa was then applied to the system for 4 hours, letting resin infiltrate the buckypaper. After removing the sample, both sides of the film were polished. Since both surfaces of the film were in contact with the polished steel plates, a minor polishing was sufficient to achieve a uniform film suitable for nanoindenter-based bending tests.

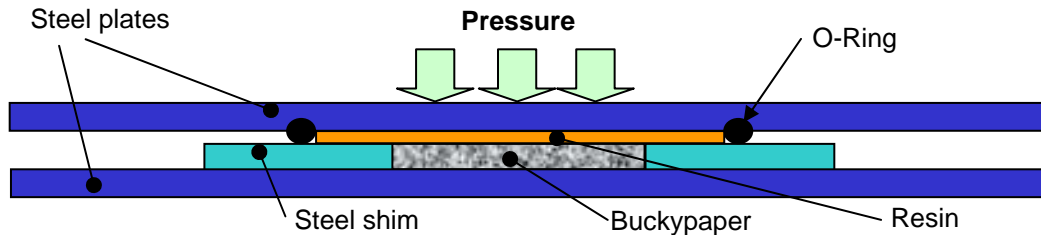


Figure 5.7: Schematic illustration of the hot-press technique for impregnation of buckypaper

## 5.6 Results of Resin-Impregnated Buckypaper Sheets

### 5.6.1 Characterization through Scanning Electron Microscope

In order to characterize the quality of impregnation, a careful inspection was performed through the thickness of fractured impregnated samples. Figure 5.8 shows a cross-sectional view of a vacuum-infiltrated specimen. A comparison between pristine buckypaper and impregnated buckypaper clearly shows a very different morphology proving the infiltration of resin into the buckypaper (Figure 5.8-a). The presence of small air bubbles is also clear in the images of impregnated buckypaper images. A higher magnification of the broken cross-

section of composites shows the evidence for bridging of CNT rope. A careful observation of pristine buckypaper with a magnification of 25K (Figure 5.1-b) demonstrates that carbon nanotube ropes are very long as their beginnings and ends were only occasionally observed. However, in Figure 5.8-b, considerable numbers of carbon nanotube endings can be observed. This proves the bridging of CNTs before their ultimate fracture due to the rupture of buckypaper composites. The presence of a considerable number of straightened ropes in Figure 5.8-b further demonstrates the bridging of CNT ropes as they were compared with the wavy CNT ropes of pristine buckypaper (Figure 5.1-b). The formation of a thin layer of polymer on one side of impregnated samples is shown in Figure 5.8-c. This layer is adjacent to the top glass substrate. This layer was not present on the other surface as the surface had been polished. The thickness of this layer varied from 3 to 10  $\mu\text{m}$  was measured after the specimen was tilted perpendicular to the scanning electrons.

Figure 5.9 shows SEM images of the samples manufactured by a hot-press technique. Two distinct regions can be observed in these samples (Figure 5.9-a); i.e. a resin-rich region and a non-impregnated region. Under pressure, resin is forced to penetrate buckypaper. Due to the extremely low permeability of buckypaper, the resin displaces the ropes to build channels through the buckypaper. These channels have lateral dimensions of a few micrometers. Also, the air trapped between the two steel substrates and the O-ring (Figure 5.6) will prevent an efficient infiltration of resin into the buckypaper. This is unlike the samples impregnated through vacuum techniques in which the vacuum is applied more consistently to the resin, resulting in a more uniform impregnation of the buckypaper. Figure 5.9-b shows a magnified view at the boundary of the two regions of a hot-press sample, suggesting that the resin wets the CNT ropes well. However, Figure 5.9-c shows the lack of resin in the middle of non-impregnated regions.

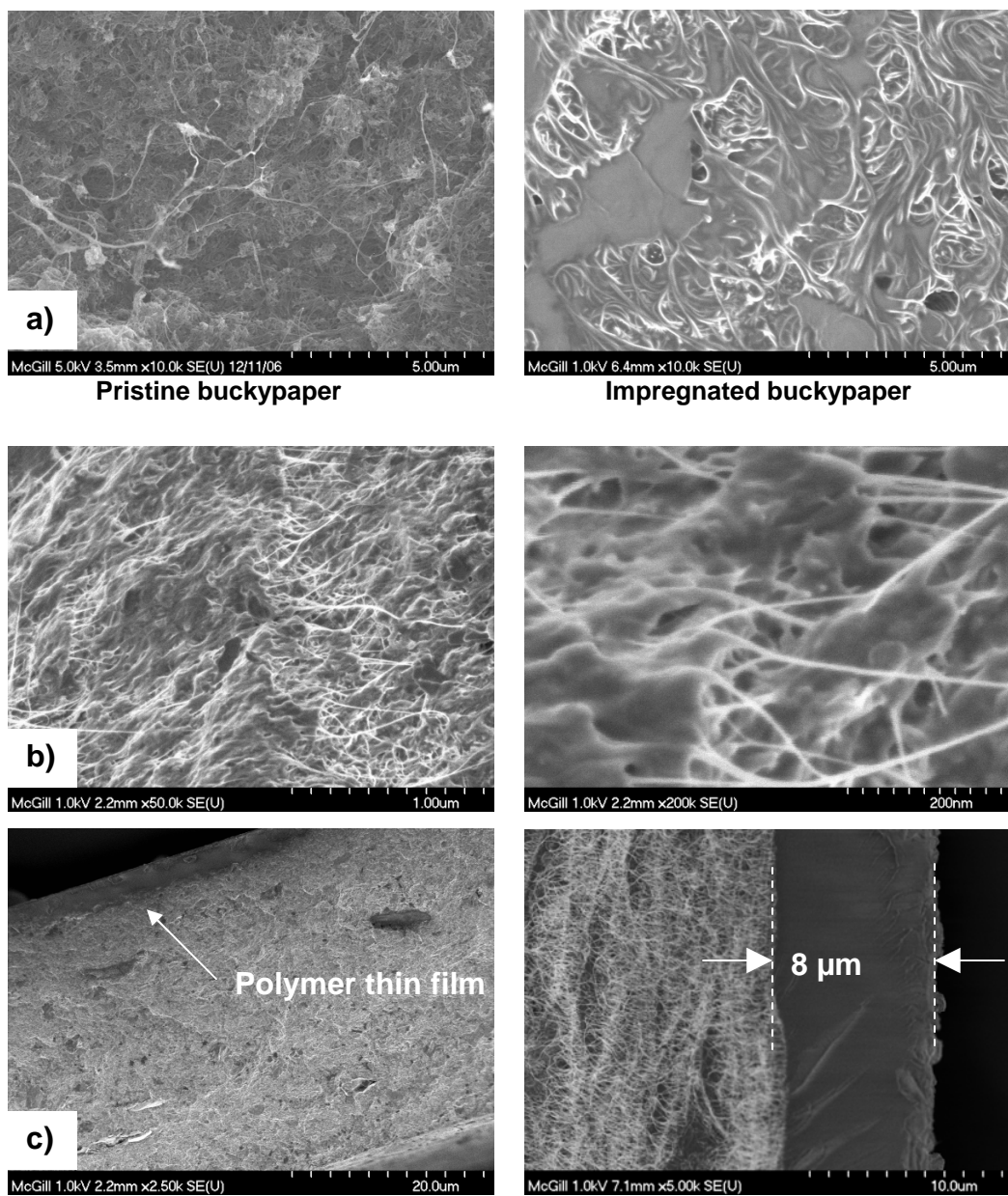


**Figure 5.8: Cross-sectional view of vacuum-infiltrated samples. a) A comparison between pristine buckypaper and impregnated buckypaper. b) A broken surface with magnifications of 50K and 200K showing the bridging effect of CNT c) An 8  $\mu\text{m}$ -thick layer of resin film at one edge of the sample.**

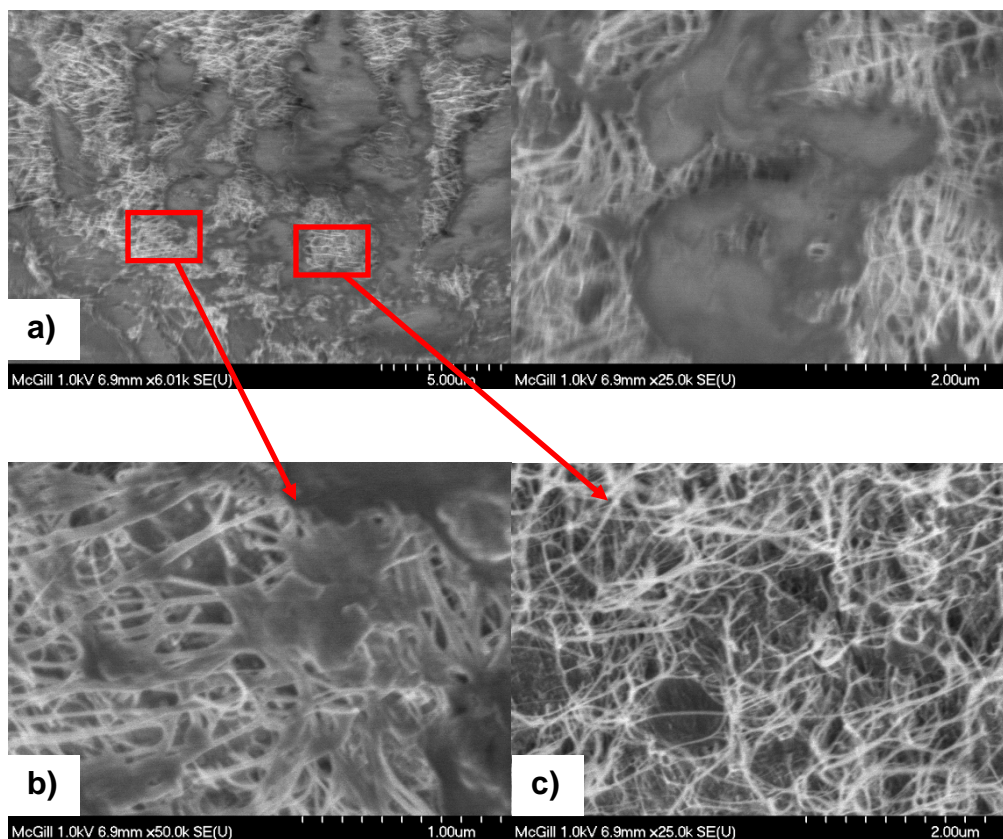


**Figure 5.9: Cross-sectional view of hot-press samples. a) Two distinct regions can be differentiated: a resin-rich region and a non-impregnated region. b) Good resin wetting can be observed at the boundary of these two regions. c) There is no sign of resin infiltration in the middle of the CNT-rich region.**

## 5.6.2 Characterization of Elastic Properties

Nanoindenter-based bending tests were performed to characterize the impregnated buckypaper. Figure 5.10 exhibits three representative load-deflection curves obtained from the nanoindenter-based bending tests of a buckypaper film, a resin film, and their composite film. All three films have comparable film thicknesses. Arrows in this figure show loading and unloading directions. The load-deflection curves of both polymer and nanocomposite films are linear demonstrating the dominant bending behavior of the film. For each case, the loading part of the curve overlaps the unloading part, indicating that the deformation is dominantly elastic in nature. The curve corresponding to the pristine buckypaper, however, is non-linear and non-overlapping. This can be attributed to the compaction of the

porous buckypaper due to the applied load resulting in a permanent deformation of around 500 nm as can be seen in this figure. Moreover, the stiction of the pristine buckypaper to the diamond tip might be responsible for the negative force detected during unloading. For both impregnation techniques, Equations (5.5) and (5.6) were used to extract the Young's modulus of the composite film. In the case of the vacuum impregnated technique, however, a thin layer of polymer forms on one side of the composite. For this reason, the theory of bi-layer composites developed in Section 5.4 was utilized to extract the Young's modulus of the resin-impregnated buckypaper. In this method, by estimating  $P/\delta$  from the load deflection curve, Equation (5.5) was used to extract the bending stiffness of the bi-layer composite film ( $D_{II}$ ). Then, knowing the thickness of the polymer film from SEM images as well as its Young's modulus (3.4 GPa), Equation (5.9) was used to extract the Young's modulus of the resin-impregnated buckypaper film. Table 5.5 summarized the results from both techniques. A comparison between the second and the third columns shows that accounting for the presence of the thin layer of polymer films causes an overall reduction of 20% of the Young's modulus of the bi-layer films when compared to the Young's modulus of impregnated buckypaper films.

**Table 5.5: Young's modulus of polymer-impregnated buckypaper (GPa)**

Sample name	Vacuum technique		Hot-press technique
	Bi-layer film {Equation (5.6)}	CNT/polymer film {Equation (5.9)}	CNT/polymer film {Equation (5.6)}
Sample 1	5.8 (GPa)	6.4 (GPa)	4.1 (GPa)
Sample 2	12.6 (GPa)	15.4 (GPa)	3.1 (GPa)
Sample 3	6.5 (GPa)	7.3 (GPa)	3.8 (GPa)
Sample 4	11.6 (GPa)	14.5 (GPa)	2.9 (GPa)
<b>Average</b>	<b>9.2±3.5 (GPa)</b>	<b>11.0±4.7 (GPa)</b>	<b>3.5±0.5 (GPa)</b>

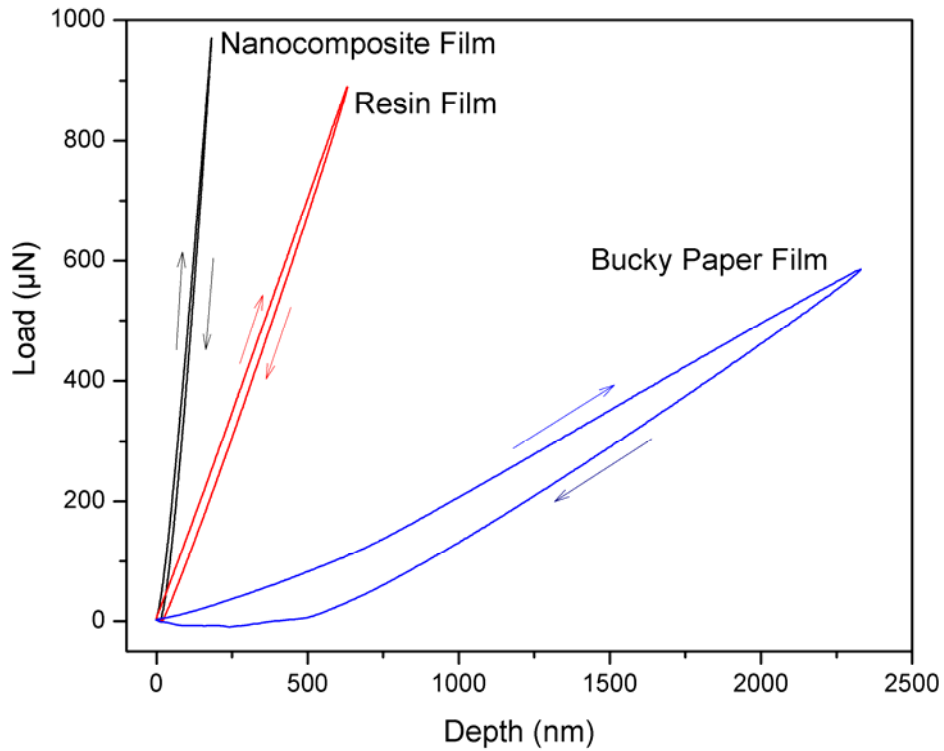


**Figure 5.10: Load-deflection curves for buckypaper, resin, and resin-infiltrated buckypaper composite manufactured by vacuum infiltration.**

Figure 5.11 compares elastic properties of different films (epoxy, buckypaper and resin-impregnated buckypaper films) with theoretical values predicted through Mori-Tanaka's approach. In theoretical calculations, an aspect ratio of 1000 was assigned to the SWNT arrays.

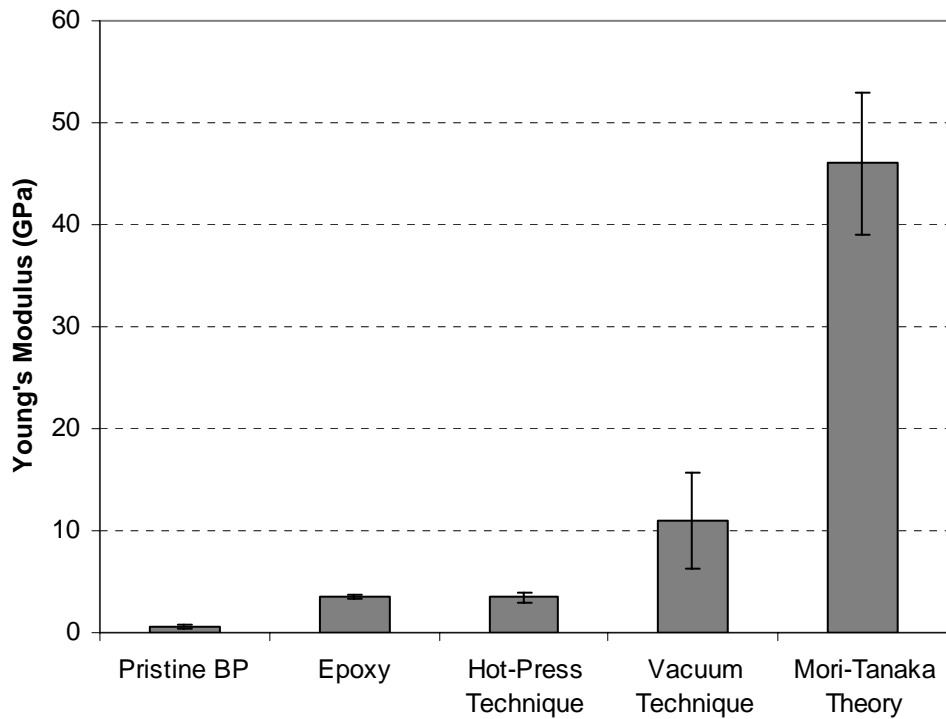


Figure 5.11: A comparison between different films (pure epoxy, pristine buckypaper and impregnated buckypaper) and theoretical prediction using Mori-Tanaka technique.

## 5.7 Summary

Polymer-impregnated buckypaper sheets manufactured through the vacuum infiltration technique produced a 3-fold increase in the Young's modulus with respect to that of pure resin. This result was comparable to the best results obtained through other experimental work reported earlier in the literature (Table 5.2). However, theoretical results obtained through Mori-Tanaka approach suggest the possibility of a further increase of three to four times in the elastic properties of impregnated buckypaper (Figure 5.11). Some of the factors that hold the key to these improvements are enumerated below.

1. The approach of Mori and Tanaka considers a perfect load transfer between resin and nanotubes, which can overestimate the elastic properties in real cases when the bonding between resin and tubes is not perfect.

2. In the theoretical calculations, a longitudinal Young's modulus of 580 GPa was assigned to the SWNT arrays. This value is for ideal SWNT arrays and obtained through molecular dynamics simulations [36, 132]. In as-manufactured materials, however, the presence of defects and missing SWNT inside arrays can result in degraded mechanical properties of SWNT arrays. A drop in the elastic properties of SWNT arrays will significantly decrease the predicted Young's modulus of the resin-impregnated buckypaper sheets.
3. The impregnation process of buckypaper sheets was not perfect and the presence of voids was detected by SEM images. This can be responsible for the relatively large standard deviation in the Young's modulus of vacuum infiltrated buckypaper sheets.
4. SEM images show a considerable quantity of impurities inside the pristine buckypaper (Figure 5.1). As a result, the presence of a higher percentage of impurities inside buckypaper sheets than the one considered in this work (10%) is feasible. This will reduce the actual volume fraction of SWNT arrays inside buckypaper, resulting in a reduction of elastic properties.

## Chapter 6

### Summary and Future Work

This work employed a combination of theoretical and experimental techniques to investigate the applicability of CNT composites for microstructures. The contributions of this work are summarized as follows.

**A combined framework of micromechanics and structural mechanics of composite materials was used to address different characteristics of carbon nanotube-based nanocomposites.** This included the choice of matrix as well as the type, volume fraction, aspect ratio and alignment of carbon nanotubes. One important assumption was the fact that the interfacial bonding between nanotubes and matrix was optimized for perfect load transfer. In this sense, the results presented in Chapter 2 represent upper bounds for the mechanical properties. These bounds were consistent with measurements reported in the literature. This comparison had to be interpreted only in a qualitative sense because many important parameters such as the orientation and distribution of nanotubes and the quality of nanotube-matrix bonding have not been reported in experimental studies. Therefore, the primary conclusion was that the analysis based on continuum mechanics is a useful first step in the design and analysis of nanotube-reinforced composites. Polymer-matrix nanocomposites reinforced with aligned, dispersed SWNT were identified as excellent candidates for microstructures with properties rivaling those of metallic- and ceramic-structures used in the current generation of microelectromechanical systems (MEMS).

**A new technique was developed to characterize the elasticity of soft thin films, i.e. polymer and polymer-based composite films.** A need for a new technique arose from the fact that traditional techniques such as tensile tests, bending and stretch tests, bulge tests and nanoindentation, presented difficulties

for the elastic characterization of soft thin films. The proposed technique was based on the bending behaviour of the films. A combination of theoretical, numerical, and experimental techniques was used to validate this method and a maximal error of 11% was identified between theoretical and finite-element calculations of contact indentation. Therefore, a nanoindentation-based method for assessing contact indentation was also developed. This resulted in more accurate measurements of the Young's moduli of polymer thin films. An evaluation of contact indentation using the Hertzian theory underestimated the elastic properties of polymers examined in this work (epoxy and LDPE). One primary reason resulting in this underestimation was the effect of the surface roughness of samples, which is more pronounced for shallow indents of rough surfaces. This surface effect, however, did not play a significant role on the sample characterized by the combined plate-indentation method because the effect of roughness appears in both the plate test and nanoindentation. As a result, the effect is cancelled out when pure bending deflection is calculated. A combination of the simplicity of the setup, uniform application of clamped boundary conditions as well as accurate measurements of force and displacements made the nanoindenter-based bending test a versatile technique for elastic characterization of polymer based thin films.

**The choice of polymer matrix plays an important role on the performance of nanocomposite thin films.** Results obtained through the characterization of epoxy-matrix nanocomposite films showed no increase in the elastic properties. Poor dispersion of nanotubes in the matrix is the primary source of the difference between theoretical and experimental predictions as evidenced by agglomerations observed in optical micrographs. For the case of epoxy vinyl ester mixtures, however, an increase compatible with theoretical predictions was measured in elastic properties upon adding SWNTs. As evidenced by optical micrographs, there is a much better dispersion of SWNTs inside epoxy vinyl ester resin. The discrepancy between these two systems can be attributed to the differences in the quality of interactions between polymer molecules and carbon nanotubes. A poor

interaction between carbon nanotubes and the epoxy resin system can be responsible for the poor mechanical properties of carbon nanotube/epoxy thin films.

**Carbon nanotube sheets (buckypaper) with a relatively high content of carbon nanotubes (30-40% by volume) were identified as good candidates for the manufacture of high quality nanocomposite thin films.** Two different techniques were utilized to impregnate pristine buckypaper sheets. The first technique was based on the application of pressure to inject resin into the buckypaper (hot-press technique). SEM images demonstrated that there were two distinct regions in these samples: a resin-rich region and a non-impregnated region. This fact was consistent with the results obtained through the elastic characterization of these films in which no improvement in the elastic modulus was found for hot-press samples. The second technique for the impregnation of the buckypaper was through the application of vacuum pressure. A more uniform impregnation was also observed through SEM. A three- to four-fold increase in Young's modulus was measured through the nanoindenter-based bending tests and was consistent with observations based on SEM micrographs. However, theoretical results obtained through Mori-Tanaka approach suggested the possibility of a further increase of three to four times in the elastic properties of impregnated buckypaper, demonstrating significant potential of the resin-impregnated buckypaper films for microstructures.

A qualitative comparison between the experimental results and the predicted upper bound on property values highlights the huge improvements needed in materials processing to realize the potential of carbon nanotubes for reinforcing small structures. The following subjects could be investigated in the future:

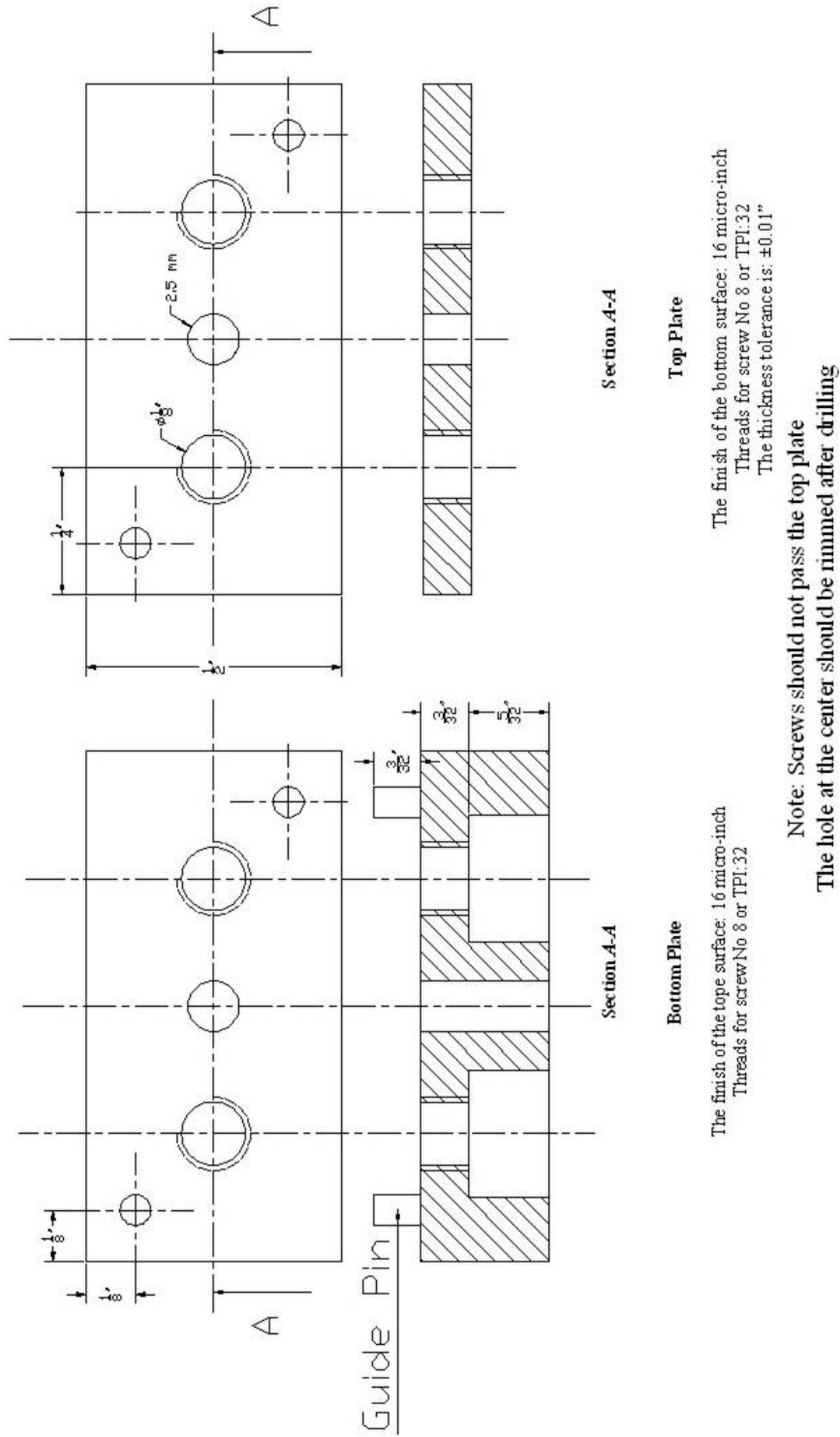
- 1) Results obtained through continuum mechanics are based on the assumption that the load transfer between carbon nanotubes and polymer chains are ideal. In that sense, these results can only calculate the upper bounds for the

properties. Moreover, experimental results presented in Chapter 4 prove that the choice of matrix plays an important role on the quality of carbon nanotube-polymer interactions. As a result, a more thorough analysis of carbon nanotube-polymer interaction based on non-continuum models such as molecular dynamics (MD) could be a very strong tool for improving the modelling techniques. This will help identify ideal polymers to manufacture high performance composite materials. A multiscale model combining continuum and non-continuum techniques is perhaps the ideal, computationally reasonable scheme. Here, the interaction between carbon nanotubes and polymer can be first modeled using non-continuum techniques. These results will be considered as inputs for continuum models. Then, continuum mechanics techniques can be used to obtain the properties of the nanocomposites (A similar approach has been already examined by few researchers [52, 133]).

- 2) Errors involved with the new technique developed in Chapter 3 for the elastic characterization of polymer-based thin films is approximately 10%. One primary reason for this error is because of the evaluation of contact indentation through Hertzian theory. The sample roughness is probably the major reason responsible for this error. A thorough analysis of the surface roughness is therefore essential for improving the accuracy of this technique.
- 3) One important requirement of nanocomposite manufacturing is the uniform dispersion of inclusions inside the matrix. For dilute nanocomposite thin films, we utilized optical micrographs used for an evaluation of the carbon nanotube dispersion. Due to the dimensions of carbon nanotubes, optical microscopes are not accurate enough to precisely assess the quality of the carbon nanotube dispersion. As a result, techniques with higher magnification and resolution, such as transmission electron microscopy, are needed for a detailed evaluation of dispersion.

- 4) Based on results obtained through theoretical predictions, increasing the carbon nanotube volume fraction and alignment are the two most important factors in the manufacture of high-performance composite films. As a result, buckypaper sheets are interesting materials due to their high CNT volume fractions (30-40%). However, pristine buckypaper sheets have random, entangled carbon nanotubes. As a result, in order to improve the applicability of buckypaper sheets, it is necessary to align carbon nanotubes inside the buckypaper. Researchers have tried different techniques to align carbon nanotubes inside resin using magnetic or electric fields [33, 134]. An integration of alignment techniques with an impregnation method is perhaps one possible way to manufacture high quality nanocomposite films.
  
- 5) While the experimental results of Chapter 4 and 5 are based on freestanding thin films, the ultimate application of these materials for microstructures is only possible if these nanocomposites can be merged with traditional microfabrication techniques. This fact can be viewed as a natural continuation of this research. One possible solution is the application of vertically aligned carbon nanotubes. Different researchers have tried to grow carbon nanotubes on various substrates in the form of aligned tubes [135, 136]. A few researchers have tried to impregnate aligned tubes with resin [16, 136]. Considering the inherent alignment of carbon nanotubes, this configuration has great potential for the manufacture of microstructures.

# Appendix 1: Blueprint of the Fixture for Bending Test of Soft Thin Films



## **Appendix 2: Processing of CNT/Polymer Composite Films**

While there are a few reports on the manufacturing of metal- and ceramic-matrix CNT composites, most research focuses on polymer-matrix CNT composites. This is due to the fact that polymers are attractive materials in terms of manufacturability, price and weight. However, they typically suffer from inferior mechanical properties. This motivates researchers to assess the applicability of reinforcing polymers by strong nano-inclusions including carbon nanotubes. Several methods for making carbon nanotubes are reported in the literature. The most widely used methods are: arc-evaporation technique, laser ablation and chemical vapor deposition. More details of each technique can be found in the Master's thesis of the author [41].

Researchers have tried various techniques to process polymer-matrix CNT composites whose final products are in the form of films or fibres. Depending on the final product, the processing techniques are inherently different. The focus of this section is to review only the most common techniques for film processing. Readers can refer to excellent review papers by Coleman [29, 30] for fibre manufacturing and less common film manufacturing techniques. Depending on the type of polymers (thermoset versus thermoplastic) the manufacturing techniques can also be slightly different.

### **A 2.1: Solution Processing Technique**

This technique is the most common technique for manufacturing CNT composites [56-59, 68-70]. In this technique, carbon nanotubes are dissolved inside an appropriate solvent. An agitation technique, mostly sonication, is then used to disperse carbon nanotubes. This is a critical step as most carbon nanotubes, more specifically single-walled carbon nanotubes, tend to form bundles and because the intermolecular forces, for example Van der Waals forces, between them is very strong, it is extremely difficult to de-bundle them. Then, the polymer is added to the solvent and agitation is repeated to make a uniform mixture. Finally, the CNT/polymer paste is manufactured by the evaporation of the solvent. While

sonication is the most common technique for agitation, other sources of mixing including shear, magnetic and reflux are also used [29]. One critical factor for the success of this technique is the choice of the solvent. The solvent should be chosen carefully in order to guarantee that both polymer and carbon nanotubes are dissolved in it. Considering the fact that CNTs are inert, it is very difficult to disperse them uniformly inside most solvents. Another major limitation of this technique is the fact that it can only be used for soluble polymers.

### **A 2.2: Melt Processing Technique**

In this technique carbon nanotubes are directly added to the polymer. This technique can only be used for thermoplastic polymers [64-67]. First, a polymer is first heated until it is sufficiently viscous. For amorphous thermoplastics, the temperature is typically above thermal glass transition ( $T_g$ ) while for semi-crystalline thermoplastics, this temperature is above the melting temperature. After that, carbon nanotubes are added to the heated polymers. Depending on the type of polymer, mechanical mixing techniques, mostly shear mixing, are used to disperse carbon nanotube inside the polymers. This technique is susceptible to several drawbacks including

1. Carbon nanotubes damage or break during mixing
2. Polymer degradation due to a high shear rate
3. Change in polymer crystals due to the presence of CNTs

### **A 2.3: In Situ Polymerization Technique**

The main goal here is to graft polymer molecules directly to the carbon nanotubes [71-73]. Therefore, the method has a few important advantages:

- 1) Composites with higher percentages of carbon nanotubes can be made.
- 2) Almost all types of polymers can be used.
- 3) A better interaction between carbon nanotube and polymer can be provided.

This type of processing results in two types of interactions between carbon nanotube and polymer chains: non-covalent bonding (for example, Van der Waals) and covalent bonding through functionalization. Functionalization has two

main advantages. First, it facilitates the dispersion of carbon nanotubes by modifying the surface of the carbon nanotube. Second, the functional group added to the surface can form a strong covalent bond with polymer chains increasing the interfacial interaction between them. One drawback of functionalization, however, is the fact that it can damage the carbon nanotube structure and reduce the mechanical properties as shown both theoretically [52] and experimentally [137].

#### **A 2.4: Carbon Nanotube Sheet**

Researchers have tried to manufacture composites using carbon nanotube sheets, also called buckypaper [117]. These sheets are typically formed by vacuum infiltration of a suspended solution of carbon nanotubes. A few researchers have tried to manufacture composites by impregnating buckypaper sheets. The main advantage of this technique is the possibility of manufacturing composites with a high percentage of CNT composites. A more detailed analysis on the properties of buckypaper, impregnation techniques and their properties is given in Chapter 5.

## Appendix 3: Raw Data

Table B3.1: Epoxy thin films

Sample	Force ( $P_{max}$ )	Total Deflection ( $\delta_T$ )	Contact Deflection ( $\delta_C$ )	Film Thickness (h)
MY-1	9.59E-04 ± 3E-06 (μN)	2.35E-07 ± 1.5E-08 (nm)	8.31E-08 ± 1.54E-08 (nm)	101 (μm)
MY-2	9.33E-04 ± 8E-06 (μN)	3.88E-07 ± 4.4E-08 (nm)	1.50E-07 ± 4.3E-08 (nm)	71 (μm)
MY-3	8.17E-04 ± 5.5E-05 (μN)	1.06E-06 ± 3.1E-07 (nm)	1.43E-07 ± 4.3E-08 (nm)	42 (μm)

- Data used for Figure 3.15

Table B3.2: Low density polyethylene thin films

Sample	Force ( $P_{max}$ )	Total Deflection ( $\delta_T$ )	Contact Deflection ( $\delta_C$ )	Film Thickness (h)
LDPE-1	1.58E-03 (μN)	2.90E-06 (nm)	1.06E-06 (nm)	121 (μm)
LDPE-2	1.57E-03 (μN)	2.93E-06 (nm)	1.06E-06 (nm)	121 (μm)
LDPE-3	1.59E-03 (μN)	2.82E-06 (nm)	1.06E-06 (nm)	115 (μm)
LDPE-4	1.64E-03 (μN)	2.44E-06 (nm)	1.06E-06 (nm)	109 (μm)
LDPE-5	1.64E-03 (μN)	2.44E-06 (nm)	1.06E-06 (nm)	125 (μm)

- Data used for Figure 3.17

**Table B3.3: Epoxy nanocomposite thin films**

<b>Sample</b>	<b>Force (<math>P_{max}</math>)</b>	<b>Total Deflection (<math>\delta_T</math>)</b>	<b>Film Thickness (<math>h</math>)</b>
<b>Epoxy-1</b>	8.87E-04 ( $\mu\text{N}$ )	6.14E-07 (nm)	60 ( $\mu\text{m}$ )
<b>Epoxy-2</b>	8.90E-04 ( $\mu\text{N}$ )	5.95E-07 (nm)	54 ( $\mu\text{m}$ )
<b>Epoxy-3</b>	9.01E-04 ( $\mu\text{N}$ )	5.91E-07 (nm)	56 ( $\mu\text{m}$ )
<b>Epoxy-4</b>	8.83E-04 ( $\mu\text{N}$ )	5.88E-07 (nm)	57 ( $\mu\text{m}$ )
<b>Plasma 1-1</b>	8.90E-04 ( $\mu\text{N}$ )	6.14E-07 (nm)	63 ( $\mu\text{m}$ )
<b>Plasma 1-2</b>	8.93E-04 ( $\mu\text{N}$ )	5.95E-07 (nm)	66 ( $\mu\text{m}$ )
<b>Plasma 1-3</b>	8.95E-04 ( $\mu\text{N}$ )	5.91E-07 (nm)	69 ( $\mu\text{m}$ )
<b>Plasma 1-4</b>	8.95E-04 ( $\mu\text{N}$ )	5.88E-07 (nm)	60 ( $\mu\text{m}$ )
<b>Plasma 2-1</b>	8.83E-04 ( $\mu\text{N}$ )	6.14E-07 (nm)	65 ( $\mu\text{m}$ )
<b>Plasma 2-2</b>	8.90E-04 ( $\mu\text{N}$ )	5.95E-07 (nm)	62 ( $\mu\text{m}$ )
<b>Plasma 2-3</b>	8.87E-04 ( $\mu\text{N}$ )	5.91E-07 (nm)	69 ( $\mu\text{m}$ )
<b>Plasma 2-4</b>	8.90E-04 ( $\mu\text{N}$ )	5.88E-07 (nm)	61 ( $\mu\text{m}$ )
<b>Plasma 3-1</b>	8.84E-04 ( $\mu\text{N}$ )	6.14E-07 (nm)	61 ( $\mu\text{m}$ )
<b>Plasma 3-2</b>	8.91E-04 ( $\mu\text{N}$ )	5.95E-07 (nm)	69 ( $\mu\text{m}$ )
<b>Plasma 3-3</b>	8.88E-04 ( $\mu\text{N}$ )	5.91E-07 (nm)	66 ( $\mu\text{m}$ )
<b>Plasma 3-4</b>	8.90E-04 ( $\mu\text{N}$ )	5.88E-07 (nm)	59 ( $\mu\text{m}$ )
<b>Laser 1-1</b>	8.83E-04 ( $\mu\text{N}$ )	6.14E-07 (nm)	60 ( $\mu\text{m}$ )
<b>Laser 1-2</b>	8.90E-04 ( $\mu\text{N}$ )	5.95E-07 (nm)	66 ( $\mu\text{m}$ )
<b>Laser 1-3</b>	8.87E-04 ( $\mu\text{N}$ )	5.91E-07 (nm)	66 ( $\mu\text{m}$ )
<b>Laser 1-4</b>	8.90E-04 ( $\mu\text{N}$ )	5.88E-07 (nm)	59 ( $\mu\text{m}$ )
<b>Laser 2-1</b>	8.84E-04 ( $\mu\text{N}$ )	6.14E-07 (nm)	68 ( $\mu\text{m}$ )
<b>Laser 2-2</b>	8.90E-04 ( $\mu\text{N}$ )	5.95E-07 (nm)	69 ( $\mu\text{m}$ )
<b>Laser 2-3</b>	8.86E-04 ( $\mu\text{N}$ )	5.91E-07 (nm)	59 ( $\mu\text{m}$ )
<b>Laser 2-4</b>	8.92E-04 ( $\mu\text{N}$ )	5.88E-07 (nm)	61 ( $\mu\text{m}$ )

- Data used for Table 4.2

**Table B3.4: Vinyl ester epoxy nanocomposite thin films**

<b>Sample</b>	<b>Force (<math>P_{max}</math>)</b>	<b>Total Deflection (<math>\delta_T</math>)</b>	<b>Film Thickness (h)</b>
<b>VE-1</b>	8.87E-04 ( $\mu\text{N}$ )	6.36E-07 (nm)	60 ( $\mu\text{m}$ )
<b>VE-2</b>	8.90E-04 ( $\mu\text{N}$ )	6.18E-07 (nm)	54 ( $\mu\text{m}$ )
<b>VE-3</b>	9.01E-04 ( $\mu\text{N}$ )	5.54E-07 (nm)	56 ( $\mu\text{m}$ )
<b>VE-4</b>	8.83E-04 ( $\mu\text{N}$ )	6.61E-07 (nm)	57 ( $\mu\text{m}$ )
<b>VE+0.3SWNT-1</b>	8.90E-04 ( $\mu\text{N}$ )	4.04E-07 (nm)	63 ( $\mu\text{m}$ )
<b>VE+0.3SWNT-2</b>	8.93E-04 ( $\mu\text{N}$ )	3.89E-07 (nm)	66 ( $\mu\text{m}$ )
<b>VE+0.3SWNT-3</b>	8.95E-04 ( $\mu\text{N}$ )	3.55E-07 (nm)	69 ( $\mu\text{m}$ )
<b>VE+0.3SWNT-4</b>	8.95E-04 ( $\mu\text{N}$ )	5.31E-07 (nm)	60 ( $\mu\text{m}$ )
<b>VE+0.6SWNT-1</b>	8.83E-04 ( $\mu\text{N}$ )	3.82E-07 (nm)	65 ( $\mu\text{m}$ )
<b>VE+0.6SWNT-2</b>	8.90E-04 ( $\mu\text{N}$ )	3.98E-07 (nm)	62 ( $\mu\text{m}$ )
<b>VE+0.6SWNT-3</b>	8.87E-04 ( $\mu\text{N}$ )	2.82E-07 (nm)	69 ( $\mu\text{m}$ )
<b>VE+0.6SWNT-4</b>	8.90E-04 ( $\mu\text{N}$ )	5.13E-07 (nm)	61 ( $\mu\text{m}$ )

- Data used for Figure 4.4

**Table B3.5: Buckypaper thin films**

<b>Sample</b>	<b>Force (<math>P_{max}</math>)</b>	<b>Total Deflection (<math>\delta_T</math>)</b>	<b>Film Thickness (h)</b>
<b>Vac BP-1</b>	9.68E-04 ( $\mu\text{N}$ )	2.39E-07 (nm)	65 ( $\mu\text{m}$ )
<b>Vac BP-2</b>	9.71E-04 ( $\mu\text{N}$ )	1.82E-07 (nm)	54 ( $\mu\text{m}$ )
<b>Vac BP -3</b>	9.54E-04 ( $\mu\text{N}$ )	2.68E-07 (nm)	59 ( $\mu\text{m}$ )
<b>Vac BP-4</b>	9.46E-04 ( $\mu\text{N}$ )	3.11E-07 (nm)	57 ( $\mu\text{m}$ )
<b>HP BP-1</b>	9.69E-04 ( $\mu\text{N}$ )	1.66E-07 (nm)	90 ( $\mu\text{m}$ )
<b>HP BP-2</b>	9.59E-04 ( $\mu\text{N}$ )	2.39E-07 (nm)	85 ( $\mu\text{m}$ )
<b>HP BP-3</b>	9.65E-04 ( $\mu\text{N}$ )	1.90E-07 (nm)	90 ( $\mu\text{m}$ )
<b>HP BP -4</b>	9.57E-04 ( $\mu\text{N}$ )	2.52E-07 (nm)	85 ( $\mu\text{m}$ )
<b>BP-1</b>	6.72E-04 ( $\mu\text{N}$ )	1.86E-06 (nm)	60 ( $\mu\text{m}$ )
<b>BP-2</b>	7.95E-04 ( $\mu\text{N}$ )	1.16E-06 (nm)	69 ( $\mu\text{m}$ )
<b>BP-3</b>	7.06E-04 ( $\mu\text{N}$ )	1.66E-06 (nm)	71 ( $\mu\text{m}$ )
<b>BP-4</b>	5.86E-04 ( $\mu\text{N}$ )	2.33E-06 (nm)	66 ( $\mu\text{m}$ )

- Data used for Table 5.5 and Figure 5.11

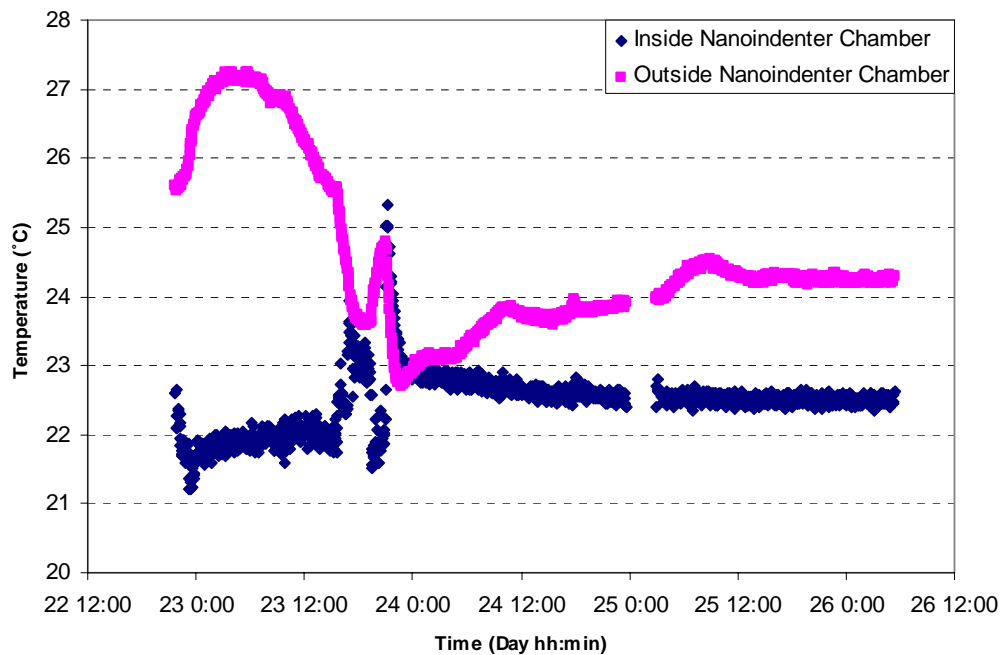


**Figure B3.1: Temperature variations inside and outside of the TriboIndenter's chamber for a period of four days from August 22, 2007 to August 26, 2007. The temperature inside the chamber varies between 22°C and 23°C and is more uniform than the temperature outside. A sudden change of the temperature inside chamber (a spike in above figure) is observed in August 23. This is happened due to an intentional opening of the nanoindenter's door.**

## References

1. Baughman, R.H., A.A. Zakhidov, and W.A. De Heer, *Carbon nanotubes - The route toward applications*. Science, 2002. **297**(5582): p. 787-792.
2. Vaia, R. and J. Baur, *Materials science: Adaptive composites*. Science, 2008. **319**(5862): p. 420-421.
3. Bekyarova, E., E.T. Thostenson, A. Yu, H. Kim, J. Gao, J. Tang, H.T. Hahn, T.W. Chou, M.E. Itkis, and R.C. Haddon, *Multiscale carbon nanotube-carbon fiber reinforcement for advanced epoxy composites*. Langmuir, 2007. **23**(7): p. 3970-3974.
4. Gojny, F.H., M.H.G. Wichmann, B. Fiedler, W. Bauhofer, and K. Schulte, *Influence of nano-modification on the mechanical and electrical properties of conventional fibre-reinforced composites*. Composites Part A: Applied Science and Manufacturing, 2005. **36**(11): p. 1525-1535.
5. Wichmann, M.H.G., J. Sumfleth, F.H. Gojny, M. Quaresimin, B. Fiedler, and K. Schulte, *Glass-fibre-reinforced composites with enhanced mechanical and electrical properties - Benefits and limitations of a nanoparticle modified matrix*. Engineering Fracture Mechanics, 2006. **73**(16): p. 2346-2359.
6. Thostenson, E.T., W.Z. Li, D.Z. Wang, Z.F. Ren, and T.W. Chou, *Carbon nanotube/carbon fiber hybrid multiscale composites*. Journal of Applied Physics, 2002. **91**(9): p. 6034.
7. Gong, Q.M., Z. Li, X.W. Zhou, J.J. Wu, Y. Wang, and J. Liang, *Synthesis and characterization of in situ grown carbon nanofiber/nanotube reinforced carbon/carbon composites*. Carbon, 2005. **43**(11): p. 2426-2429.
8. Li, X., K. Li, H. Li, J. Wei, and C. Wang, *Microstructures and mechanical properties of carbon/carbon composites reinforced with carbon nanofibers/nanotubes produced in situ*. Carbon, 2007. **45**(8): p. 1662-1668.
9. Li, C., E.T. Thostenson, and T.W. Chou, *Sensors and actuators based on carbon nanotubes and their composites: A review*. Composites Science and Technology, 2008. **68**(6): p. 1227-1249.
10. Dharap, P., Z. Li, S. Nagarajaiah, and E.V. Barrera, *Nanotube film based on single-wall carbon nanotubes for strain sensing*. Nanotechnology, 2004. **15**(3): p. 379-382.
11. Zhang, W., J. Suhr, and N. Koratkar, *Carbon nanotube/polycarbonate composites as multifunctional strain sensors*. Journal of Nanoscience and Nanotechnology, 2006. **6**(4): p. 960-964.
12. Kupke, M., K. Schulte, and R. Schuler, *Non-destructive testing of FRP by d.c. and a.c. electrical methods*. Composites Science and Technology, 2001. **61**(6): p. 837-847.
13. Thostenson, E.T. and T.W. Chou, *Carbon nanotube networks: Sensing of distributed strain and damage for life prediction and self healing*. Advanced Materials, 2006. **18**(21): p. 2837-2841.

14. Tsai, L.N., Y.T. Cheng, W. Hsu, and W. Fang, *Ni-carbon nanotubes nanocomposite for robust microelectromechanical systems fabrication*. Journal of Vacuum Science and Technology B: Microelectronics and Nanometer Structures, 2006. **24**(1): p. 205-210.
15. Shen, G.R., Y.T. Cheng, and L.N. Tsai, *Synthesis and characterization of Ni-P-CNT's nanocomposite film for MEMS applications*. IEEE Transactions on Nanotechnology, 2005. **4**(5): p. 539-547.
16. Fang, W., H.Y. Chu, W.K. Hsu, T.W. Cheng, and N.H. Tai, *Polymer-reinforced, aligned multiwalled carbon nanotube composites for microelectromechanical systems applications*. Advanced Materials, 2005. **17**(24): p. 2987-2992.
17. Bell, D.J., T.J. Lu, N.A. Fleck, and S.M. Spearing, *MEMS actuators and sensors: Observations on their performance and selection for purpose*. Journal of Micromechanics and Microengineering, 2005. **15**(7).
18. Senturia, S.D., *Microsystem Design*. 2001, Norwell, Ma: Kluwer Academic.
19. Qian, J. and Y.P. Zhao, *Materials selection in mechanical design for microsensors and microactuators*. Materials and Design, 2002. **23**(7): p. 619-625.
20. Srikar, V.T. and S.M. Spearing, *Materials selection for microfabricated electrostatic actuators*. Sensors and Actuators, A: Physical, 2003. **102**(3): p. 279-285.
21. Srikar, V.T. and S.M. Spearing, *Materials selection in micromechanical design: An application of the Ashby approach*. Journal of Microelectromechanical Systems, 2003. **12**(1): p. 3-10.
22. Ashby, M.F., *Materials Selection in Mechanical Design*. 2001, Oxford: Butterworth-Heinemann.
23. Zhang, G., J. Gaspar, V. Chu, and J.P. Conde, *Electrostatically actuated polymer microresonators*. Applied Physics Letters, 2005. **87**(10): p. 1-3.
24. Chou, T.W., *Microstructural Design of Fiber Composites*. 1992, Cambridge: Cambridge University Press.
25. Callister, W.D., *Materials Science and Engineering*. 2005, New York: Wiley.
26. Whitby, R.L.D., W.K. Hsu, Y.Q. Zhu, H.W. Kroto, and D.R.M. Walton, *Novel nanoscale architectures: Coated nanotubes and other nanowires*. Philosophical Transactions: Mathematical, Physical and Engineering Sciences (Series A), 2004. **362**(1823): p. 2127-2142.
27. Qian, D., G.J. Wagner, W.K. Liu, M.F. Yu, and R.S. Ruoff, *Mechanics of carbon nanotubes*. Applied Mechanics Reviews, 2002. **55**(6): p. 495-532.
28. Thostenson, E.T., C. Li, and T.W. Chou, *Nanocomposites in context*. Composites Science and Technology, 2005. **65**(3-4): p. 491-516.
29. Coleman, J.N., U. Khan, W.J. Blau, and Y.K. Gun'ko, *Small but strong: A review of the mechanical properties of carbon nanotube-polymer composites*. Carbon, 2006. **44**(9): p. 1624-1652.

30. Coleman, J.N., U. Khan, and Y.K. Gun'ko, *Mechanical reinforcement of polymers using carbon nanotubes*. *Advanced Materials*, 2006. **18**(6): p. 689-706.
31. Dequesnes, M., S.V. Rotkin, and N.R. Aluru, *Calculation of pull-in voltages for carbon-nanotube-based nanoelectromechanical switches*. *Nanotechnology*, 2002. **13**(1): p. 120-131.
32. Lefevre, R., M.F. Goffman, V. Derycke, C. Miko, L. Forro, J.P. Bourgoin, and P. Hesto, *Scaling law in carbon nanotube electromechanical devices*. *Physical Review Letters*, 2005. **95**(18): p. 1-4.
33. Xie, X.L., Y.W. Mai, and X.P. Zhou, *Dispersion and alignment of carbon nanotubes in polymer matrix: A review*. *Materials Science and Engineering R: Reports*, 2005. **49**(4).
34. Shen, L. and J. Li, *Transversely isotropic elastic properties of single-walled carbon nanotubes*. *Physical Review B - Condensed Matter and Materials Physics*, 2004. **69**(4): p. 454141-4541410.
35. Shen, L. and J. Li, *Transversely isotropic elastic properties of multiwalled carbon nanotubes*. *Physical Review B - Condensed Matter and Materials Physics*, 2005. **71**(3): p. 1-10.
36. Ashrafi, B. and P. Hubert, *Modeling the elastic properties of carbon nanotube array/polymer composites*. *Composites Science and Technology*, 2006. **66**(3-4): p. 387-396.
37. Schadler, L.S., S.C. Giannaris, and P.M. Ajayan, *Load transfer in carbon nanotube epoxy composites*. *Applied Physics Letters*, 1998. **73**(26): p. 3842-3844.
38. Ajayan, P.M., L.S. Schadler, C. Giannaris, and A. Rubio, *Single-walled carbon nanotube-polymer composites: Strength and weakness*. *Advanced Materials*, 2000. **12**(10): p. 750-753.
39. Liu, L., A.H. Barber, S. Nuriel, and H.D. Wagner, *Mechanical properties of functionalized single-walled carbon-nanotube/ poly(vinyl alcohol) nanocomposites*. *Advanced Functional Materials*, 2005. **15**(6): p. 975-980.
40. Frankland, S.J.V., A. Caglar, D.W. Brenner, and M. Griebel, *Molecular simulation of the influence of chemical cross-links on the shear strength of carbon nanotube-polymer interfaces*. *Journal of Physical Chemistry B*, 2002. **106**(12): p. 3046-3048.
41. Ashrafi, B., *Modeling the elastic properties of carbon nanotube arrays and their composites*, in *Mechanical Engineering*. 2004, Master's Thesis, McGill, Montreal p. 124.
42. Tucker Iii, C.L. and E. Liang, *Stiffness predictions for unidirectional short-fiber composites: Review and evaluation*. *Composites Science and Technology*, 1999. **59**(5): p. 655-671.
43. Halpin, J.C., *Stiffness and Expansion Estimates for Oriented Short Fiber Composites*. *Journal of Composite Materials*, 1969. **3**: p. 732-734.
44. Halpin, J.C. and J.L. Kardos, *Halpin-Tsai equations: a review*. *Polymer Engineering and Science*, 1976. **16**(5): p. 344-352.
45. Hill, R., *Elastic Properties of Reinforced Solids: Some Theoretical Principles* *Journal of Mechanics and Physics of Solids*, 1963. **11**: p. 357.

46. Eshelby, J.D., *The determination of the elastic field of an ellipsoidal inclusion, and related problems*. Proc. R. Soc., 1957. **241**: p. 376-396.
47. Clyne, T.W. and P.J. Withers, *An Introduction to Metal Matrix Composites*. 1993, Cambridge: Cambridge University Press.
48. Mori, T. and k. Tanaka, *Average Stress in Matrix and Average Elastic Energy of Materials with Misfitting Inclusions*. Acta Metallurgica 1973. **21**(5): p. 571-574.
49. Benveniste, Y., *New Approach to the Application of Mori-Tanaka's Theory in Composite Materials*. Mechanics of Materials, 1987. **6**(2): p. 147-157.
50. Mura, T., *Micromechanics of Defects in Solids*. 1987, Dordrecht: Kluwer-Academic.
51. Chen, C.H. and C.H. Cheng, *Effective elastic moduli of misoriented short-fiber composites*. International Journal of Solids and Structures, 1996. **33**(17): p. 2519-2539.
52. Odegard, G.M., T.S. Gates, K.E. Wise, C. Park, and E.J. Siochi, *Constitutive modeling of nanotube-reinforced polymer composites*. Composites Science and Technology, 2003. **63**(11): p. 1671-1687.
53. Thostenson, E.T. and T.W. Chou, *On the elastic properties of carbon nanotube-based composites: Modelling and characterization*. Journal of Physics D: Applied Physics, 2003. **36**(5): p. 573-582.
54. Pipes, R.B., S.J.V. Frankland, P. Hubert, and E. Saether, *Self-consistent properties of carbon nanotubes and hexagonal arrays as composite reinforcements*. Composites Science and Technology, 2003. **63**(10): p. 1349-1358.
55. King, J.L., *free transverse vibrations of anisotropic beams*. Journal of Sound and Vibration, 1985. **98**(4): p. 575-585.
56. Qian, D., E.C. Dickey, R. Andrews, and T. Rantell, *Load transfer and deformation mechanisms in carbon nanotube-polystyrene composites*. Applied Physics Letters, 2000. **76**(20): p. 2868-2870.
57. Ruan, S.L., P. Gao, X.G. Yang, and T.X. Yu, *Toughening high performance ultrahigh molecular weight polyethylene using multiwalled carbon nanotubes*. Polymer, 2003. **44**(19): p. 5643-5654.
58. Cadek, M., J.N. Coleman, K.P. Ryan, V. Nicolosi, G. Bister, A. Fonseca, J.B. Nagy, K. Szostak, F. Beguin, and W.J. Blau, *Reinforcement of Polymers with Carbon Nanotubes: The Role of Nanotube Surface Area*. Nano Letters, 2004. **4**(2): p. 353-356.
59. Coleman, J.N., M. Cadek, R. Blake, V. Nicolosi, K.P. Ryan, C. Belton, A. Fonseca, J.B. Nagy, Y.K. Gun'ko, and W.J. Blau, *High-performance nanotube-reinforced plastics: Understanding the mechanism of strength increase*. Advanced Functional Materials, 2004. **14**(8): p. 791-798.
60. Chang, T.E., L.R. Jensen, A. Kisliuk, R.B. Pipes, R. Pyrz, and A.P. Sokolov, *Microscopic mechanism of reinforcement in single-wall carbon nanotube/polypropylene nanocomposite*. Polymer, 2005. **46**(2): p. 439-444.

61. Kearns, J.C. and R.L. Shambaugh, *Polypropylene fibers reinforced with carbon nanotubes*. Journal of Applied Polymer Science, 2002. **86**(8): p. 2079-2084.
62. Haggemueller, R., H.H. Gommans, A.G. Rinzler, J.E. Fischer, and K.I. Winey, *Aligned single-wall carbon nanotubes in composites by melt processing methods*. Chemical Physics Letters, 2000. **330**(3-4): p. 219-225.
63. Sandler, J.K.W., S. Pegel, M. Cadek, F. Gojny, M. Van Es, J. Lohmar, W.J. Blau, K. Schulte, A.H. Windle, and M.S.P. Shaffer, *A comparative study of melt spun polyamide-12 fibres reinforced with carbon nanotubes and nanofibres*. Polymer, 2004. **45**(6): p. 2001-2015.
64. Gorga, R.E. and R.E. Cohen, *Toughness enhancements in poly(methyl methacrylate) by addition of oriented multiwall carbon nanotubes*. Journal of Polymer Science, Part B: Polymer Physics, 2004. **42**(14): p. 2690-2702.
65. Meincke, O., D. Kaempfer, H. Weickmann, C. Friedrich, M. Vathauer, and H. Warth, *Mechanical properties and electrical conductivity of carbon-nanotube filled polyamide-6 and its blends with acrylonitrile/butadiene/styrene*. Polymer, 2004. **45**(3): p. 739-748.
66. Thostenson, E.T. and T.W. Chou, *Aligned multi-walled carbon nanotube-reinforced composites: Processing and mechanical characterization*. Journal of Physics D: Applied Physics, 2002. **35**(16).
67. Manchado, M.A.L., L. Valentini, J. Biagiotti, and J.M. Kenny, *Thermal and mechanical properties of single-walled carbon nanotubes-polypropylene composites prepared by melt processing*. Carbon, 2005. **43**(7): p. 1499-1505.
68. Bai, J., *Evidence of the reinforcement role of chemical vapour deposition multi-walled carbon nanotubes in a polymer matrix*. Carbon, 2003. **41**(6): p. 1325-1328.
69. Breton, Y., G. Desarmot, J.P. Salvétat, S. Delpoux, C. Sinturel, F. Beguin, and S. Bonnamy, *Mechanical properties of multiwall carbon nanotubes/epoxy composites: Influence of network morphology*. Carbon, 2004. **42**(5-6): p. 1027-1030.
70. Allaoui, A., S. Bai, H.M. Cheng, and J.B. Bai, *Mechanical and electrical properties of a MWNT/epoxy composite*. Composites Science and Technology, 2002. **62**(15): p. 1993-1998.
71. Zhu, J., H. Peng, F. Rodriguez-Macias, J.L. Margrave, V.N. Khabashesku, A.M. Imam, K. Lozano, and E.V. Barrera, *Reinforcing epoxy polymer composites through covalent integration of functionalized nanotubes*. Advanced Functional Materials, 2004. **14**(7): p. 643-648.
72. Park, C., Z. Ounaies, K.A. Watson, R.E. Crooks, J. Smith Jr, S.E. Lowther, J.W. Connell, E.J. Siochi, J.S. Harrison, and T.L. St Clair, *Dispersion of single wall carbon nanotubes by in situ polymerization under sonication*. Chemical Physics Letters, 2002. **364**(3-4): p. 303-308.
73. Gao, J., M.E. Itkis, A. Yu, E. Bekyarova, B. Zhao, and R.C. Haddon, *Continuous spinning of a single-walled carbon nanotube-nylon composite*

- fiber*. Journal of the American Chemical Society, 2005. **127**(11): p. 3847-3854.
74. Wang, Z., Z. Liang, B. Wang, C. Zhang, and L. Kramer, *Processing and property investigation of single-walled carbon nanotube (SWNT) buckypaper/epoxy resin matrix nanocomposites*. Composites Part A: Applied Science and Manufacturing, 2004. **35**(10): p. 1225-1232.
  75. Lee, Z., C. Ophus, L.M. Fischer, N. Nelson-Fitzpatrick, K.L. Westra, S. Evoy, V. Radmilovic, U. Dahmen, and D. Mitlin, *Metallic NEMS components fabricated from nanocomposite Al-Mo films*. Nanotechnology, 2006. **17**(12): p. 3063-3070.
  76. Lu, S. and B. Panchapakesan, *Nanotube micro-optomechanical actuators*. Applied Physics Letters, 2006. **88**(25).
  77. Srikar, V.T. and S.M. Spearing, *A critical review of microscale mechanical testing methods used in the design of microelectromechanical systems*. Experimental Mechanics, 2003. **43**(3): p. 238-247.
  78. Vengallatore, S., *Analysis of thermoelastic damping in laminated composite micromechanical beam resonators*. Journal of Micromechanics and Microengineering, 2005. **15**(12): p. 2398-2404.
  79. Huang, C.K., W.M. Lou, C.J. Tsai, T.C. Wu, and H.Y. Lin, *Mechanical properties of polymer thin film measured by the bulge test*. Thin Solid Films, 2007. **515**(18): p. 7222-7226.
  80. Zheng, D.W., Y.H. Xu, Y.P. Tsai, K.N. Tu, P. Patterson, B. Zhao, Q.Z. Liu, and M. Brongo, *Mechanical property measurement of thin polymeric-low dielectric-constant films using bulge testing method*. Applied Physics Letters, 2000. **76**(15): p. 2008-2010.
  81. Jansen, K.M.B., V. Gonda, L.J. Ernst, H.J.L. Bressers, and G.Q. Zhang, *State-of-the-Art of Thermo-Mechanical Characterization of Thin Polymer Films*. Journal of Electronic Packaging, Transactions of the ASME, 2005. **127**(4): p. 530-536.
  82. Oliver, W.C. and G.M. Pharr, *Measurement of hardness and elastic modulus by instrumented indentation: Advances in understanding and refinements to methodology*. Journal of Materials Research, 2004. **19**(1): p. 3-20.
  83. Tranchida, D., S. Piccarolo, J. Loos, and A. Alexeev, *Accurately evaluating Young's modulus of polymers through nanoindentations: A phenomenological correction factor to the Oliver and Pharr procedure*. Applied Physics Letters, 2006. **89**(17).
  84. VanLandingham, M.R., J.S. Villarrubia, W.F. Guthrie, and G.F. Meyers, *Nanoindentation of polymers: An overview*. Macromolecular Symposia, 2001. **167**(1): p. 15-43.
  85. Oyen, M.L., *Analytical techniques for indentation of viscoelastic materials*. Philosophical Magazine, 2006. **86**(33-35 SPEC ISSUE): p. 5625-5641.
  86. Tweedie, C.A. and K.J. Van Vliet, *Contact creep compliance of viscoelastic materials via nanoindentation*. Journal of Materials Research, 2006. **21**(6): p. 1576-1589.

87. Lu, H., B. Wang, J. Ma, G. Huang, and H. Viswanathan, *Measurement of creep compliance of solid polymers by nanoindentation*. *Mechanics Time-Dependent Materials*, 2003. **7**(3-4): p. 189-207.
88. Huang, G. and H. Lu, *Measurement of Young's relaxation modulus using nanoindentation*. *Mechanics of Time-Dependent Materials*, 2006. **10**(3): p. 229-243.
89. Odegard, G.M., T.S. Gates, and H.M. Herring, *Characterization of viscoelastic properties of polymeric materials through nanoindentation*. *Experimental Mechanics*, 2005. **45**(2): p. 130-6.
90. Huang, G., B. Wang, and H. Lu, *Measurements of viscoelastic functions of polymers in the frequency-domain using nanoindentation*. *Mechanics of Time-Dependent Materials*, 2004. **8**(4): p. 345-364.
91. Schiffmann, K.I. and C. Brill, *Testing the viscoelastic properties of SU8 photo resist thin films at different stages of processing by nanoindentation creep and stress relaxation*. *International Journal of Materials Research*, 2007(5): p. 397-403.
92. Cheng, L., X. Xia, L.E. Scriven, and W.W. Gerberich, *Spherical-tip indentation of viscoelastic material*. *Mechanics of Materials*, 2005. **37**(1): p. 213-226.
93. Leseman, Z.C., H.K. Jeong, T.J. Mackin, R.I. Masel, and M. Begley. *Measurements of the mechanical properties of freestanding nanoscale membranes*. in *American Society of Mechanical Engineers, Micro-Electro Mechanical Systems Division, (Publications) MEMS*. 2006.
94. Wang, T.H., T.H. Fang, S.H. Kang, and Y.C. Lin, *Nanoindentation characteristics of clamped freestanding Cu membranes*. *Nanotechnology*, 2007. **18**(13).
95. Zhang, R., D. Shilo, G. Ravichandran, and K. Bhattacharya, *Mechanical characterization of released thin films by contact loading*. *Journal of Applied Mechanics, Transactions ASME*, 2006. **73**(5): p. 730-736.
96. Begley, M.R. and T.J. Mackin, *Spherical indentation of freestanding circular thin films in the membrane regime*. *Journal of the Mechanics and Physics of Solids*, 2004. **52**(9): p. 2005-2023.
97. Ju, B.F., K.K. Liu, S.F. Ling, and W. Hong Ng, *A novel technique for characterizing elastic properties of thin biological membrane*. *Mechanics of Materials*, 2002. **34**(11): p. 749-754.
98. Ju, B.F., Y. Ju, M. Saka, K.K. Liu, and K.T. Wan, *A systematic method for characterizing the elastic properties and adhesion of a thin polymer membrane*. *International Journal of Mechanical Sciences*, 2005. **47**(3): p. 319-332.
99. Scott, O.N., M.R. Begley, U. Komaragiri, and T.J. Mackin, *Indentation of freestanding circular elastomer films using spherical indenters*. *Acta Materialia*, 2004. **52**(16): p. 4877-4885.
100. Timoshenko, S. and S. Woinowsky-Krieger, *Theory of Plates and Shells*. 2nd ed. 1959, New York: McGraw-Hill
101. Komaragiri, U., M.R. Begley, and J.G. Simmonds, *The mechanical response of freestanding circular elastic films under point and pressure*

- loads. *Journal of Applied Mechanics, Transactions ASME*, 2005. **72**(2): p. 203-212.
102. Gerberich, W.W., W. Yu, D. Kramer, A. Strojny, D. Bahr, E. Lilleodden, and J. Nelson, *Elastic loading and elastoplastic unloading from nanometer level indentations for modulus determinations*. *Journal of Materials Research*, 1998. **13**(2): p. 421-436.
  103. Fischer-Cripps, A., *Nanoindentation*. 2nd ed. 2004, New York: Springer.
  104. Walter, C., T. Antretter, R. Daniel, and C. Mitterer, *Finite element simulation of the effect of surface roughness on nanoindentation of thin films with spherical indenters*. *Surface and Coatings Technology*, 2007. **202**(4-7): p. 1103-1107.
  105. Manual, A., *ANSYS Manual, Version 10*. 2005, Canonsburg (PA): SAS IP
  106. Wriggers, P., *Computational Contact Mechanics*. 2006: Springer.
  107. Gonda, V., J. Den Toonder, J. Beijer, G.Q. Zhang, and L.J. Ernst, *Finite thickness influence on spherical and conical indentation on viscoelastic thin polymer film*. *Journal of Electronic Packaging, Transactions of the ASME*, 2005. **127**(1): p. 33-37.
  108. Drozdov, A.D. and Q. Yuan, *The viscoelastic and viscoplastic behavior of low-density polyethylene*. *International Journal of Solids and Structures*, 2003. **40**(10): p. 2321-2342.
  109. Zhao, Q., J.R. Wood, and H.D. Wagner, *Stress fields around defects and fibers in a polymer using carbon nanotubes as sensors*. *Applied Physics Letters*, 2001. **78**(12): p. 1748-1750.
  110. Ashrafi, B., P. Hubert, and S. Vengallatore, *Carbon nanotube-reinforced composites as structural materials for microactuators in microelectromechanical systems*. *Nanotechnology*, 2006. **17**(19): p. 4895-4903.
  111. Suhr, J., N. Koratkar, P. Koblinski, and P. Ajayan, *Viscoelasticity in carbon nanotube composites*. *Nature Materials*, 2005. **4**(2): p. 134-137.
  112. Satyanarayana, N., K. Rajan, S. Sinha, and L. Shen, *Carbon Nanotube Reinforced Polyimide Thin-film for High Wear Durability*. *Tribology Letters*, 2007. **27**(2): p. 181-188.
  113. Cattin, C., *Electrical Properties of Single Walled Carbon Nanotube-Reinforced Epoxy Vinyl Ester Resin*. 2007, McGill University and École Polytechnique Fédérale de Lausanne: Montreal and Lausanne.
  114. Whitten, P.G., G.M. Spinks, and G.G. Wallace, *Mechanical properties of carbon nanotube paper in ionic liquid and aqueous electrolytes*. *Carbon*, 2005. **43**(9): p. 1891-1896.
  115. Cooper, S.M., H.F. Chuang, M. Cinke, B.A. Cruden, and M. Meyyappan, *Gas permeability of a buckypaper membrane*. *Nano Letters*, 2003. **3**(2): p. 189-192.
  116. Knapp, W. and D. Schleussner, *Field-emission characteristics of carbon buckypaper*. *Journal of Vacuum Science and Technology B: Microelectronics and Nanometer Structures*, 2003. **21**(1 SPEC.): p. 557-561.

117. Baughman, R.H., C. Cui, A.A. Zakhidov, Z. Iqbal, J.N. Barisci, G.M. Spinks, G.G. Wallace, A. Mazzoldi, D. De Rossi, A.G. Rinzler, O. Jaschinski, S. Roth, and M. Kertesz, *Carbon nanotube actuators*. Science, 1999. **284**(5418): p. 1340-1344.
118. Song, L., H. Zhang, Z. Zhang, and S. Xie, *Processing and performance improvements of SWNT paper reinforced PEEK nanocomposites*. Composites Part A: Applied Science and Manufacturing, 2007. **38**(2): p. 388-392.
119. Wang, S., Z. Liang, G. Pham, Y.B. Park, B. Wang, C. Zhang, L. Kramer, and P. Funchess, *Controlled nanostructure and high loading of single-walled carbon nanotubes reinforced polycarbonate composite*. Nanotechnology, 2007. **18**(9).
120. Coleman, J.N., W.J. Blau, A.B. Dalton, E. Munoz, S. Collins, B.G. Kim, J. Razal, M. Selvidge, G. Vieiro, and R.H. Baughman, *Improving the mechanical properties of single-walled carbon nanotube sheets by intercalation of polymeric adhesives*. Applied Physics Letters, 2003. **82**(11): p. 1682-1684.
121. Frizzell, C.J., M. In Het Panhuis, D.H. Coutinho, K.J. Balkus, A.I. Minett, W.J. Blau, and J.N. Coleman, *Reinforcement of macroscopic carbon nanotube structures by polymer intercalation: The role of polymer molecular weight and chain conformation*. Physical Review B - Condensed Matter and Materials Physics, 2005. **72**(24): p. 1-8.
122. Lahiff, E., R. Leahy, J.N. Coleman, and W.J. Blau, *Physical properties of novel free-standing polymer-nanotube thin films*. Carbon, 2006. **44**(8): p. 1525-1529.
123. Zhang, X., T.V. Sreekumar, T. Liu, and S. Kumar, *Properties and structure of nitric acid oxidized single wall carbon nanotube films*. Journal of Physical Chemistry B, 2004. **108**(42): p. 16435-16440.
124. Berhan, L., Y.B. Yi, A.M. Sastry, E. Munoz, M. Selvidge, and R. Baughman, *Mechanical properties of nanotube sheets: Alterations in joint morphology and achievable moduli in manufacturable materials*. Journal of Applied Physics, 2004. **95**(8): p. 4335-4345.
125. Astrom, J.A., A.V. Krashennikov, and K. Nordlund, *Carbon nanotube mats and fibers with irradiation-improved mechanical characteristics: A theoretical model*. Physical Review Letters, 2004. **93**(21).
126. Cox, H.L., *The elasticity and strength of paper and other fibrous materials*. British Journal of Applied Physics, 1952. **3**(3): p. 72-79.
127. Kingston, C.T. and B. Simard, *Recent advances in laser synthesis of single-walled carbon nanotubes*. Journal of Nanoscience and Nanotechnology, 2006. **6**(5): p. 1225-1232.
128. Kingston, C.T., Z.J. Jakubek, S. Dénommée, and B. Simard, *Efficient laser synthesis of single-walled carbon nanotubes through laser heating of the condensing vaporization plume*. Carbon, 2004. **42**(8-9): p. 1657-1664.
129. Hou, J.P. and G. Jeronimidis, *Bending stiffness of composite plates with delamination*. Composites Part A: Applied Science and Manufacturing, 2000. **31**(2): p. 121-132.

130. Berthelot, J.-M., *Composite Materials: Mechanical Behavior and Structural Analysis* 1999, New York: Springer.
131. Adhikari, K., *Effects of Functionalized Single Walled Carbon Nanotubes on the Processing and Mechanical Properties of Laminated Composites*, in *Department of Mechanical Engineering*. 2006, Master's Thesis, McGill University: Montreal.
132. Popov, V.N., V.E. Van Doren, and M. Balkanski, *Elastic properties of crystals of single-walled carbon nanotubes*. *Solid State Communications*, 2000. **114**(7): p. 395-399.
133. Valavala, P.K. and G.M. Odegard, *Modeling techniques for determination of mechanical properties of polymer nanocomposites*. *Reviews on Advanced Materials Science*, 2005. **9**(1): p. 34-44.
134. Dai, L., A. Patil, X. Gong, Z. Guo, L. Liu, Y. Liu, and D. Zhu, *Aligned Nanotubes*. *ChemPhysChem*, 2003. **4**(11): p. 1150-1169.
135. Melechko, A.V., V.I. Merkulov, T.E. McKnight, M.A. Guillorn, K.L. Klein, D.H. Lowndes, and M.L. Simpson, *Vertically aligned carbon nanofibers and related structures: Controlled synthesis and directed assembly*. *Journal of Applied Physics*, 2005. **97**(4): p. 041301-1-041301-39.
136. Garcia, E.J., A.J. Hart, B.L. Wardle, and A.H. Slocum, *Fabrication and nanocompression testing of aligned carbon-nanotube-polymer nanocomposites*. *Advanced Materials*, 2007. **19**(16): p. 2151-2156.
137. Garg, A. and S.B. Sinnott, *Effect of chemical functionalization on the mechanical properties of carbon nanotubes*. *Chemical Physics Letters*, 1998. **295**(4): p. 273-278.